Time-resolved plasmonics in designed nanostructures

Lorek, Eleonora

2016

Time-resolved plasmonics in designed nanostructures

Eleonora Lorek

Doctoral Thesis
2016

Lund University

Time-resolved plasmonics in designed nanostructures

Printed in Sweden by Media-Tryck, Lund, 2016

Division of Atomic Physics
Department of Physics
Faculty of Engineering, LTH
Lund University
P.O. Box 118
SE–221 00 Lund
Sweden
www.atomic.physics.lu.se

ISSN 0281-2762
Lund Reports on Atomic Physics, LRAP 511 (2016)

ISBN (print) 978-91-7623-632-1
ISBN (pdf) 978-91-7623-633-8

Front page image adapted with permission from Gallery Yopriceville

"What I cannot create, I do not understand." Richard Feynman

Abstract

A metal nanoparticle can be considered as consisting of a base of positive ion cores and a sea of free electrons. When the free electrons are displaced, for example, by an incident electric field, a restoring force acts on the electrons. The electrons may then oscillate back and forth until equilibrium is reached. This oscillation occurs at the natural frequency, or eigenfrequency, of the system. By matching the driving frequency with this frequency, the amplitude (the maximum electron displacement) can be made large - the system is in resonance. This resonance mode is a plasmon. The separation of charge on that small length scale will result in a large field in the vicinity of the nanoparticle. This large field, often oscillating at optical frequencies, on the spatial scale of nanometers, has many potential applications, such as high-resolution microscopy, photo-voltaics, light emission and coherent control.

Because of the interest in manipulating light on the nanoscale, particles having their resonances in the optical domain are often used. The collective electron oscillation, when resonantly excited, therefore occurs on the femtosecond timescale. Due to this ultrashort timescale, the dynamics are difficult to follow in time. The spatial confinement of the oscillation to the nanometer scale makes it challenging to also image them.

This thesis explores ways of studying the ultrafast dynamics of plasmons spatially and temporally, simultaneously. Two types of experiments are discussed. The first is autocorrelation experiments where the induced and enhanced field is autocorrelated with itself. For one of these experiments, bowtie nanoantennas were manufactured, using the focused ion beam technique. In the second kind of experiment an infrared laser pulse is used to excite the plasmon, and a short attosecond pulse probes it. The work described in this thesis deals with the fabrication of nanostructures and the implementation of attosecond pulse generation schemes suitable for this purpose.

Populärvetenskaplig sammanfattning

Var är vi någonstans? Var har vi hamnat? Dessa är frågor vi kan ställa som barn när vi börjar upptäcka världen omkring oss. Men bara för att vi växer upp och lär oss mer om världen betyder det inte att vi helt får svar på de frågorna. Omkring oss ser vi röda bussar, blå hav och gula blommor. Men enligt vetenskapen är det inte sådana saker vi fundamentalt har omkring oss. Vi börjar med aspekten färg. Fysiker som Galilei [1] och Newton [2] menade att objekten omkring oss, samt ljuset som reflekteras från dem, saknar färg och att färg är något som först skapas i vårt medvetande. Denna hållning är också så etablerad inom psykologin att den står med i moderna läroböcker i ämnet [3, 4]. Färg anses vara något som bara finns i vårt medvetande, precis som till exempel smärta.

Om vi antar denna hållning, vad säger det om platserna vi ser omkring oss? Färgerna finns på vissa platser i vårt synfält. Om färgerna skapas av vår hjärna bör rimligtvis de platser i synfältet som bär färgen också skapas av vår hjärna. Det betyder att hela vår visuella värld, det vill säga det vi ser, helt skapas av hjärnan. Kanske dock baserat på fysiska input till ögonen, såsom ljus. Man talar ibland om det vi ser som en projektion eller ett användargränssnitt [5, 6] - vi interagerar med den bakomliggande verkligheten genom det vi upplever, analogt med hur vi interagerar med datorns hårdvara genom att klicka på ikoner på datorskärmen. Som skäl att vi har ett sådant här användargränssnitt brukar man ange det naturliga urvalet. Genom detta gränssnitt får organismen hjälp att notera och initiera responser och känna igen saker i sin omgivning [6].

Så nu när vi inte verkar kunna lita på våra sinnen för direkt åtkomst av verkligheten, hur ska vi göra för att få kunskap om verkligheten bakom det vi ser? Vi får här vända oss till fysiken. I fysiken beskrivs hur elektroner i atomer svänger och när de gör det, orsakar ett elektriskt fält som i sin tur får andra elektroner att svänga. Så när vi ”ser” ett objekt, upplyst av till exempel en glödlampa, är det egentligen elektroner i glödlampan som vibrerar, vilket sätter elektroner hos objektet i vibration, vilket i sin tur bör få elektroner i våra synreceptorer att börja vibrera. Utefter denna vibration skickas sedan en signal till hjärnan som då skapar en representation av vad som finns omkring oss – den skapar det vi ser. För att förstå den fysikaliska basen till vad vi ser omkring oss behöver vi alltså förstå atomer och hur de interagerar med varandra genom elektriska fält.

En metallnanopartikel kan ses som en modell av en atom, en leksaksatom. Båda

system består av en tyngre positivt laddad del. I atomens fall är det en kärna, i nanostrukturens fall är det den fixa jonkärnebakgrunden. Båda system innehåller negativt laddade och lättrörliga elektroner. I atomen är det ett fåtal elektroner medan det i metallstrukturen är ett ”hav” av fria elektroner. Om elektronerna flyttas lite grand i förhållande till kärnan eller kärnorna, (genom att ett elektriskt fält, till exempel, appliceras), kommer elektronerna att svänga tillbaka mot den positiva delen, svänga förbi, svänga tillbaka mot den positiva delen, och så vidare tills svängningen slutligen mattas av. De kommer att göra det på sin naturliga frekvens. Detta sker på samma sätt som när man puttar på en gunga - den kommer att svänga fram och tillbaka på sin naturliga frekvens tills den hittar sitt jämviktsläge, det vill säga att hänga rakt ner. Som vi såg ovan, orsakar elektronsvängningen ett elektriskt fält. Detta fält kommer att breda ut sig som en våg med samma frekvens som svängingen. För många metallnanostrukturer och många atomer svänger elektronerna med en frekvens av storleksordningen 10^{14} Hz, vilket leder till en elektromagnetisk våg med samma frekvens. Elektromagnetiska vågor med denna frekvens är vad våra ögon reagerar på och vi kallar dessa vågor ljus eller synlig strålning. Detta ljus kan i sin tur få elektroner i andra system att svänga, vilket kan leda till absorption där. Både atomer och nanostrukturer kan alltså både emittera och absorbera ljus. Utöver dessa likheter mellan metallnanostrukturer och atomer finns den viktiga skillnaden att nanostrukturer idag kan designas och framställas så att de får speciella egenskaper, till exempel en viss naturlig frekvens. De kan dessutom studeras individuellt. Genom att noggrant studera nanostrukturer kanske vi kan få en bättre förståelse av atomer, vilka och vars interaktion utgör grunden för det vi ser. Det finns dessutom en rad tekniska tillämpningar av metallnanostrukturer, då de både kan förstärka och fokusera infallande ljus.

På grund av att elektronerna i nanostrukturen förflyttar sig på så liten skala och så fort är deras rörelse mycket svår att följa. Den här avhandlingen diskuterar två sätt att ändå försöka göra det på. Båda innebär användning av ett elektronmikroskop. Med den ena metoden använder man två ljuspulser som består av ett elektriskt fält som bara svänger några enstaka perioder och med en våglängd som tillhör den infraröda delen av det elektromagnetiska spektrumet. Dessa skickas in i mikroskopet och får träffa nanostrukturen. Varje puls driver elektronerna några perioder varefter de får svänga fritt. Från områden där många elektroner packas ihop kan elektronerna lämna strukturen genom att ett statiskt elektriskt fält är pålagt. Var elektronerna lämnar och inte lämnar metallen avbildas sedan i mikroskopet. Genom att variera tiden mellan de två ljuspulserna kommer man att få olika hög elektron-emission från en viss punkt. Kanske svänger elektronerna i fas på grund av de två drivfälten, vilket leder till tätt packade elektroner och hög emission, eller så svänger elektronerna i motfas, vilket leder till lägre emission. Hur emissionen från en viss punkt varierar med tiden mellan pulserna berättar om svängningen hos elektronerna. Det andra sättet att studera elektronsvängningen hos nanostrukturen är att först driva den med en kort infraröd puls bestående av några få perioder och sen låta den svänga fritt utan att få hög emission. Vid olika tidpunkter relativt den infraröda pulsen kan man sen komma in med en ännu kortare puls, en attosekundspuls (10^{-18} s). Attosekundspulsen fungerar som ett slags ”snapshot” och orsakar bara elektronemission när den är där. På så sätt kan man ”fotografera” var elektronerna befinner sig under den längre pulsens gång och efter den är över. I avhandlingen beskrivs experiment som utnyttjar den första tekniken och steg mot ett experiment som utnyttjar den andra tekniken.

Med dessa experiment och fler av sitt slag kan vi förhoppningsvis förstå metall-

nanostrukturer, tekniska tillämpningar av dessa, atomer och, kanske också, var vi har hamnat någonstans, lite bättre.

Popular Science Summary

Where are we? And what are all the things we have around us? These are questions that we ask as children when we start to discover the world around us. But just because we grow up does not mean that we find the answers to those questions. Around us, we see things as red buses, blue oceans and yellow flowers. But according to science, it is not these things that we fundamentally have around us. Let us start with the concept of color. Physicists like Galilei [1] and Newton [2] argued that the objects around us, as well as the light reflected from them, actually lack color and that colors are created in our consciousness. This point of view is today so established within psychology that it is presented in modern textbooks about the subject [3, 4]. Color is seen as something which only exists in our consciousness, just like for example pain.

If we assume this point of view to be true, what does it tell us about the places we observe around us? The colors are at specific locations in our field of view. If the colors are created in our brain, so should the places in our visual field carrying those colors be. This means that our visual world, everything we see, is created in the brain. Maybe, however, based on physical input to our eyes, such as light. Some researchers talk about the perceived world as a projection or a user interface [5, 6] – we interact with fundamental reality through what we experience, in the same way as we interact computers by clicking on icons on the computer screen. As an explanation for us being equipped with this user interface, natural selection is often suggested. The user interface helps the organism to note and initiate responses, and recognize objects in its environment [6].

So, if we can't directly access reality through our senses, what should we do to gain knowledge about the fundamental reality behind what we see? We have to turn to physics. Physics describes how electrons in atoms oscillate and, when they do so, cause an electric field, which in turn makes other electrons oscillate. So when we think we "see" an object illuminated, for example, by a light bulb, it is really electrons in the light bulb that oscillate, cause the electrons in the object to oscillate, which in turn should make the electrons in our eye photoreceptors oscillate. A signal is sent to the brain which then creates a representation of what is around us – it creates what we are seeing. To understand the physical basis of what we see around us, we therefore have to understand atoms, and how they interact with each other through electric fields.

A metal nanoparticle can be regarded as a model of an atom, or a "toy atom"1Â§. Both systems have a heavy positively charged part. In the case of the atom it is a nucleus, while in the case of the nanostructure it is the fixed ion core background. Both systems contain easily movable, negatively charged, electrons. Atoms only have

a few electrons, while metal nanostructures contain a "sea" of free electrons. If the electrons are slightly displaced with respect to the core or cores, (for example, by an applied electric field) the electrons will swing back towards the positive part, overshoot, swing back again to the positive part, and so on until the oscillation finally stops. The electrons will oscillate at the natural frequency of the system. This electron oscillation occurs in the same way as when a swing is pushed. The swing will oscillate back and forth at its natural frequency until it reaches its equilibrium, that is to hang straight down. As seen above, the electron oscillation will cause an electric field. This field will propagate as a wave with the same frequency as the oscillation. For many metal nanostructures and many types of atoms, the electrons naturally oscillate at frequencies on the order of 10^{14} Hz, which leads to an electromagnetic wave with the same frequency. Our eyes are sensitive to electromagnetic waves of this frequency, and we call these waves light or visible radiation. This light can, in turn, make electrons in other systems oscillate, possibly resulting in absorption of the light there. Both atoms and metal nanostructures can thus both emit and absorb light. Although there are similarities between metal nanostructures and atoms, there is an important difference in that nanostructures can today be designed and fabricated so that they have specific properties, for example, a certain natural frequency. Additionally, they can be studied individually. By studying nanostructures, we may be able to gain a better understanding of atoms, the interaction of which forms the basis of what we see. There are also many technical applications of metal nanostructures, as they can both enhance and focus incoming light.

Because the electrons are displaced on such a small spatial scale and so rapidly, their motion is very difficult to follow. This thesis discusses two ways of still doing this. Both involve the use of an electron microscope. The first method uses two pulses consisting of only a few cycles, and with a wavelength in the infrared part of the electromagnetic spectrum. The pulses are sent into the microscope where they impinge on the nanostructure. Each pulse drives the electrons a few cycles back and forth, whereafter they oscillate freely. From areas where many electrons are densely packed the electrons can leave the structure due to an applied static electric field. Images can then be obtained of the areas from which electrons leave, and areas where they do not. The electron emission from a particular point can be made to vary by varying the time between two light pulses. The electrons may oscillate in phase as a result of the two pulses, leading to densely packed electrons and high emission, or they may oscillate out of phase, leading to lower emission. The way in which the emission from a given point varies with the time between the pulses provides information about the oscillation of the electrons. The other way of studying electron oscillations in the nanostructure is to first drive it with a short infrared pulse consisting of only a few cycles, and then let the electrons oscillate freely, without high emission. An even shorter pulse, an attosecond pulse (10^{-18} s) will then be seen at different times relative to the infrared pulse. The attosecond pulse provides a kind of snapshot, and only causes electron emission during its short duration. In this way, it is possible to take "photographs" of where the electrons are during and after the infrared pulse. This thesis describes experiments using the first technique, and steps towards experiments using the second.

Hopefully, these experiments, and similar ones, will help us understand nanoparticles and their applications, atoms, and maybe also, where we are, a little better.

List of Publications

This thesis is based on the following papers, which will be referred to in the text by their roman numerals.

I **Secondary electron imaging of nanostructures using extreme ultraviolet attosecond pulse trains and infrared femtosecond pulses**
E. Mårsell, C.L. Arnold, E. Lorek, D. Guenot, T. Fordell, M. Miranda, J. Mauritsson, H. Xu, A. L'Huillier and A. Mikkelsen.
Annalen der Physik **525**, 162–170 (2013).

II **High-order harmonic generation using a high-repetition-rate turnkey laser**
E. Lorek, E.W. Larsen, C.M. Heyl, S. Carlström, D. Paleček, D. Zigmantas and J. Mauritsson.
Review of Scientific Instruments **85**, 123106 (2014).

III **Imaging localized surface plasmons by femtosecond to attosecond time-resolved photoelectron emission microscopy- "ATTO-PEEM"**
S.H. Chew, K. Pearce, C. Späth, A. Guggenmos, J. Schmidt, F. Süßmann, M.F. Kling, U. Kleineberg, E. Mårsell, C.L. Arnold, E. Lorek, P. Rudawski, C. Guo, M. Miranda, F. Ardana, J. Mauritsson, A. L'Huillier and A. Mikkelsen.
(2015) *Chapter in the book: "Attosecond Nanophysics", editors: P. Hommelhoff and M.F. Kling, Wiley-VCH Verlag GmbH and Co. KGaA.*

IV **Carrier-envelope phase-dependent high-order harmonic generation with a high-repetition-rate OPCPA system**
P. Rudawski, A. Harth, C. Guo, E. Lorek, M. Miranda, C.M. Heyl, E.W. Larsen, J. Ahrens, O. Prochnow, T. Binhammer, U. Morgner, J. Mauritsson, A. L'Huillier and C.L. Arnold.
The European Physical Journal D **69**, 147–152 (2015).

V **Nanoscale imaging of local few-femtosecond near-field dynamics within a single plasmonic nanoantenna**
E. Mårsell, A. Losquin, R. Svärd, M. Miranda, C. Guo, A. Harth, E. Lorek, J. Mauritsson, C.L. Arnold, H. Xu, A. L'Huillier and A. Mikkelsen.
Nano Letters **15**, 6601-6608 (2015).

VI **Size- and shape-dependent few-cycle near-field dynamics of bowtie nanoantennas**
E. Lorek, E. Mårsell, A. Losquin, M. Miranda, A. Harth, C. Guo, R. Svärd, C.L. Arnold, A. L'Huiller, A. Mikkelsen and J. Mauritsson.
Optics Express **23**, 31460-31471 (2015).

VII **Trajectory-resolved high-order harmonic generation in elliptically polarized fields in the presence of resonances**
E.W. Larsen, S. Carlström, E. Lorek, C.M. Heyl, D. Paleček, K.J. Schafer, A. L'Huiller, D. Zigmantas and J. Mauritsson.
Submitted for publication.

VIII **Spatially and spectrally resolved quantum path interference with chirped driving pulses**
J. Preclíková, S. Carlström, E. Lorek, E.W. Larsen, C.M. Heyl, D. Paleček, D. Zigmantas, K.J. Schafer and J. Mauritsson.
Manuscript in preparation.

Contents

Papers

Chapter 1

Introduction

1.1 Introduction

This thesis describes experiments in which designed metal nanoparticles are illuminated by laser pulses and studied in a time-resolved manner. Metal nanoparticles are interesting for a number of reasons. One is that, if they are very small, they bear many resemblances to atoms, which are fundamental to the way in which we perceive the things around us. The resemblances between metal nanoparticles and atoms can be understood by using a simplified picture of the latter, and both can then be regarded as dipoles in harmonic motion [7].

When displaced from its equilibrium position, an harmonic oscillator experiences a force proportional to the displacement. Such oscillators have a natural frequency associated to them, and when driven at this frequency, the amplitude of the oscillation becomes high and resonance occurs. Familiar examples of such systems are swings and other pendulums. If you give a swing one hard and short push, it will swing back and forth at its own natural frequency. Should you push it every time it passed you, at that frequency, the amplitude will increase and resonance will occur. The swing moves towards its equilibrium position (to hang straight down) because a restoring gravitational force acts to minimize the potential energy of the system. When positive charges are separated from negative charges by a certain distance, this system is called an electric dipole. The dipole has electric potential energy and so will also experience a restoring force, the electrical Coulomb force, which will also act so as to minimize that energy.

An atom consists of a positively charged nucleus and surrounding negatively charged electrons, which are attracted to the nucleus by the Coulomb force. In the simplified picture [7], the outermost bound electrons are bound to their respective atom by an elastic restoring force proportional to the displacement of the electrons. When the electrons are driven at their natural frequency, they will oscillate around the nucleus with a high amplitude. This is a simplified description of what happens when an atom undergoes a transition from one energy level to another [7]. Thus, the atom, during an energy transition, can be considered as a dipole in harmonic motion.

Metals can be described as a fixed ion core background with conduction electrons able to move almost freely around the material [8]. This is in contrast to dielectrics

where all the charges are bound to specific atoms or molecules [9]. Suppose that an homogeneous electromagnetic field is applied to a very small metal nanoparticle for a very short time. The field then exerts a force on the conduction electrons such that they move towards one of the surfaces. This will lead to the accumulation of electrons on one side, and a reduced number of electrons on the opposite side, creating a dipole. The dipole generates an electric field inside the nanoparticle with the opposite direction compared to the initial external field that pulls the electrons back towards their equilibrium position. The electrons may then overshoot the equilibrium position, and oscillate back and forth, with the natural frequency of the system, until equilibrium is reached. The greater the initial displacement, the greater the restoring force. Let us now apply light - an electromagnetic field which is varying in time. If the frequency of the incident light matches the natural frequency of the system, we can expect large displacements, just as in the case of the swing. Thus, the metal nanoparticle can, when excited, be considered a dipole in harmonic motion, similarly to the atom during an energy transition. This electromagnetic excitation of the conduction electrons of metallic nanostructures coupled to an electromagnetic field is called a localized surface plasmon [10]. They are similar to surface plasmon polaritons, but the latter are propagating.

As oscillating dipoles can emit and absorb radiation [9], radiation can be emitted and absorbed by both atoms and metal nanostructures. During an atomic transition from one energy level to another, the electron is driven resonantly. The natural frequency of atomic transitions is often in the visible range of the electromagnetic spectrum, or higher. This means frequencies above $4.3 \cdot 10^{14}$ Hz, corresponding to a period shorter than $2.3 \cdot 10^{-15}$ s or 2.3 fs. This, and shorter, is the natural timescale of electron motion in atoms. The emitted and absorbed radiation are of the same frequency as the dipole oscillation. In the case of stimulated emission, the atom starts in the upper state, and the produced radiation is in phase with the incident light. In the case of absorption, the atom starts in the lower state and the light produced by the oscillation is out of phase with the incoming light [11]. Small silver and gold nanoparticles are also resonant in the visible part of the spectrum [10], so by exciting localized surface plasmons in these, light can be absorbed or emitted.

Although the descriptions of atoms and metallic particles given above are simplified, there are similarities between metal nanostructures and atoms. An important difference, however, is that nowadays nanostructures can be fabricated and tailored, to have specific properties, such as a specific natural frequency. In fact, much of the work described in this thesis concerns the fabrication of designed nanostructures (Chapters 2 and 3). Another advantage of nanostructures is that they can, with the right technique, be studied individually. These aspects make metal nanostructures interesting to investigate. The fact that a strong enhancement of a driving electric field occurs and that this field can be effectively focused to below the diffraction limit of light does not make them less interesting. By exploiting plasmons, it is thus possible to manipulate light on the nanoscale, with applications such as high-resolution microscopy and spectroscopy, photo-voltaics, and coherent control [12]. As gold and silver nanoparticles exhibit strong responses in the visible range these materials are commonly studied and used in the field of plasmonics.

This thesis describes studies carried out with the intention of studying collective electron oscillations, *i.e*, localized surface plasmons, in designed nanostructures both spatially and temporally. These phenomena take place on the nanoscale, presenting

a challenge in terms of achieving sufficient spatial resolution in the measurements. Nanometer-sized objects can, however, be studied by electron microscopes. As the de Broglie wavelength of the electron is shorter than the wavelength of light, imaging with a resolution inaccessible with ordinary visible light microscopy is possible. Temporal resolution is, however, a major challenge. As the resonances of gold and silver nanoparticles are in the optical part of the spectrum the collective electron oscillation takes place over a period shorter than 2.3 fs. Even if we could perceive this oscillation spatially with our eyes, we would not be able to resolve it temporally as our eyesight has a temporal resolution of only 0.04 s or $4 \cdot 10^{-2}$ s. We cannot, for example, resolve the 25 frames per second that is the standard for television broadcasting, as different frames. An improvement in temporal resolution of 13 orders of magnitude is required to see the surface plasmon. Measurement techniques using electronics would also be too slow to detect the charge oscillation.

It is thus necessary to use other techniques in order to resolve the collective electron oscillation in metal nanostructures. Imagine that we would like to record a video of a swing in motion. We could either record the complete scenario by taking snapshots at its various positions. But we could also perform a so-called pump-probe measurement. In this case, we release the swing and take an image, then release the swing again, but take the image with a later delay relative the release time. This process is then repeated a number of times, taking snapshots at increasing time delays. Eventually, we will have collected a series of image of the swing at its different locations, at different times. Using this method, it is possible to collect the data for one snapshot over a much longer time than the timescale of the process. Another advantage of pump-probe measurements is that any possible effect of the measurement itself on the system you want to probe is removed, as the process starts again after each measurement. Time-resolved plasmon studies are based on the same idea. The plasmon is excited, and snapshots are taken after various delays with respect to the starting time, giving a video of the collective electron oscillation.

Ideally, we would like to start the oscillation with a short "kick". One of the shortest events possible that would be suitable for this is a few-cycle, 800 nm infrared (IR) laser pulse. This few-fs pulse would drive the oscillation for a few cycles and then leave the electrons to oscillate at their own natural frequency once the pulse ceases. In order to take the snapshots, we need something of much shorter duration than the oscillation period itself. In other words, something on the attosecond timescale. The process of high-order harmonic generation (HHG) can occur when a laser beam is focused into a gas. The process was discovered 1987 [13] and in 2001 it was confirmed that this process indeed can produce light pulses with a duration of attoseconds [14]. These pulses are the shortest controllable events ever created by mankind. One attosecond relates to one second as one second relates to twice the age of the universe. These pulses are produced by an oscillating dipole. The dipole oscillates with a duration of attoseconds. The emitted light is thus in the form of an attosecond pulse. The spectral components of the pulse extends up to the extreme ultraviolet (XUV) part of the electromagnetic spectrum. But how can the attosecond light pulse be made to interact with the plasmon in the nanoparticle so that an image can be recorded?

The answer to this problem is photoemission electron microscopy (PEEM). PEEM is an electron microscope, but the source of electron emission is not other electrons as in many other electron microscopes, but light. Based on the photoelectric effect, discovered in 1905 by Einstein [15], incident light causes electrons from the sample being

studied to leave the sample and these are then imaged by the instrument. The idea of combining PEEM with attosecond pulses to study plasmon dynamics was presented in 2007 by Stockman *et al.* [16]. An IR pulse is used to initiate the electron oscillation. After a certain delay, the attosecond pulse hits the sample and causes photoemission of electrons from the metal particle. In the originally proposed scheme, the measured energy of the emitted electrons would depend on when during the plasmonic cycle they are emitted, thus providing information about the plasmonic field. The idea employed in the present work is slightly different. Mikkelsen *et al.* in 2009 [17] suggested that more electrons are expected from regions in the nanostructure where the electron density is high. In other words, emission is expected from regions where the electric field over the sample, called the near field, is high. Lets assume that we have access to a single attosecond pulse per femtosecond pulse. The femtosecond pulse would drive the electron density, and when it releases it, the density would oscillate freely at its natural frequency. The attosecond pulse is then sent to the nanostructure at different delays with respect to the femtosecond pulse. It would cause a presumed instantaneous photoemission when it is there. We believe that at delays of high density at one location, the signal due to the attosecond pulse would be high, and at delays of low density the signal would be low. The electron density oscillation would thus be mapped on its natural time-scale. Since the full nanostructure and its surrounding would be imaged we can further expect a full video of the charge oscillations. Much related to the HHG part, this kind of IR–XUV experiment is technically demanding, and has not been realized. However, steps towards realization have been taken, and some of them are described in this thesis.

There are, however, other ways of performing time-resolved studies of plasmon dynamics. We performed IR–IR experiments, where two IR pulses hit the nanostructure with a variable delay, each giving rise to an enhanced near field. The first pulse causes a collective electron oscillation resulting in an enhanced field. The second pulse then causes a similar oscillation and field. For certain time delays between the pulses, high photoemission will occur, as both oscillations occur in phase, leading to high charge concentrations and a strong near field. At other time delays, weaker photoemission will result as the two oscillations cancel each other. Plotting the photoemission signal as a function of delay will thus provide information about the plasmon dynamics.

One important step towards the realization of the IR-XUV experiment, is the generation of attosecond pulses at high repetition rate. If the electron density is too high in the PEEM system, for example, at the focus, the electrons will repel each other and cause space-charge effects, which blur the resulting image. This places an upper limit of the number of electrons that should be emitted per attosecond pulse. As only few electrons can be emitted per shot, many shots are required to build up an image. To obtain reasonably short exposure times, considering laser beam fluctuations and other instabilities, and to be able to use apertures to improve the resolution, the number of attosecond shots per second must be high. That is, a high repetition rate of the pulses generating the attosecond pulses is required. Traditionally and due to the high intensity needed to drive the HHG process, those pulses come at a low repetition rate.

Table 1.1: Overview of the experiments described in this thesis. Different combinations of pumps, probes and whether the pulses are applied to nanostructures, were used in the experiments.

		Probe			
Section	Pump	Low rep. rate	High rep. rate	Nanostr. appl.	Paper
3.1–3.3	IR	-	IR	✓	V, VI
4.1	IR	XUV	-	✓	I
4.2	-	-	XUV	-	II, IV, VII, VIII
4.3	-	-	XUV	✓	III
Outlook	IR	-	XUV	✓	

1.2 Thesis outline

The thesis is divided into five chapters. After the introduction of the general topic of the thesis, the experimental techniques employed in these studies are described in Chapter 2. Chapter 3 is devoted to the description of the near-field autocorrelation experiments, while Chapter 4 concerns the steps towards the realization of IR–XUV experiments. Finally, a summary and future outlook are presented in Chapter 5.

Table 1.1 summarizes the experimental schemes described in the different sections. A functioning pump and probe were achieved in the IR–IR experiments (Sections 3.1–3.3). However, XUV pulses are preferable as the probe, as they provide more information about the plasmon dynamics. A preliminary study on the feasibility of an IR–XUV experiment was therefore performed with a laser system with a pulse repetition rate of 1 kHz (Sec. 4.1). Because a higher repetition rate is required, HHG at a repetition rate of 200 kHz was developed (Sec. 4.2), which led to an improvement in the images obtained (Sec. 4.3). The final goal is to pump the nanostructures with IR pulses and imaging them using high-repetition-rate XUV pulses. This is described in the outlook part of Chapter 5.

So far, the general frame of the thesis have been set out. The three main subjects of this thesis are plasmonics, designed nanostructures and time-resolution, which are described in more detail below.

1.3 Plasmonics

Plasmonics is the study of the interaction between electromagnetic radiation and free electrons at metal interfaces, or in small metal nanostructures, leading to an enhanced optical near field of sub-wavelength dimension. It is part of the broader field of nanophotonics, which concerns the confinement of electromagnetic fields over dimensions smaller than the wavelength of optical light [10].

For the interaction between metals and light with angular frequency ω, the dielectric function, $\epsilon(\omega)$, is important. The Drude model of the optical response of metals

defines the dielectric function as [10, 18]:

$$\epsilon(\omega) = 1 - \frac{\omega_p^2}{\omega^2 + i\gamma\omega} \tag{1.1}$$

where the plasma frequency $\omega_p = \sqrt{Ne^2/\epsilon_0 m}$, where N is the number of atoms per unit volume, e the charge of the electron, ϵ_0 the electric constant, and m the electron mass. γ denotes the characteristic collision frequency (typically 100 THz [10]). For most metals, the plasma frequency is in the ultra-violet regime [19]. The plasma frequency can be seen as the natural frequency of an oscillation of the electron sea around the ions in the bulk of the metal [10]. The quanta of these longitudinal oscillations are called plasmons, volume plasmons or bulk plasmons. A plasmon is a quasi-particle. Other quasi-particles include phonons and excitons. Because of their longitudinal character these waves do not connect to transverse electromagnetic waves and can only be initiated by particle impact.

Surface plasmon polaritons are electromagnetic surface waves originating from the coupling between electric fields and oscillations of the conducting electron plasma. They propagate along the interface between a metal and a dielectric. The surface plasmon polariton is evanescently limited in the perpendicular direction. The term "polariton" means that surface plasmons couple with the free electromagnetic field [20]. These excitations cannot be created directly using light.

Non-propagating excitations of conduction electrons in metal nanostructures coupled to electromagnetic fields are called localized surface plasmon polaritons. Since the thesis concerns individual nanoparticles, and not broad surfaces, localized surface plasmons will be described more thoroughly. Also, the term "plasmon" will henceforth be used to denote a localized surface plasmon. When electrons in metal nanoparticles are driven, the positive ion background exerts a restoring force on them so that resonance can occur, as described above. This resonance can be induced by illumination with light and is described more in detail below. The description is mainly based on the book *Plasmonics: Fundamentals and Applications*, by S. Maier [10].

Despite the ending "-on" in "localized surface plasmon", and the nanometer scale involved, plasmons can be described well by classical physics [10]. Let us first consider a particle of a size much smaller than the wavelength of light in the surrounding medium, we are allowed to make the so-called *quasi-static approximation*. In this case, the phase of the harmonically oscillating field is almost constant over the particle volume, so we can calculate the spatial field distribution by assuming the simplified problem of a particle in an electrostatic field. Once the field distribution is known, the time dependence can be added.

Consider a sphere of radius a, located in the static electric field, $\boldsymbol{E} = \boldsymbol{E_0}\hat{\boldsymbol{z}}$, (see Fig. 1.1). At a sufficient distance from the sphere, the field lines are parallel to the z-direction. The surrounding medium is described by the dielectric constant ϵ_m, while the frequency-dependent dielectric function $\epsilon(\omega)$ describes the sphere. It can be shown [10] that the distribution of the electric fields inside and outside the sphere are:

$$\boldsymbol{E_{in}(r)} = \frac{3\epsilon_m}{\epsilon + 2\epsilon_m}\boldsymbol{E_0} \tag{1.2}$$

and

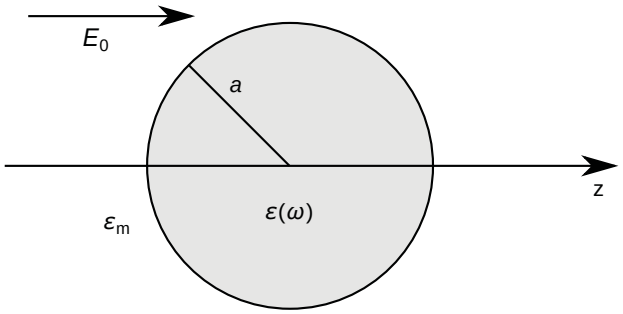

Figure 1.1: A small sphere of radius a and dielectric function $\epsilon(\omega)$ in a surrounding medium with the dielectric constant ϵ_m. The electrostatic field E_0 is applied.

$$\boldsymbol{E_{out}(r)} = \boldsymbol{E_0} + \frac{3\mathbf{n}(\mathbf{n} \cdot \mathbf{p}) - \mathbf{p}}{4\pi\epsilon_0\epsilon_m} - \frac{1}{r^3} \tag{1.3}$$

where $\mathbf{p}$ is the dipole moment, $\mathbf{p} = 4\pi\epsilon_0\epsilon_m a^3 \frac{\epsilon-\epsilon_m}{\epsilon+2\epsilon_m}\boldsymbol{E_0}$ and $\mathbf{n}$ is a unit vector pointing to the observation point $\boldsymbol{r}$, $\mathbf{n} = \frac{\boldsymbol{r}}{|\boldsymbol{r}|}$. The dipole moment is introduced by the applied field and has a magnitude proportional to $|\boldsymbol{E_0}|$. It can be seen that both the internal and external field are resonant when $(\epsilon + 2\epsilon_m)$ is minimum. For the case of a small imaginary part of ϵ, this simplifies to:

$$Re[\epsilon(\omega)] = -2\epsilon_m \tag{1.4}$$

This relationship is called the Fröhlich condition. The Fröhlich condition is satisfied by choosing the appropriate frequency, and the nanoparticle then acts as an electric dipole with enhanced internal and external fields. Many important applications of metal nanoparticles rely on the enhancement of this external field. Metal nanoparticles are sometimes referred to as optical antennas, as they can convert freely propagating optical radiation to localized energy, and vice versa [21]. The field described in Equation 1.3 is the near field around the sphere. In the far field localized surface plasmons lead to extinction or scattering of light. Both absorption and scattering are resonantly enhanced at the plasmon resonance frequency, *i.e.* when the Fröhlich condition is met [10].

This theory of the dipole particle plasmon is, however, only valid for very small spherical or ellipsoidal particles with dimensions below 100 nm, illuminated with visible or near-IR radiation [10]. For larger particles this quasi-static approximation breaks down due to retardation effects, as different parts of the nanostructures are then exposed to different phases of the incident light, which complicates the response. This effect is enhanced when the exciting light deviates from normal incidence. A rigorous electrodynamic approach is then needed. In 1908, Mie [22] provided a theory for the scattering and absorption of electromagnetic radiation by spheres. For other geometries, such as those considered in this work, the Maxwell's equations are solved numerically (for example, using Finite-difference time-domain simulations) for the given geometry. The electric field is then calculated over the geometry for many points in time. The absorption spectrum can then be obtained, and when the res-

onance frequency is known, the spatial field distribution at that frequency can be obtained for the considered geometry.

The plasmons of particles beyond the quasi-static regime are damped by radiative decay, and non-radiative decay due to absorption. For small gold and silver particles the plasmon lifetime is between 5 and 10 fs [10]. When the particle size is comparable to the vacuum wavelength of the exciting light, higher order resonances or modes other than the dipolar mode are seen. For rods and wires odd and even modes can exist. Odd modes have an anti-symmetric charge distribution with respect to the center of the particle, while the even modes have a symmetric distribution [23]. This also means that the even modes do not have a net dipole moment. When light is incident normally, these modes thus do not couple to it.

1.4 Designed nanostructures

Localized plasmon resonances can occur in both isolated individual particles and on roughnesses on films [24]. They occur in metal nanoparticles of any shape. The resonance frequency and field enhancement can be manipulated by the design of the nanoparticle. Three parameters that affect one of or both of these properties are discussed below.

Size. As the size of the particle increases, the resonance is red-shifted [10, 25]. The reason for this is that when the size increases, the distance between the charges at opposite interfaces is increased, leading to a weaker restoring force and thus the frequency is reduced. *Shape.* The field can be further enhanced by designing the nanostructure so that it has sharp features. This gives rise to the so-called lightning-rod effect [26–28]. In contrast to the plasmon, this effect has no frequency dependence, but is a purely geometric phenomenon resulting from the crowding of field lines near the sharp metallic features, due to highly confined charges. For spheroids and prisms, the field enhancement can be a factor of $> 10^3$ [29]. Altering the shape may lead to shifts in resonance frequency. *Gap.* Another way of further increasing the field enhancement is to pair two nanoparticles closely together. Enhancement factors close to $> 10^5$ in the gap region have been reported [29]. The parts of the nanoparticles facing each other then have opposite charges, which increases the electric field. The enhancement is a strong function of separation distance, with greater enhancement for smaller gaps [30]. Particles are considered not to interact when their separation distance is >150 nm [10]. In terms of resonance frequency, a red shift, compared to the case of an isolated particle, is observed [31] when the light is polarized along the inter-particle axis, due to a smaller restoring force on the electron cloud when there is an accumulation of opposite charge close by.

A structure that makes use of both the lightning-rod effect and the effect of coupling two nanostructures is the bowtie nanoantenna [29, 30, 32]. It consists of two triangular prisms separated by a small gap and are capable of very high field enhancement in the gap region. Because of this, bowtie antennas are interesting for various applications, such as high-resolution microscopy and spectroscopy, photo-voltaics and light-emission tailoring [12].

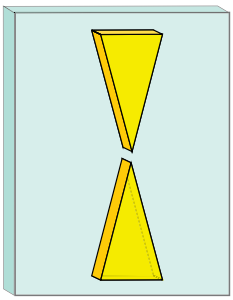

Figure 1.2: A bowtie structure with its two separated triangular prisms.

1.5 Time resolution

In principle, the plasmon is characterized by an eigenfrequency and a lifetime. The collective electron oscillation occurs at a certain frequency, and for a certain time, or, equivalently: the induced near field has a certain frequency, and is present for a certain time. Many techniques can access these quantities [33], for example, spectroscopy. As the eigenfrequencies of the most interesting plasmons are optical, and thus have periods of less than a few fs, time-resolved measurements of the electron dynamics/near-field dynamics are challenging. However, good time resolution is, however, desirable, for at least three reasons. One is that it is interesting in itself to be able to follow the collective electronic motion. Another is that if two or more plasmon modes are excited, their relative phase relation can only be observed with time-resolved measurements as the phase is not accessible in spectroscopic measurements. Thirdly, there are applications exploiting the ultrafast near-field dynamics in nanoparticles. For applications using the dynamics it is desirable to be able to measure them. These applications include coherent control [34], harmonic generation [35] and electron acceleration [36, 37].

Several approaches can be used for time-resolved measurements. Before work started on this thesis, these included the following. 1) PEEM combined with femtosecond laser pulses [24]. Different dynamics of regions of a rough silver film could be observed by combining 10 fs laser pulses passed through an interferometer. 2) PEEM combined with attosecond pulses has been suggested but not yet realized [16]. 3) Femtosecond laser pulses combined with interferometric frequency resolved optical gating [38]. The main advantage of using PEEM compared to the third alternative is that its resolution is not limited by optical diffraction. Another advantage of PEEM is that it is based on imaging, and not on scanning, which means that different parts of the same structure, or different structures, can be investigated simultaneously.

Apart from the general interest in being able to perform time-resolved plasmonics, two topics are of particular interest. One concerns the variations in dynamics of different bowtie nanoantennas. Such bowtie antennas are interesting as they can be used in the applications listed above [34–37]. It is of interest to study the influence of geometrical variations that may be induced during fabrication, on the near-field dynamics, as arrays of such antennas may be used in some applications. This influence was investigated in this work and the findings are described in Paper VI and Chapter 3. The other subject of interest is how the near-field evolves at different parts of a single nanostructure. In Paper V and Chapter 3 a study of this kind is described.

Chapter 2

Experimental toolbox

This chapter described the experimental tools used to realize time-resolved plasmonics in designed nanostructures. Achieving time-resolution in experiments on processes occurring on the femtosecond timescale is difficult. One problem is that data must be collected on a very short timescale. Another is the fact that the process being studied may be seriously affected by the detection process. Both these problems can be avoided in pump–probe experiments. The pump initiates the dynamic process, and the probe produces a measurable signal. The event can be probed at different "times", or stages, by varying the delay between the pump and probe. By repeatedly restarting the process with the pump, the possible effects of the probe on the dynamic process can be avoided.

In such an experiment, a pump, a probe, a detection system are needed. In the present work, an IR femtosecond laser pulse was used to pump the plasmonic field in a metal nanoparticle, and PEEM was used for detection. In IR–IR experiments, an IR pulse was used as the probe pulse, while an XUV attosecond pulse is considered as the probe pulse in a future IR–XUV experiment. The nanostructures investigated were either provided by collaborators or fabricated in-house. Fabrication was carried out using the focused ion beam (FIB) technique, at the Lund Nano Lab. The phenomena, instruments and techniques employed make up the experimental toolbox and each is described in this chapter.

2.1 Pump: IR pulse

Any pulse of light can be regarded as a superposition of waves of different frequencies. The duration of the pulse is inversely proportional to the range of frequencies. The different frequency components interfere to give constructive interference at the peak position of the pulse. Figure 2.1 shows a pulse with its carrier and envelope. When a pulse travels in vacuum, the speed of the carrier wave, *i.e.* the phase velocity, is the same as the speed of the envelope, *i.e.* the group velocity. This will not be the case, however, when the pulse travels through glass or any other dispersive medium. A difference in phase will then develop between the carrier and the envelope, denoted carrier-envelope phase (CEP), as shown in Fig. 2.1. The frequency components of the

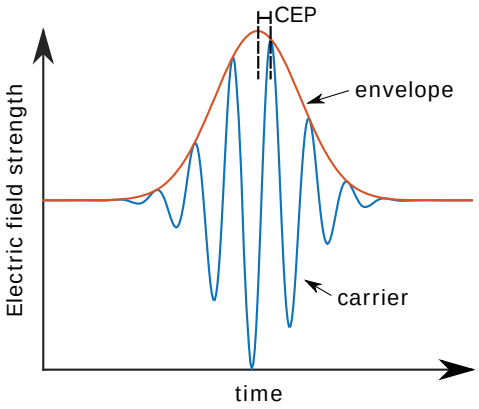

Figure 2.1: A light pulse with its carrier and envelope. The phase difference between the carrier and the envelope, the CEP, is shown.

pulse have different velocities in the glass, which causes stretching of the pulse, and it becomes longer in both time and space. It is then described as being chirped. Another way to chirp a pulse is to make the frequency components travel different distances. This is the principle behind grating compressors and stretchers used in many laser systems.

The type of pulse used as a pump in the time-resolved plasmonics experiment described here was an IR pulse, centered on a wavelength of ∼800 nm. Depending on the experiment, the pulse can either be produced by a laser oscillator alone (Venteon) or by the oscillator combined with an amplification system [39]. In the first case the pulse energy was 1 nJ, the repetition rate 80 MHz and the duration <6 fs. When the laser pulse was amplified, the pulse energy increased to 10 µJ, the repetition rate decreased to 200 kHz and the pulse duration increased to ∼8 fs. However, not all of this amplified energy will, however, be used as excitation of the plasmonic field. Some of it will be used to produce XUV pulses, as discussed in Section 2.4. The exceptionally short pump pulse means that the electrons in the plasmonic system oscillates under the influence of the laser for just a few cycles, whereafter the oscillation occurs freely. The short time duration also means that the pulse can excite many plasmon modes if multiple modes are supported by the system. As the duration of the pulse is inversely proportional to the range of frequencies, this can also be understood in the frequency domain by considering the large spectral bandwidth covering many modes.

2.2 Detection: Photoemission electron microscopy

The interaction of light, both the pump and the probe, with the metal nanoparticles took place in a PEEM. Electrons are emitted from the sample due to the interaction with light. The PEEM instrument then images local variations in electron emission. The light was incident at 65° to the sample normal.

One PEEM imaging mode is based on electrons being released as the result of incident light of a high frequency (one photon emission). PEEM then provides contrast in work function, topography and electron density. In the experiments described in

this thesis, a mercury lamp with a photon energy of 4.9 eV was used for imaging, and thus aided in the positioning of the sample. This photon energy is very similar to the work function for metals (4–5 eV). This means that the photoelectrons emitted initially have very low energies, which leads to a narrow energy distribution. This results in images with high spatial resolution. XUV light was also used to induce a linear photoemission process in these experiments, as described in Section 2.4.

Another imaging mode is based on the release of electrons by irradiation with light with low frequency but with high intensity (multiphoton emission). PEEM can then be used to obtain sensitive maps of the local field on the sample. In one experiment of this kind [40], observations of localized photoemission from the tips of metal nanostructures were interpreted as a signature of local field enhancement, so-called hot spots. Another experiment confirmed that local field enhancement, arising from resonant excitation of a plasmon mode, can strongly promote the multiphoton photoemission [41]. These findings provide evidence that PEEM is suitable for direct subwavelength imaging of plasmon-enhanced fields in metallic nanoparticles.

Assuming a linear relation between the incident field and the induced local field, the dependence of the photoemission on the local field on a given sample can be found experimentally. The photoemission yield, Y, is related to the incident light intensity, I, by $Y = a \cdot I^n$, where a is a proportionality constant and n is the number of photons required for photoemission [42–44]. If we take the logarithm of both sides of this equation we see that the exponent, n, is the slope of the line when the logarithm of the yield is plotted as a function of the logarithm of the intensity. As an example of this intensity dependence, Fig. 2.2a shows the measured photoemission signal summed over an array of gold bowtie nanostructures as a function of incident laser power (central photon energy 1.55 eV). Plotting the logarithm of the photoemission signals as a function of the logarithm of the laser power and fitting a linear curve to the data points, Fig. 2.2b gives the exponent n. This value was found to be 3.4, which is consistent with 3–4 photons being required to overcome the work function of gold, which is ∼5.3 eV [45].

The emitted electrons are imaged with PEEM. A schematic of the instrument used in this work (FOCUS IS-PEEM) is shown in Fig. 2.3. The objective lens consists of four electrodes: sample, extractor, focus and column. The sample is at ground potential, and the electrons are accelerated by applying a positive voltage (10–15 kV) to the extractor electrode. The electrons then pass through the objective lens. The first and second projective lenses can be active, or disabled so that PEEM operates with only one lens. The preretardation lens and retardation grid together constitutes an imaging energy filter, allowing only electrons with a sufficiently high kinetic energy to pass through. This filter was used in the studies described in Paper III. The electrons hit the microchannel plate (MCP), where the signal is amplified before being sent to the fluorescent (yttrium aluminum garnet) screen, which is imaged by a camera. The electron optics are enclosed in a vacuum chamber.

Because PEEM images electrons (with short associated de Broglie wavelengths) it provides high spatial resolution, on the nanometer scale, compared to optical microscopes. The high spatial resolution is one aspect that makes PEEM a suitable tool for studying plasmons. The PEEM used in this work has a specified ultimate resolution of 20 nm. In practice the resolution is lower than that. It depends on the light source used and on the sample. The limiting factors for high spatial resolution are mainly the four kinds of aberration described below.

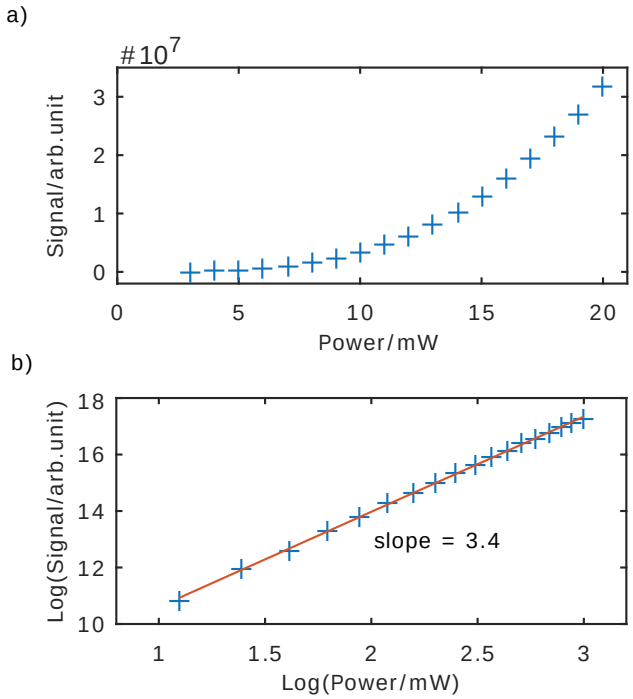

Figure 2.2: The measured photoemission signal from an array of gold bowtie nanostructures as a function of laser power in a linear plot (a) and a log-log plot (b).

Chromatic aberration arises due to a spread in the energy of the electrons. The lower the kinetic energy, the shorter the effective focal length of a lens. *Spherical aberration* arises when electrons further away from the optical axis are focused more strongly. Both these kinds of aberrations can be reduced if the initial energy is low and the acceleration energy high. These aberrations also depend on the emission angle; spherical aberration being more sensitive. The emission angle can be controlled by spatial filtering in the back focal plane of the objective lens. If a small contrast aperture is introduced, electrons emitted at only small angles will pass through. However, the use of small contrast apertures means that the number of electrons available for imaging is decreased. *Astigmatism* is caused by asymmetries in the mechanical construction, or misalignment such as the optical axis not being centered in the middle of the lenses, or the sample being tilted with respect to the optical axis. The stigmator/deflector in the PEEM can be used to compensate for these asymmetries. *Space charge effects* are other phenomena leading to a blurred image. This is due to Coulomb repulsion between electrons in a small volume, which arises primarily at the sample surface or at cross-over points in the electrons trajectories. This repulsion can lead to temporal, lateral and energy broadening. It can only be reduced by decreasing the intensity of the excitation source [46] and thus the number of electrons confined to a small volume.

Since PEEM is based on electron emission by light, it benefits from the high temporal resolution offered by light pulses in a pump–probe scheme. The temporal resolution is then only limited by the duration of the light pulses, which can be very

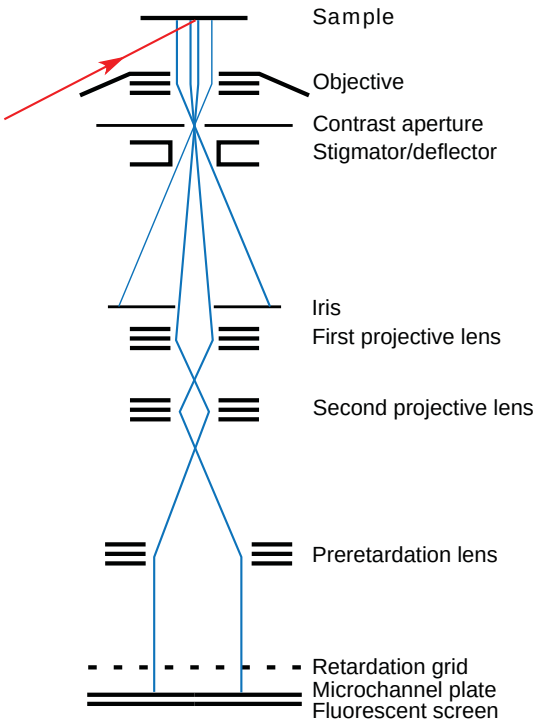

Figure 2.3: A schematic of the PEEM instrument showing its different components.

short, and the precision with which they can be delayed. The pump pulse in the experiments described here was seen to have a 6–8 fs duration, while the probe pulse had a duration of less than 6 fs. The time delay between the pulses can be finely scanned, down to 10 as. In both experiments, an IR-pulse would initiate the plasmon dynamics in the nanostructures being studied. The probe pulse then, ideally, causes the photoemission. For an exposure time of 1 s and a pulse repetition rate of 200 kHz, the photoemission from 200 000 excitations are recorded providing a single image.

2.3 Probe: IR pulse

Nonlinear near-field autocorrelations can be measured with PEEM by splitting the IR-probe pulse into two pulses and introducing a time delay between them [24]. Conceptually, each point in such a trace is the time-integrated signal due to the near-fields caused by the two individual pulses. The total near-field changes, as does the photoemission signal, when the delay is scanned. Let us consider, for example, two individual near fields induced with a time delay such that they are out of phase with each other. For this time delay, a low photoemission signal is expected during the exposure time. If, on the other hand, the two near fields are induced so that they are in phase with each other, high photoemission is expected. In other words, for a given delay, the two pulses can confine the charge to a higher and lesser degree over the duration of the two pulses and the ringing of charge that follows, leading high photoemission if the charge is highly confined and low emission if it is not. As the delay between the

pulses is varied, the amount of total charge confinement changes. Hence the resulting photoemission changes with delay. Mathematically, what is measured with PEEM in such experiments is, at a given point on the sample, is;

$$S(\tau) = \int_{-\infty}^{\infty} |E_z(t) + E_z(t+\tau)|^n dt \tag{2.1}$$

where S is the photoemission signal for a given time delay τ, $E_z(t)$ is the component of the electric field normal to the object as a function of time, and n the number of photons required for photoemission.

While it is not possible to reconstruct the complete time-domain near field from such a recorded auto-correlation trace, some information can still be obtained about it. A closer spacing between the fringes in a trace corresponds to a higher oscillation frequency of the near field, as discussed in Paper V. More generally, since PEEM simultaneously measures near-field autocorrelation traces from different particles within the same field of view, any measured differences in these traces shows that the particles have a different near-field.

The free electron oscillation, occuring after the pump pulse has passed, can only be probed using a very short probe pulse, as it lasts for only ∼10 fs [10]. For few-fs pump and probe pulses, for example, most of the induced field, and thus the photoemission, is dictated by the system itself, and only a small part is fully controlled by the laser pulses. We used a 6 fs IR pulse for the pump and probe, which made the measurement sensitive to these intrinsic dynamics. The intrinsic dynamics is interesting to get hold off for applications such as coherent control [34], harmonic generation [35] and electron acceleration [36, 37].

2.4 Probe: XUV pulse

A more direct measurement of the full plasmonic field could be achieved by using a much shorter probe pulse. With this short pulse snapshots could be taken of the field at different delays. To achieve a much shorter pulse than the IR pulses described above, the period of the carrier wavelength has to be drastically reduced, as a pulse cannot be shorter than one period of its carrier. In the process of high-order harmonic generation (HHG), pulses with frequencies in the XUV part of the spectrum, and with a duration on the attosecond timescale (10^{-18} s), can be created. Such pulses are used today to probe electrons in atoms and molecules on their natural timescale.

2.4.1 Principle of HHG

HHG was discovered in 1987 [13]. A spectrum of odd high-order harmonics of the fundamental frequency was observed when illuminating a gas with a strong laser field. The spectrum included a region of harmonics with comparable intensity (forming the so-called plateau) and a region of higher orders where the intensity dramatically decreased, the so-called cut-off region. Figure 2.4 shows the higher energy part of a measured HHG spectrum, including the plateau and cut-off regions. As the driving laser wavelength in that measurement was 1030 nm, the harmonic orders shown range from 45–25 nm (28–49 eV).

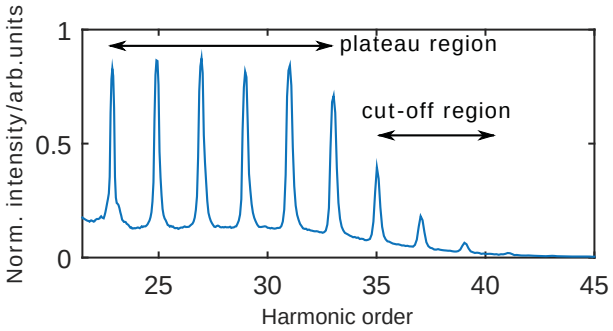

Figure 2.4: A typical experimental high-order harmonic spectrum, showing the upper energy part. The plateau region and the cut-off region are indicated. This spectrum was generated by 170 fs laser pulses with 1030 nm wavelength.

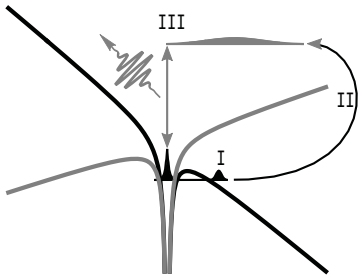

Figure 2.5: The three-step model: 1) tunneling, 2) acceleration and 3) recombination. Image courtesy of David Kroon.

In 2001 it was confirmed that high-order harmonic spectra can support pulses with a duration of a few hundreds of attoseconds [14]. Meanwhile, the understanding of the microscopic mechanism behind HHG had developed. While a fully quantum mechanical treatment of the process describes the process in the most complete way [47], a semi-classical description [48] of HHG is adequate for the purposes of this thesis. The semi-classical model explains the presence of the plateau in the HHG spectrum.

HHG can occur when a laser pulse is focused into a gas. The laser pulse will interact with many atoms as it travels through the gas. Let us start by considering the interaction with one atom. As the pulse consists of several optical cycles, the atom will interact with the pulse during all these cycles. For a pulse consisting of many cycles, the interaction will be approximately the same for every half-cycle. Let us then first consider the interaction during one half-cycle.

In the semi-classical description, HHG consists of three steps, as illustrated in Fig. 2.5. The first step is tunneling-ionization. If intensities on the order of 10^{14} W/cm^2 are reached, the electric field strength of such pulses is comparable to the Coulomb field binding a valence electron to the atom. When the electric field is near its maximum, the total potential of the atom and the potential resulting from the field add, forming a barrier sufficiently small for an electron to tunnel through. The atom is thereby ionized. The second step, acceleration, occurs when the field changes sign. The electron is accelerated in the applied electric field, thereby gaining kinetic energy. The

average kinetic energy, U_p, that an electron can gain in an electric field is given by $U_\mathrm{p} = e^2E_0^2/4m\omega^2$, where E_0 is the amplitude of the field and ω the angular frequency of the field. As the electron is accelerated back towards the parent ion it may recombine with it, recombination being the third step. The time of tunneling with respect to the phase of the laser field determines both whether the electron is actually driven back to the parent ion and the energy it acquires. This is illustrated in Fig. 2.6. Figure 2.6a shows some calculated electron trajectories for different tunneling times. It can be seen that only some trajectories lead back to the parent ion. These trajectories are plotted in Fig. 2.6b. Electrons tunneling early and recombining late follow the long trajectories while electrons leaving late and recombining early follow the short trajectories. Figure 2.6c shows the kinetic energy upon recombination as a function of return time. The highest energy ($3.2U_\mathrm{p}$), the cut-off energy, corresponds to the trajectory represented by the blue curve in b). All other energies result from both a short and a long trajectory. The recombination leads to the emission of an attosecond pulse. The energy acquired by the electron, E_kin, together with the ionization potential of the atom (the energy required to remove the most loosely bound electron from the atom), I_p, is transferred into photon energy, E_phot, according to:

$$E_\mathrm{kin} + I_\mathrm{p} = E_\mathrm{phot} \tag{2.2}$$

The maximum photon energy is thus:

$$I_\mathrm{p} + 3.2U_\mathrm{p} = E_\mathrm{phot,max} \tag{2.3}$$

As U_p is proportional to the laser intensity and the square of the wavelength, the cut-off energy can be increased by using a higher intensity (up to the saturation intensity at which the atom is ionized with a probability of ~ 1) or a longer wavelength. Today, it is possible to generate harmonics with a photon energy of 1.6 keV (7.7 Å), corresponding to the 5000th order [49].

As can be seen in Fig. 2.6c, the range of kinetic energies gained by the electrons is continuous. Thus, the emission from an atom during one half-cycle is continuous in frequency. The discrete harmonic orders in Fig. 2.4 result from a repetition of the process, which is discussed below. The different kinetic energies, corresponding to different trajectories, are obtained with similar probabilities. This explains the plateau shape of the harmonic spectrum, where the different harmonics have similar amplitudes.

In a hand-waving quantum mechanical picture, the ionizing electron wave packet takes all trajectories after tunneling. A small part of the wave packet tunnels out and accelerates. An electron with a high energy is described by a plane wave of short wavelength. When the electron wave packet is driven back to the atomic system it interferes with the ground state. As the free part moves over the bound part this system forms an oscillating dipole. The dipole first oscillates at relatively low frequencies, due to interference with part of the electron taking a short path leading to less energy, after which it oscillates at high frequencies, due to the electron following the path leading to the highest energy, and then it again oscillates as lower frequencies, due to the part of the electron taking the long trajectories. The light emitted by dipole is continuous in frequency, chirped and has a large bandwidth.

The process of HHG repeats itself every half-cycle of the laser pulse. Every time the field is close to its maximum, an electron tunnels out, accelerates and recombines,

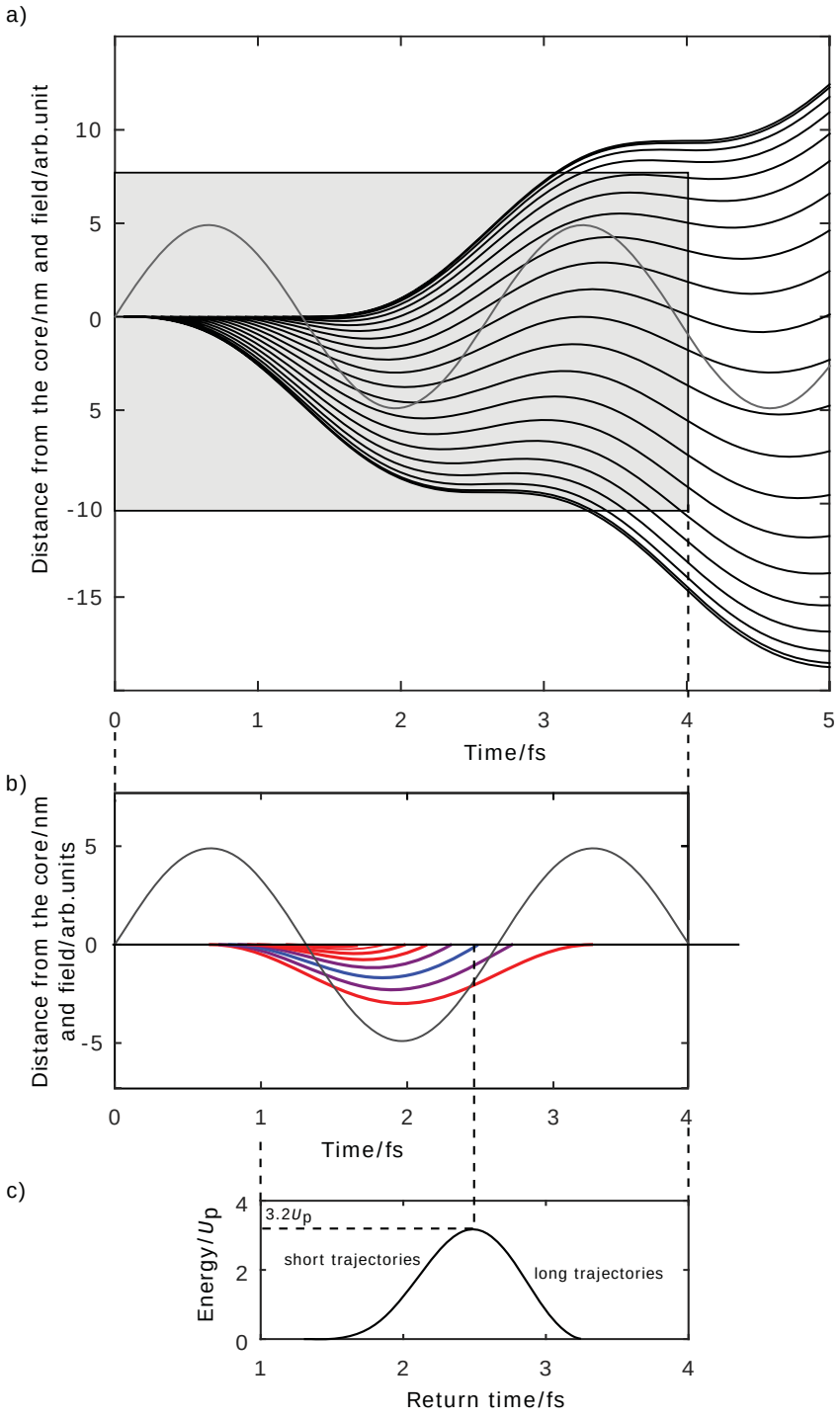

Figure 2.6: The electron trajectories in an oscillating laser field and associated return energies. a) The calculated electron trajectories. Most of the electrons do not return to the origin, or zero-position. b) The trajectories that lead to recombination. The corresponding kinetic energies are indicated by different colors: blue indicating high energy and red low energy. c) The kinetic energy upon return to the atom. The electrons returning early (taking the short trajectories) and those returning late (taking the long trajectories) gain a relatively low energy. The trajectory in between corresponds to a high kinetic energy. The trajectories were calculated by assuming an electric field amplitude of $4.9 \cdot 10^{10}$ V/m and a period of 2.6 fs.

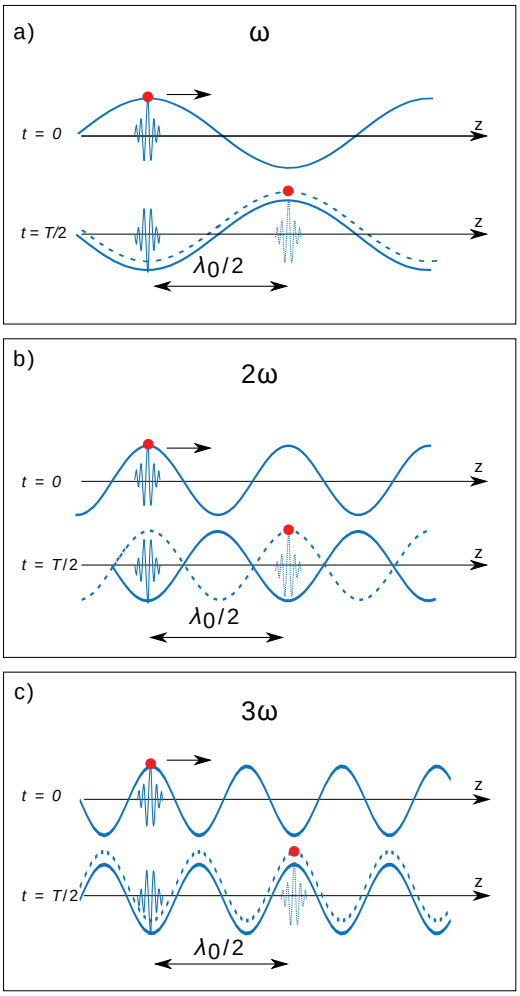

Figure 2.7: The first three harmonics of attosecond pulses generated at $t = 0$ and $t = T/2$ as a function of z. a) The first harmonic. The waves associated with the two attosecond pulses appear in phase. b) The second harmonic. The waves are out of phase. c) The third harmonic. The waves associated with the two consecutive attosecond pulses are in phase.

producing an attosecond XUV pulse. Thus, a train of attosecond pulses is produced during a single laser pulse. As a laser pulse has to be very short in order to produce just one attosecond pulse, the generation of single pulses is challenging. There are, however, techniques to isolate attosecond pulses [50].

Two consecutive attosecond pulses have opposite phases. This can be understood by considering that the dipole causing the attosecond pulse starts oscillating in opposite directions in the two half-cycles. The dipole will start its oscillations in opposite directions because the free electron, described by a wave packet, will come from opposite directions due to the opposite sign of the driving field in the two cases.

An attosecond pulse train corresponds to a spectrum of odd harmonics in the frequency domain. A simple picture is sufficient to understand why only the odd harmonic frequency components survive over the half-cycles, despite the continuous range of frequencies emitted each half-cycle. Figure 2.7 exemplifies the constructive interference of odd harmonics and the destructive interference of even harmonics. Let us study the generation of two attosecond pulses, separated in time by half a cycle, and the way in which their associated frequency components interfere. The first pulse is generated at $t = 0$ and the second at $t = T/2$. Here, T is the period of the fundamental, the driving field, and λ_0 its wavelength. In 2.7a the first attosecond pulse is generated at $t = 0$ and the ω component is shown as a function of the spatial direction z. At $t = T/2$ this wave has traveled half of its wavelength (dashed line). The displacement of the wave is indicated by the shift of the red marker. But as half a cycle has passed, a new attosecond pulse has been emitted. As described just above, this attosecond pulse is emitted with opposite phase to the first one. As can be seen, the ω wave of the attosecond pulse emitted at $t = T/2$ (solid line) is in phase with the ω wave of the attosecond pulse emitted at $t = 0$ (dashed line). Let us now consider the case for the second harmonic, depicted in Fig. 2.7b. The figure shows the 2ω component of the attosecond pulse generated at $t = 0$. After $T/2$ this wave has moved $\lambda_0/2$, *i.e.*, its own wavelength, indicated by the displacement of the wave. At this time, the atom has emitted the second attosecond pulse, with opposite phase to the pulse generated at $t = 0$. The second harmonic of the $t = T/2$ pulse (solid line) is out of phase with the second harmonic of the $t = 0$ pulse (dashed line). Fig. 2.7c illustrates the case of the third harmonic. The 3ω component of the attosecond pulse generated at $t = 0$ is shown. After half a period of the driving laser, this 3ω wave has propagated $\lambda_0/2$, one and a half times its wavelength, as indicated by the shift of the wave. The 3ω component of the attosecond pulse generated at $T/2$ (solid line) is also shown. This wave is in phase with the 3ω component of the previously generated attosecond pulse (dashed line), resulting in constructive interference. It has thus been demonstrated that the odd harmonics interfere constructively and the even harmonics interfere destructively, when the interval between emissions is $T/2$ and each harmonic is emitted out of phase with respect to the former one. This explains the appearance of the odd harmonics in Fig. 2.4. The other components, not at harmonic frequencies, interfere neither constructively or destructively, and remain over a few cycles. However, if the pulse is long, they disappear and the odd harmonics become more well-defined. This simple picture can be used to explain at least two other scenarios. A periodicity of HHG of T, which means that every harmonic is emitted with the same phase, results in constructive interference for both even and odd harmonics [51]. If the periodicity of HHG is $T/2$ and every harmonic still is emitted with the same phase, only even harmonics interfere constructively [52].

Noble gases are often used as generation media. Due to differences in their ionization potential, the generation of high-order harmonics has different characteristics for different noble gases. A low ionization potential means that the probability of tunneling-ionization is relatively high, which leads to a high flux. The use of gases with a high ionization potential can instead lead to higher obtained harmonic orders, as the intensity of the driving field can be increased without causing significant ionization. Xenon, krypton, argon, neon and helium (in order of increasing ionization potential) are commonly used for HHG.

To fully reconstruct the harmonic emission, both the amplitude and phase of each harmonic order must be known. Each harmonic order consists, as shown, of two contributions, the short and long trajectory contributions. The amplitude of both contributions to each harmonic order can in principle be obtained from a spectrum, but it is more difficult to determine their phase. Today, attosecond pulse trains with a dominant contribution from one of the trajectories can be fully characterized. One such technique is called reconstruction of attosecond beating by interference of two-photon transitions (RABBITT) [14, 53]. Here, the short trajectory contribution to the harmonic emission and the relative phase between each harmonic is measured. The relative phase between the two contributions to each harmonic order is, however, not accessible. This phase could be obtained by investigating the interference between the short and long trajectory contributions [54]. Such a measurement would, in combination with RABBITT, for example, make possible the full reconstruction of the harmonic emission: the phases of each harmonic order relative to each other and the relative phase of the contributions constituting them.

To understand this better, let us consider the dipole phase. It is the phase of the dipole formed when the electron wave packet interferes with the ground state. It depends on the harmonic order, the trajectory and the intensity, I. For a given harmonic order and trajectory short(s) or long (l), we have

$$\Phi_{s,l}(I) = \phi^0_{s,l} - \alpha_{s,l} I \tag{2.4}$$

where $\phi^0_{s,l}$ are constant phases and $\alpha_{s,l}$ are the coefficients. $\phi^0_{s,l}$ and $\alpha_{s,l}$ are called dipole phase parameters.

With RABBITT the difference in dipole phase between the harmonic orders, for the short trajectory, can be obtained. The absolute phases are unknown, but these are not needed for the reconstruction. We can thus set the phase of the short trajectory, lowest harmonic order, to zero, for simplicity. If also, for that order, α_s is measured, ϕ^0_s can be calculated, (Eq. 2.4). Measuring additionally α_l and ϕ^0_l-ϕ^0_s would then give the full information about the phases of both the short and long trajectory contributions for the lowest order. With the knowledge of the relative phase between Φ_s for the lowest order and the next, the same information can be obtained for the next order. This way, the emission from all harmonic orders could in principle be fully reconstructed. In this work, α_s, α_l were measured for several harmonic orders. The same experiment has the potential to additionally provide information about ϕ^0_l-ϕ^0_s. This thus paves the way for a full reconstruction of the harmonic emission. The measurement is described in Paper VIII and in Section 4.2.5.

The contributions of the long and short trajectories to the harmonic signal have different divergences and spectral widths. The long-trajectory contribution is both more divergent and spectrally broad than the short-trajectory contribution. Both

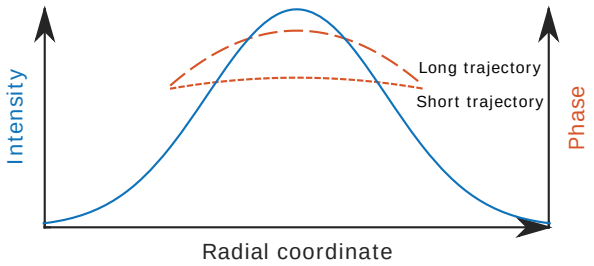

Figure 2.8: The intensity of the fundamental, phase of the short trajectory and phase of the long trajectory as a function of the radial coordinate, r. A larger variation of the phase of the long trajectory can be observed.

aspects can be understood by considering the field of one harmonic order q:

$$E(r,t) \propto e^{i(q\omega t - \Phi(r,t))} = e^{i(q\omega t - \phi^0 + \alpha I(r,t))} \tag{2.5}$$

As the dipole phase parameter α is larger for the long trajectory than for the short trajectory, and the pulse intensity varies over r, the radial coordinate, there is a greater difference in phase in the transverse plane for the long trajectories than for the short ones. Fig 2.8 illustrates how the two phases depend on r. As the laser beam can be approximated by a Gaussian beam, the intensity has a Gaussian dependence on r. At the region of maximum intensity, however, where most of the XUV light is generated, it can be approximated by a quadratic curve. As the phases of the short and long trajectory are proportional to the driving field intensity, they also have quadratic dependences in this region. The larger variation over r for the phase of the long trajectory results in a larger divergence for the long-trajectory light. The smaller divergence of the short-trajectory contribution makes it attractive for use in attosecond experiments.

The instantaneous frequency is the time derivative of the phase:

$$\omega(t) = \frac{d(q\omega t - \phi^0 + \alpha I(t))}{dt} = q\omega + \alpha \frac{dI(t)}{dt} \tag{2.6}$$

The spread in the instantaneous frequency of the harmonic order is thus larger for the long trajectory than for the short trajectory as $\alpha_l > \alpha_s$. This will be manifested as a broader spectral contribution from the long trajectories than from the short ones for a given harmonic order.

The above reasoning was for a single atom, but the illuminated gas consists of many atoms, which particpiate in HHG. The contribution from all the participating atoms forms an XUV beam propagating collinearly with the laser. In order to obtain efficient XUV radiation, the atoms must emit radiation in a way that the radiation emitted by one atom is in phase with the radiation emitted previously from another atom, in order to ensure constructive interference. The radiation is then said to be phase-matched. The long-trajectory contribution is, in general, difficult to phase match.

A HHG process is dependent on the polarization of the driving field. The process is most efficient for linear polarization, which has been assumed above. Intuitively, for elliptically polarized light, an electron has a reduced probability to recombine with the parent ion since the electric field has a component in the transverse direction (Fig.

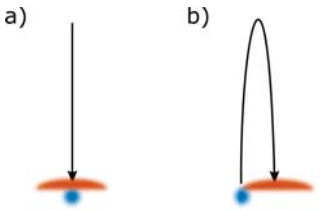

Figure 2.9: The location of the returning electron relative to the location of the parent ion in the case of a) linear polarization and b) elliptical polarization. The shift of the electron in the latter case leads to in a smaller overlap between the electron and the parent ion.

2.9). It is also expected that, an electron following a long trajectory will have less probability to recombine than an electron following a short since the long trajectory electron spends a longer time in the continuum.

The ellipticity dependence of the short trajectory electrons has been studied experimentally and theoretically. The semi-classical three-step model describes the observed dependence well. As can be seen in Fig. 2.6c, the short trajectory electrons with high energy spend a longer time in the continuum than the electrons with lower energy. It is thus predicted that they will be more sensitive to deviations from linear polarizations, as has indeed been observed [55–57]. In Paper VII and Section 4.2.4, the ellipticity dependence of the long trajectory contribution, measured in this work, is described.

2.4.2 Technical implementation of HHG

The technical implementation of HHG is difficult. The laser intensities needed, $\sim 10^{14}$ W/cm^2, are usually achieved by energetic pulses with short durations, produced by large high-power systems. Two technologies are relevant for this work. Both technologies are based on chirped pulse amplification (CPA): the pulse is stretched, amplified in a crystal and then compressed. But the amplification, *i.e.* the transfer of energy from the pump beam to the signal beam (the beam to be used) is realized differently in the two technologies: the conventional one uses population inverted media while the more recent technology uses a parametric process (optical parametric amplification, OPA, the technology including the CPA is then called OPCPA). The use of population inverted media for amplification has long been the method of choice in producing the shortest and most energetic pulses. However, it is difficult to obtain pulse durations below $\sim$ 20 fs, because of gain-bandwidth narrowing. The heat deposited in the amplification crystal often limits the pulse repetition rate to a few kHz. In OPA the energy transfer from pump to signal occurs differently than in schemes exploiting population inverted media. A pump pulse with similar duration to the stretched signal pulse, is nonlinearly mixed with the seed pulse in an optical crystal, resulting in amplification of the signal pulse and emission of an idler pulse. No energy is being stored in the crystal, and heat dissipation is therefore negligible. Laser pulses at high repetition rate ($\sim$MHz) can thus be obtained with OPCPA laser systems. Pulses shorter than 10 fs can be amplified with non-collinear pump–signal geometries.

A consequence of the use of large high-power systems is that the HHG is limited to a few laboratories with the necessary equipment and expertise. This is unfortunate,

as the plasmonics community, and researchers in other fields, including femtosecond chemistry and surface science, could benefit from access to HHG. Investigating the possibility of, and characterization of, HHG using less complex laser systems is therefore of interest. In this work, HHG was achieved using a turnkey laser system. This is described in Paper II and in Section 4.2.3.

2.4.3 PEEM combined with HHG

We will now consider the combination of PEEM with XUV pulses. The idea is to induce a plasmon in the nanostructure using an IR pulse. The electron density will then vary over time at every location in the structure. Electron emission should then mainly be caused by the incident attosecond pulse. The emission from a specific point depends on the electron density at that point. By varying the delay between the IR pulse and the attosecond pulse it should be possible to detect oscillating photoemission, representing the oscillating electron density. One PEEM image is taken for each delay, so over the PEEM images an oscillation in signal is expected. If only one attosecond pulse is produced per IR pulse, the attosecond pulse can be used to map the full plasmonic field, and beating between several modes can, in principle, be observed. However, to obtain only one attosecond pulse per femtosecond pulse is, as seen, challenging. The access to a full train of attosecond pulses, with one attosecond pulse for each half-cycle of the femtosecond pulse, is more straight forward. In this case, the full plasmonic field cannot be mapped. Also, it may in this case happen that no oscillations in photoemission signal can be observed. For one half-cycle the electron density might be high and cause a high photoemission. In the next half-cycle the density is lower than average and thus causes a low photoemission. During the exposure time of the PEEM image, these contributions could together produce a signal equal to the signal obtained when the attosecond pulses probe the zeros of the field at the sample. Thus, there is a risk that no oscillation as a function of delay would be observed. With one attosecond pulse produced per optical IR cycle [51], this problem is avoided and one plasmonic cycle could potentially be probed. The most straight forward solution would, however, be to have only one attosecond pulse for each femtosecond pulse.

The use of XUV pulses leads to a large photoemission during a very short time determined by the attosecond pulse duration. This can lead to space-charge effects, and hence blurring of the image. This aberration can be reduced by decreasing the intensity of the XUV pulses [17], which leads to a smaller photoemission. However, this reduction in total photoelectron flux decreases the signal-to-noise ratio in the image. Attempts to improve the signal-to-noise ratio often lead to impractically long exposure times.

The paper by Mikkelsen *et al.* describes the situation before the work on this thesis started [17], see also Paper III. They used a titanium sapphire-based laser system at the Lund high power laser facility, delivering IR pulses of 35 fs duration centered at 800 nm, with a pulse energy of ∼3 mJ [17]. It is based on amplification using a population inverted medium and operates at 1 kHz, and is therefore called the "kHz system". It was shown that the attosecond pulse trains generated provided sufficient average photon flux for PEEM experiments. In order to avoid space-charge effects the XUV beam had to be attenuated. Figure 2.10a shows a scanning electron microscope (SEM) image of a silicon substrate patterned with gold using electron beam lithography (EBL). In Fig. 2.10b a PEEM image of the same sample obtained

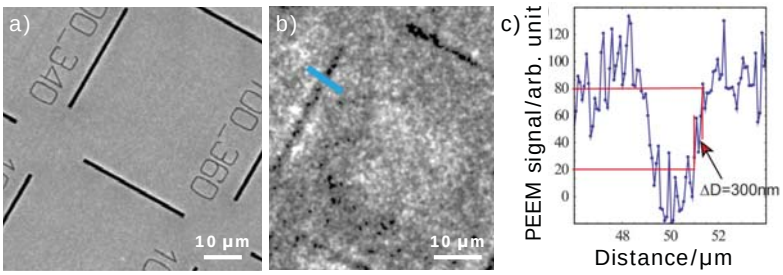

Figure 2.10: Images of the same lithographic sample. a) SEM b) PEEM using XUV radiation as light source. c) The intensity profile over the line indicated in b) [17].

under illumination of the XUV beam is shown. The spatial resolution using XUV pulses was estimated. For this, the slope of one edge of the signal profile across the 1 µm wide lithographic line, shown with the blue line in Fig. 2.10b was investigated. The distance 300 nm was measured from 20% from the bottom to 80% of the top as shown in Fig. 2.10c. In other images 200 nm wide lines can be seen. The authors therefore estimated the spatial resolution using XUV pulse trains to be 200–300 nm. By noting the smallest observable feature with the PEEM using the mercury lamp a spatial resolution of 50/100 nm (without/with running turbo pumps) was found. It was noted that the spatial resolution of the measurements using XUV pulses was limited by the energy spread in the photoelectron beam. No energy filtering was, however, available at this time and the use of such a filter would have resulted in a lower electron flux.

XUV pulse trains generated at a higher repetition rate could provide a way forward, as the number of electrons emitted per attosecond pulse could be kept low, while obtaining sufficient signal from the number of pulses. It would also be possible to energy select some electrons, thereby reducing chromatic aberrations. Several studies report the generation of high-order harmonics at high repetition rates (50 kHz–136 MHz) [35, 58–71]. One of the strategies used to achieve sufficiently high intensities despite the low pulse energy associated with high repetition rates is to focus the laser beam tightly onto the HHG medium [58, 61, 63–70]. This will affect the phase matching of the two sets of trajectories. The short-trajectory contribution will be less phase matched in this scheme, and its strength can be comparable to the contribution from the long trajectories. This thesis describes HHG at 20–400 kHz repetition rate, in Chapter 4 and Papers II, IV, VII and VIII.

Many processes can take place during the interaction of the XUV radiation with the solid. Electrons can be emitted by direct photoemission (primary electrons), or by subsequent interactions between electrons (secondary electrons). Secondary electrons have lower energy than the primary electrons. In the originally proposed scheme for attosecond PEEM experiments [16], making use of the primary electrons was suggested. Primary electrons are, in general, difficult to image, as described next.

For good image quality, the PEEM instrument must be well focused and aligned. When imaging with XUV light, the number of photoelectrons emitted is rather low, if space-charge effects are to be avoided. The mercury lamp can be used instead of the XUV pulses to obtain good settings. As the secondary electrons have energies similar to the electrons emitted by the mercury lamp these are as a result fairly well

focused. The primary electrons, however, have higher energies, which forbids the settings obtained with the mercury lamp to be successfully used in this case. Thus, suitable PEEM settings have to be found using the primary electrons themselves. The primary electrons constitute less than 10% of the full electron yield, so probing only these would lead to even longer exposure times using XUV at 1 kHz. It is thus interesting, but challenging to image the primary electrons. In this work, successful imaging using only the primary electrons were accomplished, described in Paper III and Section 4.3.

As the secondary electrons constitute more than 90% of the total electron yield, it is advantageous if they too can be used in attosecond experiments. The possibility of this depends on the time scale on which they are released. If they are released over several cycles of the plasmon field they cannot easily contribute to the mapping of the field. If, on the other hand, they are emitted over a much shorter time, they can be a valuable part of the detected electron signal. The usability of secondary electrons in time-resolved measurement was investigated theoretically in this work and the results are presented in Paper I and Section 4.1.

Another important factor for successful IR–XUV experiments is the ability to detect an oscillation in photoemission signal due to the XUV pulses. The pump IR pulse must be strong enough to change the electron density over the nanostructure but if the resulting field enhancement is sufficiently high, it will itself lead to photoemission. The photoemission signal due to the IR pulses could therefore lead to a constant background. Thus, the oscillation in photoemission signal due to the XUV pulses must provide a sufficiently strong oscillating signal so that it can be detected above that background. The signal due to XUV pulses compared to IR pulses was investigated in this work and the results are also presented in Paper I and Section 4.1. In this paper and this section, some other factors of importance for the implementation of an IR-XUV experiment are additionally discussed. These factors include the choice of sample and required exposure times for imaging.

2.5 Nanostructure fabrication method: Focused ion beam

The FIB method is commonly used for nanostructure fabrication. It is capable of producing structures with dimensions as small as ∼10 nm [72]. During FIB milling, a focused ion beam interacts with the solid so that atoms are sputtered from its surface. FIB is not only used for milling, but commonly also for imaging. In this case, the detectors usually collect secondary electrons from the ion collision process. The result of this is that atoms are removed from the imaged area, and the area is slightly milled.

One of the advantages with the FIB technique is that it is a direct write method, and does not require the application of a resist layer, as in EBL, for example. In many FIB instruments, including the one used in this work, the ion gun and electron gun can be used interchangeably, so that a milled area can be inspected with SEM directly after milling. Feedback is thus much faster than in the case of EBL, where the final result is known only after the deposition of the resist, exposure to electron gun, developing, evaporation and lift-off. The controlled production of small features, such as a ∼20 nm gap between two nanostructures is difficult with both EBL and FIB. FIB was chosen due to the instant feedback.

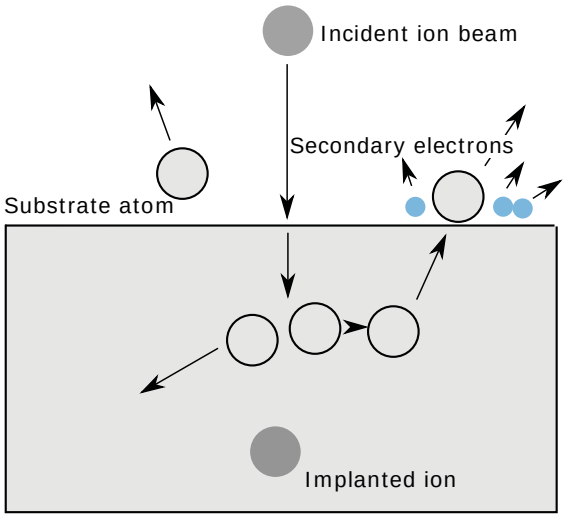

Figure 2.11: Results of some interactions between an incident ion beam and a solid. The cascade between atoms leads to emission of atoms (neutral or charged) and electrons from the surface. The incident ions are typically implanted into the solid.

2.5.1 Ion–solid interactions

The processes of milling and imaging using FIB, are based on interactions between ions and the solid [72, 73]. The kinetic energy of the ion is transferred to the solid through both inelastic and elastic interactions. In inelastic interactions, called electronic energy loss, ion energy is lost to electrons in the sample. This results in ionization and the emission of secondary electrons and electromagnetic radiation from the sample. In milling, the elastic interactions, called nuclear energy loss, are of greater importance. In this case, ion energy is transferred to a substrate atom. If the transferred energy exceeds a certain critical value, the atom will be knocked out of its original crystal site. If this atom has sufficient energy, it may displace other atoms in the material, leading to a collision cascade. If a displacement collision occurs near the surface, the recoil atom (neutral or charged) may be emitted from the solid, resulting in sputtering. The sputtering process is the basis of FIB milling. Some of the possible ion–solid interactions are shown in Fig. 2.11.

Some undesirable effects may result from ion–solid interactions. One is ion implantation. During the collisions, the incident ion looses energy. Thus, if the ion is not backscattered, it will come to rest, and become implanted in the target at some depth. Sputtered material may be deposited on surfaces in close proximity to the active milling site. This is mostly problematic when milling deep holes, and can lead to an undesired V-shape [73]. A third effect is ion channeling, and depends on crystal orientation. In this process, ions may penetrate greater distances along low-index directions compared to non-channeling directions or in amorphous materials. In polycrystalline materials, this can lead to a variation in the ion penetration depth as the beam scans over regions of different crystal orientation.

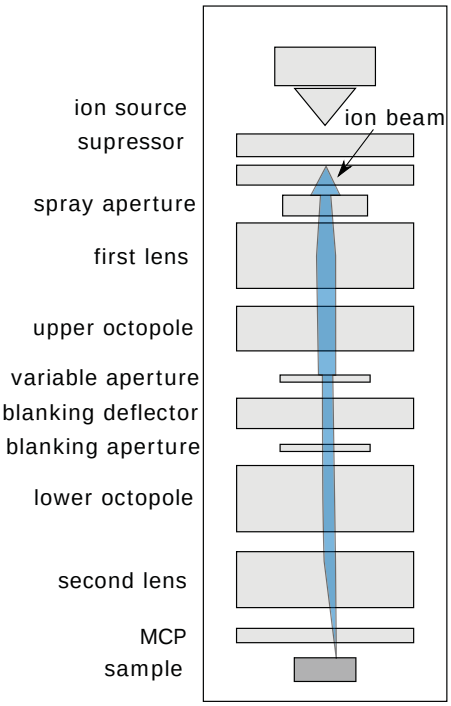

Figure 2.12: A schematic of the various components of a general FIB instrument.

2.5.2 The instrument

The general FIB instrument consists of a vacuum system and chamber, an ion source, an ion column, a sample stage, detectors and a computer to run the system [72, 73]. The instrument is very similar to a scanning electron microscope.

A vacuum system is required in order to avoid contamination and to prevent electrical discharges in the high-voltage column. In the sample chamber vacuum is necessary so that the particles can travel without too many collisions with gas atoms or molecules.

The type of ion source most commonly used is the liquid–metal ion source. These can provide a beam of ions of $\sim$5 nm in diameter, enabling the removal of material with high lateral resolution. The source often contains a tungsten needle attached to a reservoir containing the metal source material. Several metals can be used as ion sources for FIB. Gallium is the most common one, and was used in the present work. This is due partly to its low melting temperature (30°C) and partly to its low vapor pressure. The low melting temperature allows for easy design and operation, and as evaporation is limited, the source lifetime is long.

Once the Ga^+ ions are extracted from the source they are accelerated down the ion column. Charged particles are easier to focus if the acceleration voltage is high and an ion voltage of 30 keV was used in this work. A schematic of the FIB column is shown in Fig. 2.12 [74]. After the spray aperture has refined the beam, it is condensed by the first electrostatic lens. Stigmatism is adjusted by the upper octopole. The beam current can be set to one of, typically, seven values ranging from 1 pA – 8 nA, using

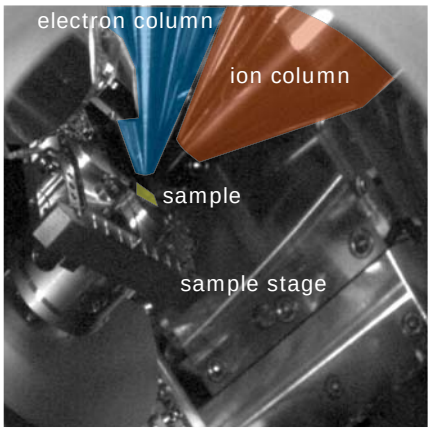

Figure 2.13: A photograph of the FIB/SEM vacuum chamber, where the electron column, the ion column, the sample and the sample stage are indicated. The colors have been added to improve clarity.

the variable aperture. The beam can be stopped from reaching the sample, by the blanking deflector and aperture. The lower octopole is used to scan the beam over the sample in a user defined pattern. The beam is focused to a fine spot by the second electrostatic lens. The MCP collects secondary particles for imaging. The stage on which the sample is mounted can usually be moved in the x, y and z directions, and can be rotated and tilted.

Figure 2.13 shows a photograph of the vacuum chamber of the FIB/SEM instrument used in this work (FEI NanoLab 600). If the sample is tilted 52°, as in the figure, it faces the ion column normally. This is the position used for milling. Note that directly after milling, the electron source can conveniently be used to inspect the milled feature from the side. The sample is attached to the FIB/SEM stage via a clamp (not shown). Electrical contact between the metallic film on the dielectric substrate and the metallic clamp is important to ensure that the film is grounded, as charging of the metallic film reduces the quality of the SEM image.

The time during which the ion beam resides on each pixel during scanning is called the dwell time. The ion beam can scan the same area several times, doing a certain number of passes. The result of scanning is that charge is deposited on the exposed area. A common quantity used to describe a certain FIB milling routine is the area dose. The area dose is either the amount of charge, or the number of ions, deposited on a given area. To calculate the area dose, Dose_Q, in terms of the charge deposited, Q, on the area A, it is necessary to know the area, the current, I, the number of scanned pixels, N_{pix}, the dwell time, t_d and the number of passes N_{pass}:

$$\mathrm{Dose_Q} = \frac{Q}{A} = \frac{Q}{t_{scan} \cdot A} \cdot t_{scan} = \frac{I \cdot t_{scan}}{A} = \frac{I \cdot N_{pix} \cdot t_d \cdot N_{pass}}{A} \tag{2.7}$$

where t_{scan} is the total scanning time. The area dose Dose_Q has the units $\mathrm{C/cm^2}$. Since the used ions are $\mathrm{Ga^+}$, each ion is charged by $-e$. The number of deposited ions per area is thus given by dividing the result of Eq. (2.7) by this ion charge.

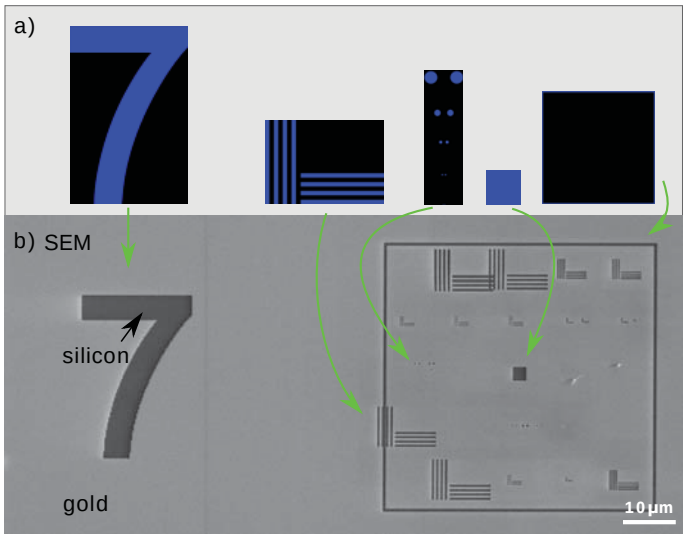

Figure 2.14: Examples of milled patterns. a) The image-files used: the number seven, horizontal and vertical lines, filled circles, a square and a frame. b) SEM image of the resulting patterned gold film.

FIB is flexible regarding pattern creation. Circles, squares and other polygons can easily be drawn using the software and milled directly. Another useful feature is the ability to load bitmap files into the software. This allows for milling of any two-dimensional pattern. Apart from the nanostructures of interest, this makes it easy to pattern large indicators on the sample, such as arrows or numbers, for navigation.

As an illustration of the flexibility in pattern design, Fig. 2.14 shows bitmap images and the resulting patterned area imaged by SEM. The bitmap images have black and blue areas. The beam is blanked over the black areas. The pixel value of the blue RGB component determines the dwell time. For a value of 0, the dwell time is 100 ns and if the value is set to 255 the dwell time set elsewhere in the user interface is used. The dwell time for the pixel values between 0 and 255 is linearly interpolated between 100 ns and the dwell time set by the user. In this work, the blue component was set to 255, as in Fig. 2.14a, and the dwell time was set in the user interface. The area dose using bitmap images is then determined by the number of pixels scanned in the loaded image file, the dwell time, the number of passes, the milled area and the current. The sample shown in Fig. 2.14b, consisting of a thin gold film on a silicon substrate, was used to test the resolution of a confocal optical microscope for detection of single impurities in a bulk crystal [75].

The beam spot size in FIB is mainly limited by the chromatic aberration resulting from the energy spread of the beam due to space charge effects by the ion source [72]. Spherical aberration caused by the lenses also plays a role. Lower currents should reduce the space-charge problems, and indeed, small beam sizes are obtained with lower currents, *e.g.* 1 pA. The smallest beam size commonly obtained today is about 5–7 nm [73]. The FIB instrument used in this work has a specified beam diameter of 7 nm at 1 pA. This current was used for milling of the plasmonic structures. It was observed that higher currents, for example 10 pA, indeed gave less well-defined

nanostructures. However, the smallest achievable feature size depends not only on the beam size, but also on the ion–solid interaction, and is around 10 nm [72]. It should be noted that the FIB instrument used in this work is optimized for a wide range of structure sizes, so fabrication on this scale means pushing the machine to its limits. For finer fabrication, FIB using helium ions is a suitable alternative [76].

2.5.3 Choice of material

Gold and silver nanoparticles are commonly studied and used in plasmonics as their resonances are in the visible range. Both these elements are therefore suitable for use in exploratory time-resolved studies. Gold has the advantage of not oxidizing, which otherwise could effect the plasmon in an unknown way. Hence, gold was chosen as the metal for the plasmonic particles produced by FIB milling. FIB milling was applied to a metal film on a dielectric substrate to produce plasmonic metal nanostructures. Sapphire was used as the substrate as it has a high heat conductivity, and thus protects the nanostructure from thermal damage during laser illumination.

As gold films do not adhere well to some substrates, a thin metal layer is often applied between the substrate and the film in nanostructure fabrication. This was done by, for example, by Kim *et al.* [35], who evaporated a 5 nm layer of chromium onto their substrate. In this work it was investigated whether a 5 nm layer of Ni could be used while still obtaining successful milling results.

Figure 2.15 presents two cases: structures, in this with a bowtie geometry, milled with (a) and without the Ni adhesion layer (b). In Fig. 2.15a, the number of passes of the ion beam increases from left to right. When the number of passes was too low (the left-most structure), the milled area around the structures was not cleared. Performing more passes with the ion beam lead to a milled area that was better cleared but at the expense of the structure itself. When the milled area around the structure was entirely clear (the structure to the right), the structure had lost its initial triangular shape. Figure 2.15b shows the case without adhesion layer, where it can be seen that the milled area around the structures is clear, without compromising the structure shape of the structure. The same number of passes was used for the three bowtie structures. Although there were other differences than in the use of an adhesion layer between case a) and case b), the difference between use and non-use was seen many times in this work. The interpretation of these observations is that the adhesion layer of 5 nm Ni is resistant to FIB milling, thus withstanding removal, while the gold is removed more. Adhesion layers of other metals, *e.g.* chromium have also been observed to have an increased resistance to FIB milling [77]. Apart from introducing difficulties during FIB milling, the adhesion layer was not found to be necessary to keep gold attached to the substrate.

During the optimization of the FIB procedure, it is important to be able to identify the plasmonic structure and the substrate in SEM images. The contrast between gold and sapphire is very clear, as can be seen in Fig. 2.15b, where the gold is much brighter than the sapphire regions.

2.5.4 Sample preparation

The PEEM sample holder can only accomodate samples up to 11 mm in size. Cutting a sapphire wafer into such small pieces is quite difficult, and generates many small

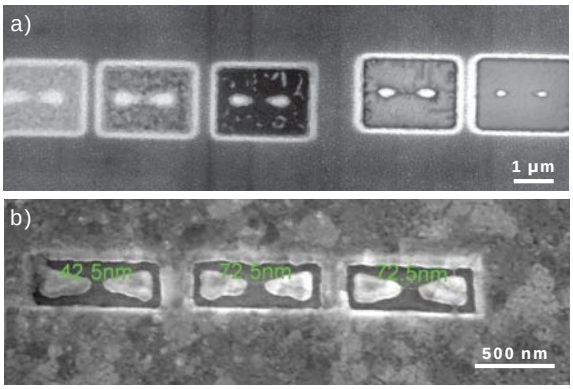

Figure 2.15: SEM images of the effects of an adhesion layer on a sapphire substrate. a) Milled structures in gold with a Ni adhesion layer. b) Milled structures in gold without the adhesion layer.

particles. These small particles may be invisible during SEM inspection but may lead to serious distortion of the PEEM images. (This will be further discussed in Chapter 3). A routine for cleaning the sample was therefore developed. The wafer was first cut into small pieces (∼6 mm×6 mm) using a diamond pen. Each piece was blown with nitrogen gas. The pieces were placed in a beaker containing acetone, which was placed in an ultrasonic bath for at least 2 minutes. The pieces were then rinsed in isopropanol and blown dry with nitrogen. Inspection in an optical microscope using the dark-field mode revealed which pieces that were most clean, and those were then used for nanostructure fabrication.

The gold film is formed using an evaporator (called AVAC). In the evaporation process, a small piece of gold is placed in a holder. The holder is then heated by current passing through it, in turn heating the gold piece, which causes the evaporation.

Finding the designed nanostructures on the ∼6 mm×6 mm-sized sample with PEEM requires structures much larger than the actual nanostructures that are easily found and point towards the nanostructures. Very large structures can easily be made using the FIB technique. Several arrays of nanostructures (3-8) were created on each sample. The location of each array was indicated by two large arrows and numbers. Figure 2.16 shows a SEM image of two such arrays with indicators, together with the corresponding bitmap images used. Table 2.1, gives the parameters used for the arrows and one of the numbers (2). The number of pixels is the number of activated pixels (blue), and the area is the milled area. From these, the dose was calculated, according to Eq. 2.7.

2.5.5 Fabrication

In order to make use of the high resolution possible with FIB, the ion beam must first be focused into a small spot. The most natural procedure for this is to use FIB in the imaging mode at high magnification and attempt to obtain as sharp an image as possible. As imaging with the ion beam also causes some sputtering, the imaged part of the sample rapidly changes. Therefore, focusing the ion beam is non-trivial. It was, however, found that the beam focus could be varied slightly faster than the

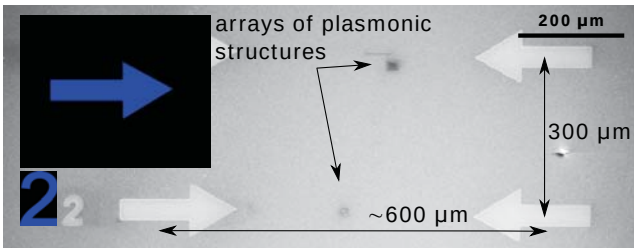

Figure 2.16: A SEM image of arrows and a number used to indicate the locations of the plasmonic arrays. The images used for patterning are also shown.

Table 2.1: Parameters used during the fabrication of an arrow and the number 2. The dose is calculated using Eq. 2.7.

Feature	Image size/px	Number of pixels $\cdot 10^3$	Dwell time $/\mu s$	Number of passes	Area $/\mu m^2$	Current /nA	Dose $\cdot 10^{20}$ /ions /cm^2
Arrow	640×512	30336	50	30	9073	20	3.1
Number 2	82×122	4448	1	4558	810	20	15.6

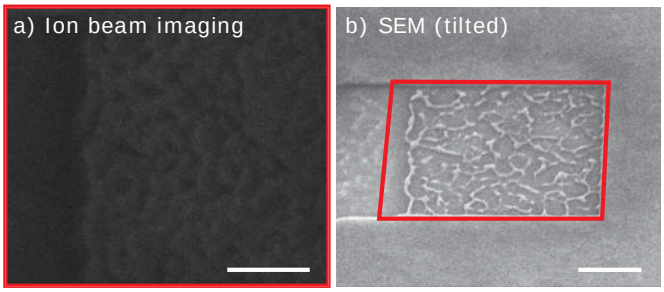

Figure 2.17: Part of a gold film imaged by two sources: a) the ion beam and b) SEM imaging (electrons). The scale bar in both figures corresponds to 500 nm.

rate of induced change in the film, so a well-focused beam could be achieved. Note that the focusing conditions vary with current. When ion beam focus is critical, as in the case of milling small plasmonic structures, focusing should be done using the same current as the milling current (in this work, 1 pA). Figure 2.17 shows part of a gold film, imaged with the ion beam (a) and the electron beam (b). In (a), the structure can vaguely be seen in the gold film, obtained after 10–30 s of ion beam scanning. The signal to noise ratio is rather low due to the low current. This structure changes rapidly during ion beam imaging but the ion beam can be focused to obtain as clear a structure as possible. Figure 2.17b shows more clearly the impact of the ion beam in the exposed area after some scanning. Residues of gold can be observed. Scanning the ion beam for a longer time would lead to more efficient removal of the residual gold.

Once the beam has been correctly focused, the scanning parameters that provide

well-defined plasmonic nanostructures must be determined. The current was set to the lowest possible for this instrument (1 pA), so the best dwell time and number of passes had to be determined. The procedure employed was to choose the shortest dwell-time and optimize the number of passes. The area around the desired structure becomes cleaner with increasing number of passes, but the number should not be so high that the structure of interest shrinks. As the smallest features that can be milled with FIB have been reported to be about ∼10 nm [72], control below this scale is not expected. One factor limiting the resolution in polycrystalline films, is ion channeling, described above, where the ion penetration depth differs for different crystal orientations. As the gold film consists of grains of varying crystal orientation this will lead to certain irregularities in the structures produced. The fact that the evaporated gold film is polycrystalline can be seen, for example, in Fig. 2.15b, where small islands are visible in the gold, seen as variations in image brightness.

After milling the pattern, it is inspected with the SEM part of the instrument. After obtaining a high-resolution image (high magnification and slow scanning) the scanned area usually becomes darker. This is due to hydrocarbons present in the chamber, and adsorbed onto surfaces exposed to energetic radiation. The effect of this kind of contamination was observed in PEEM images using the mercury lamp as an overall reduction in the signal from such regions.

Chapter 3

IR-IR experiments

Two experiments were performed on plasmonic structures using PEEM with two 6 fs IR pulses. In both experiments autocorrelations of the few-cycle near-field dynamics induced in the structures were measured. Results from the two experiments were compared to finite-difference time-domain (FDTD) simulations.

The first experiment (Paper VI) probed the near-field dynamics in gold bowtie antennas fabricated with FIB. In the production of such antennas, there will generally be some randomness in structure due to the fabrication process itself. This is due to the ion channeling effect, leading to different milling efficiencies over the varying crystal orientations in the gold film, see Section 2.5. It is interesting to study the effect of these variations on the near-field dynamics (See Section 1.5) and compare them to the effect of something more controllable, such as the overall size of the antenna. In the second experiment (Paper V), the few-cycle near-field dynamics at the two ends of a rice-grain-shaped *single* silver nanoparticle supporting several plasmon modes [78] was studied.

As the bowtie antennas were produced in-house, their fabrication and optimization are described in detail. The general aspects of nanostructure fabrication with FIB were discussed in Section 2.5, so here the emphasis is placed on the fabrication aspects specific for the bowtie antennas The setup used for the autocorrelation experiments is then described. Finally, the results obtained are presented.

3.1 Nanostructure optimization

Bowtie antennas of different sizes were produced, but before that, efforts were devoted to optimize the fabrication of antennas of one size. The optimal antenna dimensions for maximal field enhancement (a factor of 100) with 10 fs-pulses centered at 800 nm have been calculated by Kim *et al.* [35]. Note that the suggested gap size of 20 nm is close to the resolution limit of FIB. Our antennas were fabricated with a similar design, shown in Fig. 3.1, by evaporating a 25 nm layer of gold onto a sapphire substrate and using the FIB technique.

The bowtie structures must be well separated from the surrounding metal film. The most natural procedure for this would appear to be to replace the bitmap image

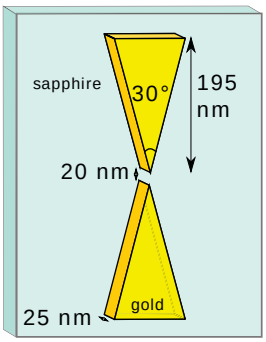

Figure 3.1: The antennae design parameters used in the fabrication process.

of the bowtie with an image with a larger milling area around the bowtie. However, better results were obtained when ion beam scanning was performed in two steps. First a frame, 340 nm×800 nm, was milled. Then, the actual bowtie was fabricated inside the frame. These patterns are shown below. Multiple antennas were then produced in arrays.

Bowtie antennas were produced in two rounds and imaged with PEEM after each. In the first round of production some important factors regarding the fabrication were now known, or easily implemented. These factors were, also mentioned in Sections 1.4 and 2.5, that an ion beam current of 1 pa was necessary for high-resolution milling, that adhesion layers could be resistant to milling and that a cleaning routine was necessary to remove unwanted particles.

PEEM images of bowties produced in the first round were recorded using the mercury lamp and IR pulses. Overlaying these images gives an indication of the location of the field enhancement produced by the structures. Figure 3.2 shows an image in which PEEM images obtained with the mercury lamp and IR pulses are overlaid. The green image was obtained by the mercury lamp and thus shows topography and work function contrast. Each rectangle is a milled region with a bowtie in the center. The red overlaid image was obtained using the IR pulses as an excitation. Spots of high field enhancement can be seen on many of the bowties. However, these spots are not located at the bowtie gaps, where the highest field enhancement is expected. This is probably due to an incomplete removal of metal surrounding the bowtie structures, caused by the use of an adhesion layer. The gaps between the bowtie tips were ∼30–50 nm in this batch of bowties, which was sub-optimal for a large field enhancement. This could explain the limited signal from the gap regions. A large undesired structure producing a high PEEM signal can also be seen close to the center of the array.

In the second round of fabrication, improvements were made to the bowtie samples. These improvements resulted in an area around the structure that was better cleared from metal, a cleaner sample and in a smaller bowtie gap. The milled area around the structure became better cleared from metal residuals when the adhesion layer was removed. The cleaning routine as described in Section 2.5 was developed. The most critical and challenging task in bowtie fabrication was to achieve a gap between the prisms of about 20 nm, which is critical for high field enhancement. Removing the adhesion layer and reducing the current from 10 pA to 1 pA reduced the gap size to ∼0–40 nm. In this process, both the dwell time and the number of passes, and thus

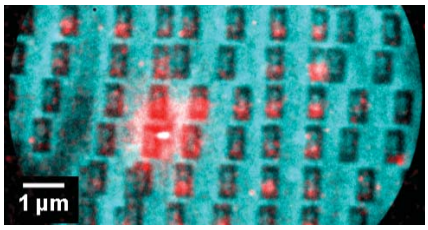

Figure 3.2: Two PEEM images, obtained with the mercury lamp (green) and the IR pulses (red).

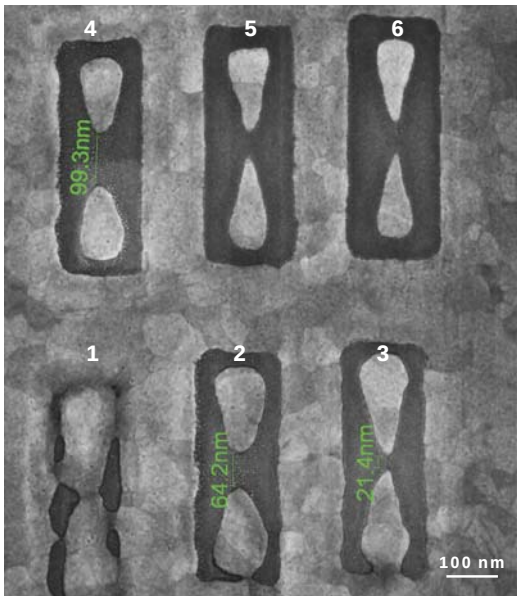

Figure 3.3: A SEM image of bowties made with different charge doses. The dose increases from bowtie 1 to bowtie 6. These bowties were fabricated using an ion current of 10 pA.

the dose, were varied, to find the optimal values. Figure 3.3 illustrates how the bowtie is affected by varying the dose. At too low a dose, as for the bowtie 1 in the figure, the bowtie appears blurred and poorly defined. As the dose is increased (from 1 to 3) it becomes more bowtie-shaped, and even more so when the dose is increased further (from 4 to 6). If the dose is too high (not shown), the triangular shape of the prisms is lost, and two small round shapes remain. During the experiments to find the best dose, the dwell time was kept small, and the number of passes was varied until the desired result was obtained. The optimal parameters are listed below. Figure 3.4 shows some of the resulting bowtie antennas after the second fabrication round and the two bitmap patterns used to make the frame and the actual bowtie.

PEEM images of the bowties fabricated in the second round showed that the structures had improved significantly. Figure 3.5 shows a PEEM image of (larger) antennas using both the mercury lamp and the IR laser, polarized as shown, for excitation. Six antennas are visible. Starting with the antennas on the right, an intense

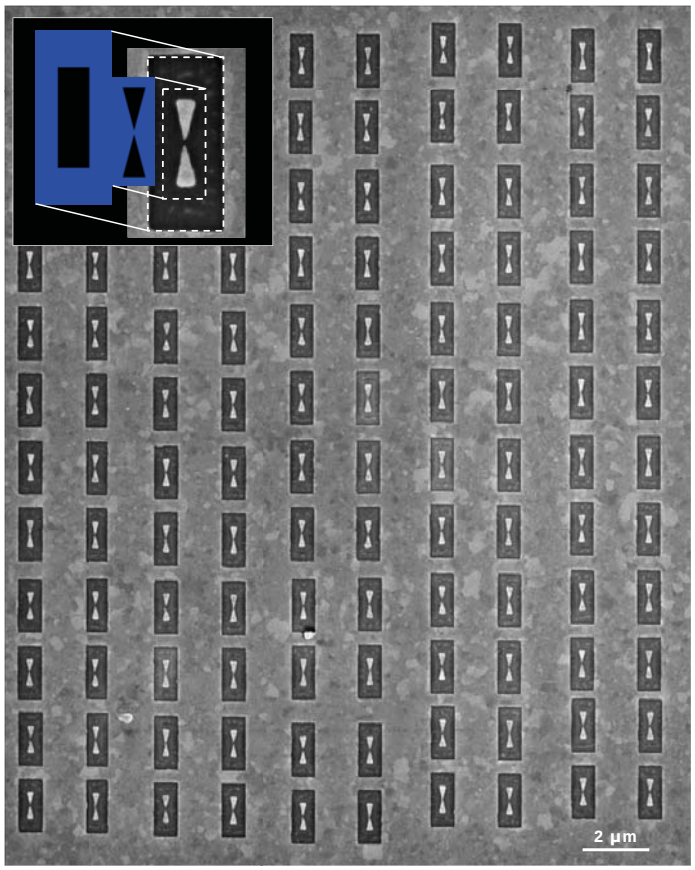

Figure 3.4: The bitmap patterns used, and an example of a fabricated bowtie structure and a complete array (SEM image).

photoemission signal is observed in the gap region of each antenna, and only there, indicating high field enhancement in the gap. A photoemission spot not originating from the gap of an antenna can be seen on the lower left antenna, however, its off-matrix location means that it will not be mistaken as a signal from an antenna.

In order to investigate the influence of the exact shape of the antennas on the induced near-field dynamics, the effects of minor shape variations can be compared to the effect of some other parameter. A natural parameter for comparison is the overall bowtie size. Bowties of distinctively different sizes were therefore produced. This was done by scaling the lateral dimensions discussed above with the scaling factors, s, where $s = 0.5, 0.75, 1, 1.25$ and 1.5, as illustrated in Fig. 3.6a-b. Arrays of 24 antennas of each size were produced, giving a total array size of 120 antennas. The distance between two adjacent antennas was 2 µm. The FIB parameters used for antennas and frames of different sizes are given in Table 3.1.

The fabricated antennas had slightly rounded corners. The actual gap sizes also varied. Limited reproducibility of small gaps in nanoantennas has also been reported by [77]. The original ($s = 1$) antennas were used to quantify the variations. Af-

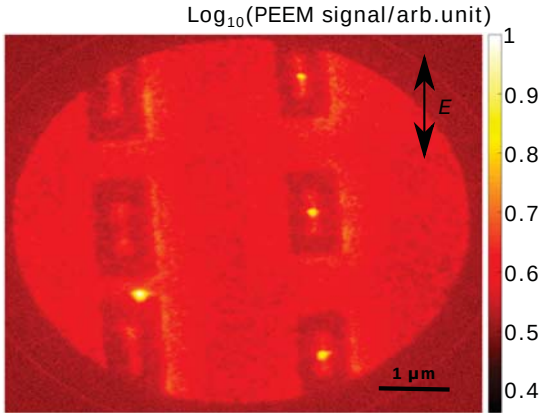

Figure 3.5: A PEEM image of bowties using the mercury lamp and the IR pulses as excitations. Note that these bowties are larger than the dimensions discussed so far.

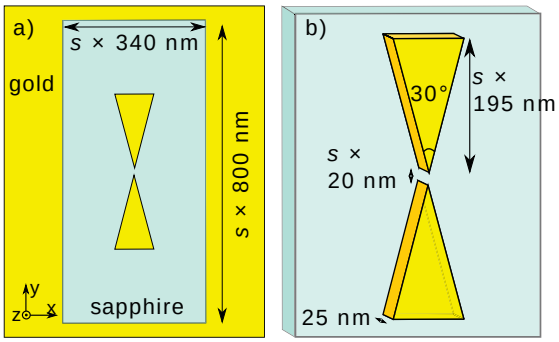

Figure 3.6: Design parameters used to scale the bowtie antennas: a) the dimensions of the milled areas around the bowtie, and b) the bowtie dimensions.

ter discarding the obviously distorted structures and bowties with clearly connected prisms, 2×21 prisms remained. The length of each prism, defined as the height of the triangle [the dimension having the length 195 nm in Fig. 3.1], was obtained from SEM images. The average prism length was found to be 189 nm, *i.e.* slightly smaller than the intended dimension, and the standard deviation was 14 nm.

The other IR–IR experiment used nanorice particles having lengths of 320–600 nm and a diameter of ∼100 nm. They were lying on a tin oxide substrate. These particles were chosen due to their almost spheroidal (and thus simple) geometry, their smooth surfaces and their lack of crystal grain boundaries. The fabrication of the silver nanorice structures has been described elsewhere [79, 80].

3.2 Experimental setup

The main components of the IR–IR setup are an oscillator producing 6 fs laser pulses, an interferometer and the PEEM instrument. The PEEM instrument is placed in a vacuum chamber (10^{-9} mbar), while the rest of the setup is in air. The setup is

Table 3.1: The FIB parameters used to fabricate bowties of different sizes and corresponding frames.

Feature	Image size/px	Number of pixels $\cdot 10^3$	Dwell time /µs	Number of passes	Area /µm^2	Current /pA	Dose $\cdot 10^{18}$ /ions /cm^2
Bowtie × 0.5	927×359	265	0.1	18	0.0193	1	1.5439
Frame × 0.5	817×356	223	1	8	0.0521	1	2.1386
Bowtie × 0.75	927×359	265	0.1	53	0.0434	1	2.0204
Frame × 0.75	817×356	223	1	29	0.1173	1	3.4456
Bowtie × 1	927×359	265	0.1	90	0.0772	1	1.9299
Frame × 1	817×356	223	1	38	0.2085	1	2.5396
Bowtie × 1.25	927×359	265	0.1	160	0.1207	1	2.1957
Frame × 1.25	817×356	223	1	82	0.3259	1	3.5073
Bowtie × 1.5	927×359	265	0.1	204	0.1738	1	1.9442
Frame × 1.5	817×356	223	1	204	0.4692	1	3.6535

illustrated in Fig. 3.7a. The light pulses produced by the oscillator (spectrum shown as spectral power density as a function of wavelength) are stretched by the double chirped mirrors (DCM) in order to compensate for dispersion resulting from the glass in the setup. The dispersion can be finely tuned with the glass wedges. The time delay between the two pulses is achieved by the dispersion-balanced interferometer, where the position of one mirror is on a movable stage. A flip mirror allows the pulses to be characterized using the d-scan technique [81]. A half-wave plate and a polarizer (Pol) were used for sample and setup characterization.

The polarization of the light could be changed from s- to p-polarized (see Fig. 3.7b). The s-polarized light is fully polarized along the sample plane, whereas the p-polarized light has an electric field component in both the sample plane and along the sample normal. For the bowtie sample, the field enhancement was enough to produce high photoemission using s-polarization. The antennas were then oriented so that the light polarization was parallel to the long, inter-particle, antenna axis, (see also Fig. 3.5). In this configuration, the excitation of even modes is minimized. For the nanorice sample, we were interested to excite both even and odd modes. We thus used p-polarized light and looked at nanorice particles mainly oriented along the polarization component in the sample plane. This way we could induce retardation effects and thereby excite even modes.

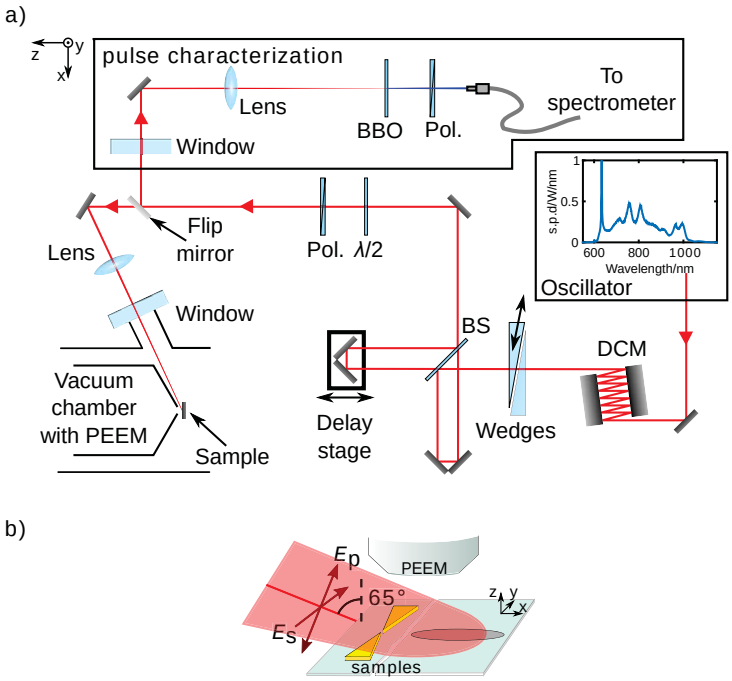

Figure 3.7: a) A schematic of the experimental setup used in the IR–IR experiments, including a spectrum of the oscillator output shown as spectral power density as a function of wavelength. b) The illumination configuration showing the two types of polarization used and the orientation of the two types of nanosystems.

3.3 Near-field autocorrelations

3.3.1 Bowtie nanoantennas

Before the actual near-field autocorrelations were measured, the photoemission process and its dependence on light polarization were investigated. In Section 2.2, it was seen that the photoemission yield is related to the incident light intensity by $Y = a \cdot I^n$, where n is the number of photons required for photoemission. A study of the photoemission dependence on laser power of an array of bowtie antennas was discussed in the same section. It was found that $n = 3.4$, consistent with 3–4 photons being required to overcome the gold work function. The dependence of the photoemission on the polarization of the incident light was then characterized. It was found that the bowties behaved as expected, showing maximum PEEM intensity when the light was polarized along the long, inter-particle, antenna axis (Paper VI). Both the observed photoemission dependence on light polarization and the photoemission dependence on power are thus consistent with previous findings [30, 76, 82].

Simulations were also performed, which revealed that several plasmon modes are supported by each antenna size. The modes become red-shifted as the size increases (Paper VI). At least two resonances were within the spectral range of the laser for bowties of all sizes.

To investigate the near-field dynamics of the bowtie antennas, interferometric near-

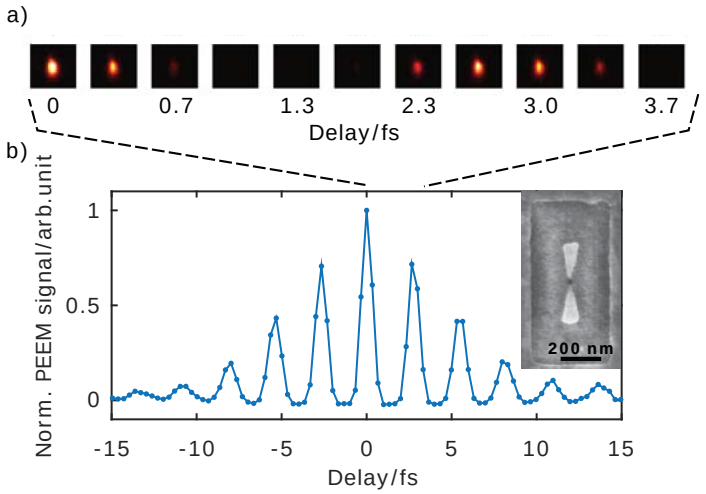

Figure 3.8: A near-field autocorrelation trace of an $s = 1$-antenna. a) The imaged photoemission spot for a small range of delays. b) The integrated signal over the spot for a large range of delays.

field autocorrelations were measured by varying the delay between two identical laser pulses. Figure 3.8a shows first the photoemission signal from one $s = 1$-antenna as a function of the time delay between the pulses. A strong signal can be observed at the region of overlap between the two pulses, at delay = 0. This is expected as the two pulses act together to confine the charges in the tips. In other words, the near-fields induced by the two pulses are completely in phase. The photoemission signal then becomes very low at about 1.3 fs, when the two pulses are opposite in phase. At a delay of about 2.6 fs we again observe a peak in photoemission. The two pulses are now one optical cycle out of phase, so their confinement is less than at zero overlap, but more than in the opposite-phase case. To observe the oscillations more clearly, and study the complete delay scan, the signal was integrated over the photoemission spot, and the integrated value given as a function of delay in Figure 3.8b. A trace that is symmetrical around the zero delay is observed. (A SEM image of the antenna is presented in the inset in b).)

Illuminating the array with differently sized antennas (partly shown in Fig. 3.9a) with the laser, gives the PEEM image shown in Fig. 3.9b. Field enhancement is seen to occur for bowties of all sizes. However, there are large variations in signal between antennas of the same size. This is in accordance with previous findings by others [30, 76, 83, 84]. The causes of these variations include minor shape differences (*e.g.* variations in gap size), differences in grain structure and different surface modifications on the molecular level, all of which can affect the field and/or photoemission process [30, 76, 83, 84]. Slight differences in field strength are further amplified by the nonlinearity of the photoemission signal. Only antennas with a signal above the noise level were considered in the dynamics studies.

To investigate the near-field dynamics of the antennas, interferometric near-field autocorrelations were measured by varying the delay between two identical pulses. Examples of autocorrelation traces from three antennas with scaling factors of $s = 0.5$,

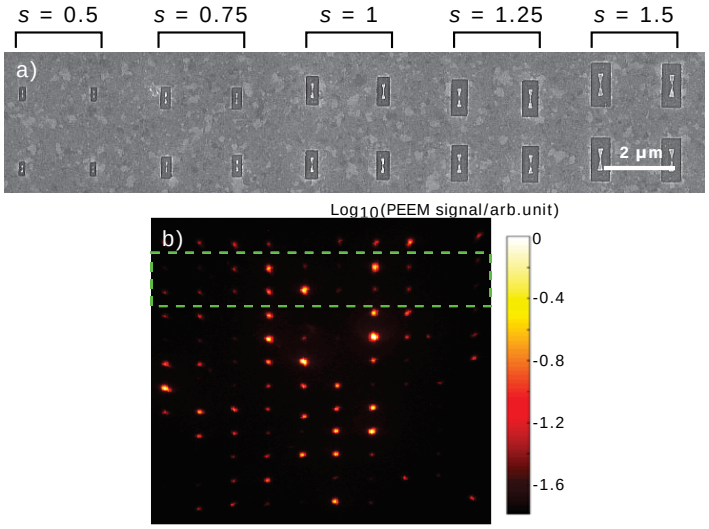

Figure 3.9: An array with differently sized bowties. a) A SEM image of part of the array. The nominal size (scaling factors) of the antennas are indicated above the image. b) A PEEM image of the array, where the part shown in a) is indicated by the green dashed line.

$s = 1$ and $s = 1.5$ are shown in Fig. 3.10a, together with corresponding SEM images. It can be seen that the traces become increasingly more out of phase with increasing delay. One important point is that the antennas were exposed to the laser pulses simultaneously. Therefore, no differences in autocorrelation traces can come from a difference in excitation, but must reflect different near-field dynamics of the antennas.

As the spacing between the fringes in a near-field autocorrelation trace relates to the oscillation frequency of the near field, as discussed in Paper V, the positions of the third and fourth peaks (defined in Fig. 3.10a), with the zero delay peak defined as peak zero, were extracted for all antennas, Figs. 3.10b-c. A slight increase in peak position can be seen with increasing size. This suggests a lower oscillation frequency of the enhanced near field in larger antennas. While such an observation is in accordance with the observed red shift of the plasmon resonances discussed previously, the expected multi-mode character of the antennas should lead to a more complicated behavior than a simple red shift of the oscillation frequency as a function of size. We therefore took the positions of the third and fourth peak as simple indicators of general differences in the near-field dynamics, and used these to compare the effect of antenna size versus detailed shape.

We note a rather large spread in peak position within each size. When the size of the antennas was increased from $s = 0.5$ to $s = 1.5$, the average positions of the third and fourth peaks were shifted by 0.5 fs and 1 fs, respectively. This can be compared to the variation in the peak positions for antennas with the same size by calculating the standard deviation of the peak position within one size group. The standard deviations of the peak positions are 0.1–0.3 fs for the third peak and 0.1–0.7 fs for the fourth peak; the higher values corresponding to the largest bowties. The variations in the peak positions within a size group are thus of the same order as the variations resulting from a change in the antenna dimensions of a factor 3 (between the $s = 0.5$

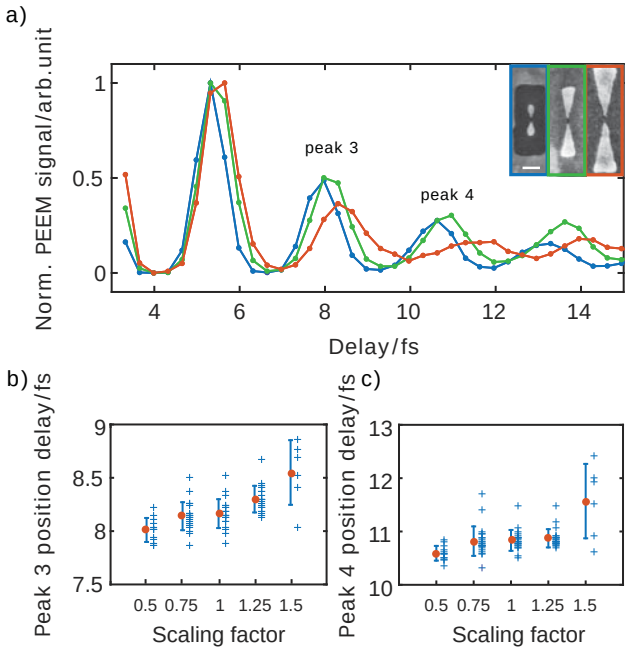

Figure 3.10: a) Near-field autocorrelation results for three differently sized antennas with $s = 0.5$, $s = 1$ and $s = 1.5$. The scale bar in the SEM image inset corresponds to 100 nm. b) and c) The extracted positions of peaks 3 and 4 (indicated in a)), for all the antennas considered, with the mean for each size (brown dot), and error bars showing two standard deviations. The data points have been shifted slightly to the right for clarity.

and $s = 1.5$ antennas).

There are several possible explanations for the large differences in near-field dynamics of antennas with the same overall size. We investigated whether the variation in peak position for a given size depended on simple variations in the bowtie geometry, such as gap and prism length, but no such dependence was found. We therefore used the exact shape of many antennas determined by SEM in FDTD simulations to determine whether the observations could be explained solely by slight variations in the shape of the antennas. Figure 3.11a shows SEM images of three example $s = 1$-antennas, and 3.11b, their extracted lateral shape, which were used the simulations. These shape variations are rather typical for the produced structures.

The simulations confirmed the effect of minor geometrical variations on the near-field dynamics. The calculated z-component of the near-fields for each of the antennas are presented in Fig. 3.12a. Significant differences in the near-field dynamics, despite the same overall size, can be observed. Figure 3.12b next shows the calculated autocorrelation traces of these fields. Clear differences in the traces are observed, reflecting the different field dynamics.

3.3.2 Nanorice

The dynamics of the near fields induced at the two ends of rice-shaped nanostructures was studied. The results obtained for two of the nanoparticles are used to represent

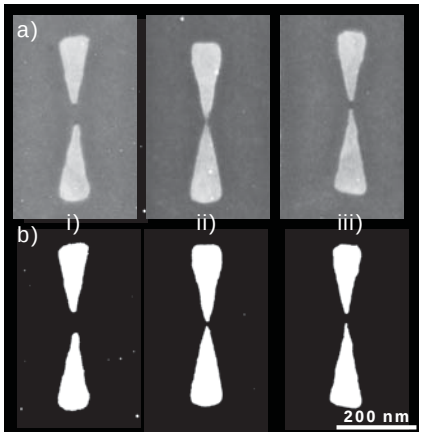

Figure 3.11: Three of the $s = 1$ bowties used in the simulations: a) SEM images and b) extracted lateral shapes used in the simulations.

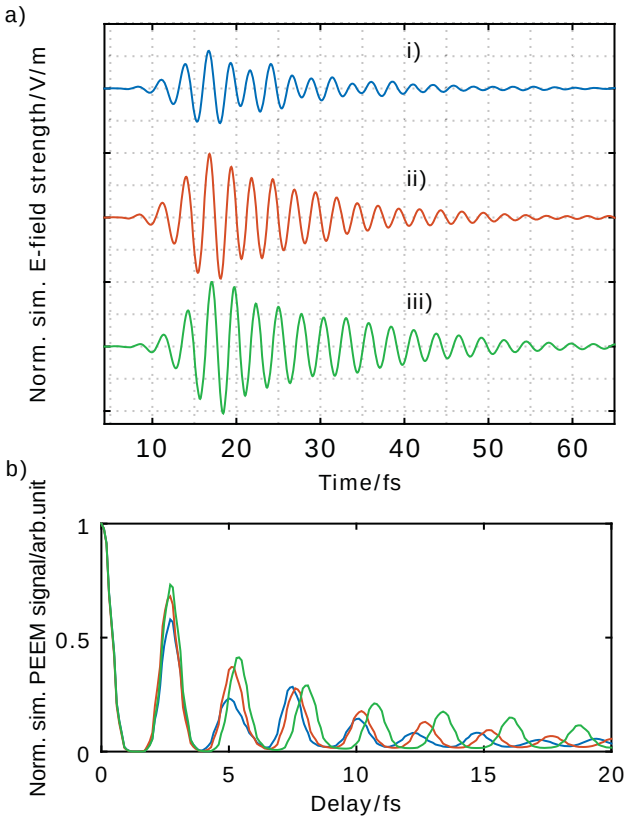

Figure 3.12: a) Simulated z-components of the near-fields at a point on one of the tips for the antennas i), ii) and iii) shown in Fig. 3.11. b) The calculated corresponding autocorrelation traces.

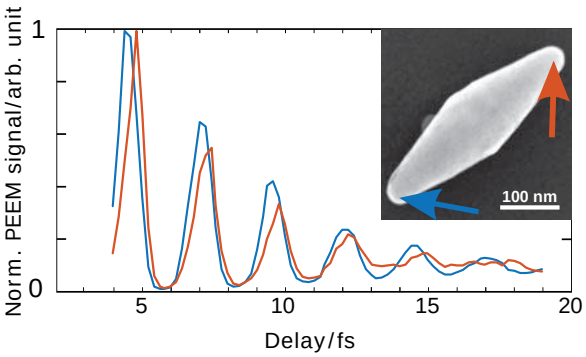

Figure 3.13: Measured near-field autocorrelation traces of the two ends of a 380 nm long nanorice particle. (The inset shows a SEM image of the particle.)

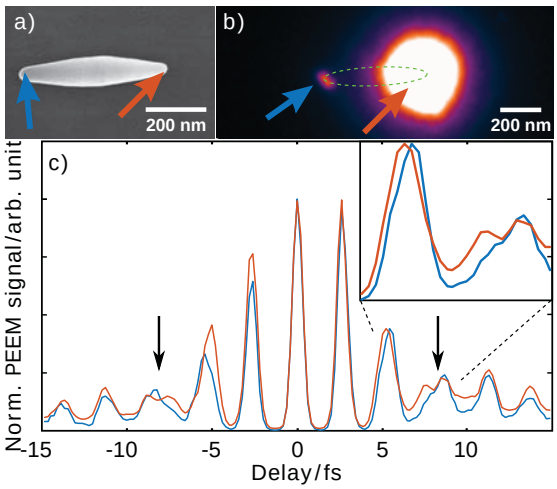

Figure 3.14: The other nanoparticle case. a) shows a SEM image and b) a PEEM image obtained with the IR laser. Two distinct photoemission spots can be observed at the two ends. c) The measured autocorrelation traces at the two ends. A difference in peak positions between the two traces can be observed, as well as complicated double-peak features, indicated by the arrows and enlarged in the inset.

the findings.

For the first nanorice particle, the autocorrelations of the near fields at the two opposite ends appeared shifted with respect to each other (Fig. 3.13), with the peaks of the end furthest from the excitation being shifted towards longer delays. One interpretation of this is plasmon retardation across the nanoparticle, possibly caused by the phase variation of the excitation field across the nanoparticle [82, 85]. This would lead to the near fields at the two ends oscillating out of phase during excitation, and then approaching the same frequency, *i.e.*, the plasmon eigenfrequency. This would result in different instantaneous frequencies, which could explain the observed peak shifts in the autocorrelation traces.

For other particles, the opposite end as compared to the first case, *i.e.*, the end

closest to the excitation, had peaks shifted towards longer delays. Figure 3.14 shows an example of an autocorrelation trace from such a particle. Both sides of the autocorrelation trace contain a complicated double-peak feature. Retardation effects cannot account for these two observations. We believe that in some particles, there is a contribution from both odd and even plasmon modes. We expect both even and odd modes to be present with our excitation geometry (grazing incidence in combination with the large bandwidth of the laser pulse). The near field at one point is thus the coherent superposition of the modes involved. This superposition can exhibit different beating at the two ends due to the different parities of the two modes involved. The instantaneous frequency of one end may then be higher, explaining the observation that the opposite end exhibited peaks shifter to longer delays. The complex near field resulting from beating will also lead to a complex autocorrelation trace, showing, for example, double peaks. Retardation effects and the presence of odd and even modes can explain all the experimentally observed local differences in the near-field dynamics for all the particles in our study.

Chapter 4

Towards an IR–XUV experiment

Conclusions could already be drawn about the induced near field in the near-field autocorrelation experiments. Other methods are, however, required for a complete extraction of the induced field. One such method would be to take snapshots with attosecond pulses of the electron density, at different delays. During such IR–XUV experiments, it can be expected that the number of electrons emitted due to the XUV pulse trains will vary depending on the phase of the plasmonic field in the hot spots. Thus, oscillation in electron numbers is expected in the hot spots. In this chapter, steps towards the realization of such experiment are presented. First, some investigations of the usability of the secondary electrons, suitable sample substrates, image resolution and required exposure times (Paper I) are presented. The findings indicated that XUV pulse trains at a higher repetition rate would be better, so was this also investigated (Papers II, IV, VII and VIII). Finally, the improvements in image quality, using XUV pulse trains at higher repetition rate (Paper III), are described.

4.1 A prestudy

In Section 2.4, it was described how attosecond pulse trains generated with the kHz laser system at the Lund high power laser facility have been found to provide sufficient average photon flux for PEEM experiments [17]. The spatial resolution using the mercury lamp was found to be 50 nm and using XUV pulses 200–300 nm. Improvements were then made in the PEEM unit, by limiting mechanical vibrations, adjusting the electron optics, using smaller contrast apertures and using longer exposure times by employing a cooled slow-scan CCD camera. A prestudy was then performed, to gain knowledge about factors of relevance for a future successful IR–XUV experiments. This study is presented in Paper I. In this study, the same PEEM and kHz laser system was used and the sample consisted of silver nanoparticles. The points considered were:

(i) Whether the secondary electrons are emitted fast enough to be used for IR–XUV experiments. This is interesting as these electrons constitute 90 % of the total electron yield (Paper I).

(ii) Which substrate that can provide a high XUV image contrast between the silver nanoparticles and the substrate.

(iii) What the spatial resolution in XUV PEEM images obtained with the upgraded PEEM instrument was.

(iv) Whether the number of electrons emitted from the interaction of the XUV pulse train with the sample was sufficiently high compared to those emitted from the interaction of the IR pulse with the sample in the hot spots.

(v) For the same area and same illumination condition, the PEEM signal will vary from image to image, due to noise. The exposure times required, given the noise level, were estimated. The case studied was a 10% oscillation in the number of imaged electrons released due to the XUV pulse trains.

The last four points were investigated experimentally. The laser pulse used was sent into an interferometer where attosecond XUV pulse trains were generated in a pulsed argon gas cell in one arm. The XUV pulse trains were separated from the collinearly propagating IR pulses by a 200 nm thin aluminum filter and then propagated through a hole in a mirror that recombined the XUV pulse trains with the IR pulses from the second interferometer arm. The XUV and IR pulses propagated collinearly into the PEEM instrument. The XUV light was defocused at the position of the PEEM unit in order to reduce the XUV intensity. The silver nanostructures used consisted of nanowires, near-spherical nanoparticles, nanorice and nanocubes.

The findings regarding the points are described briefly below.

(i) According to Monte Carlo simulations, 80% of the secondary electrons are released within the first femtosecond. The secondary electron emission is thus predicted to be sufficiently fast to be used in IR–XUV measurements.

(ii) Three substrates were used to find the optimum contrast: a 50 nm thick Au film on Si, a 50 nm Cr film on Si and a 150 nm indium tin oxide film on borosilicate glass. Silver nanowires on gold showed better contrast than wires on ITO or Cr, see Fig. 4.1. On gold the wires appeared up to 30% brighter than the substrate. The lower work function of Ag (4.1–4.7 eV [86, 87] compared to that of Au (∼5.3 eV [45]) could explain the contrast.

(iii) For the XUV resolution test we used the same lithographic sample and a 16–84%-criterion instead of the 20–80%-criterion (explained in Fig. 2.10b as used by Mikkelsen *et al.* [17]). A spatial resolution of around only 200 nm was obtained. We also measured the full width at half maximum (FWHM) of a nanowire with 200 nm in diameter on the gold substrate, with an exposure time of 400 s. It was found to be 900 nm, as shown in Fig. 4.2.

Thus, after the technical improvements mentioned above, the resolution using XUV pulses was improved from ∼200–300 nm to ∼200 nm. According to Mikkelsen *et al.* [17], the worse resolution using XUV pulses originates from the large energy spread of the photoelectrons emitted when using XUV radiation. An energy filter or smaller apertures could probably improve the resolution, but the photoelectron flux was not sufficiently high to reduce the number of detected electrons. The results suggest that a higher photoelectron flux, resulting

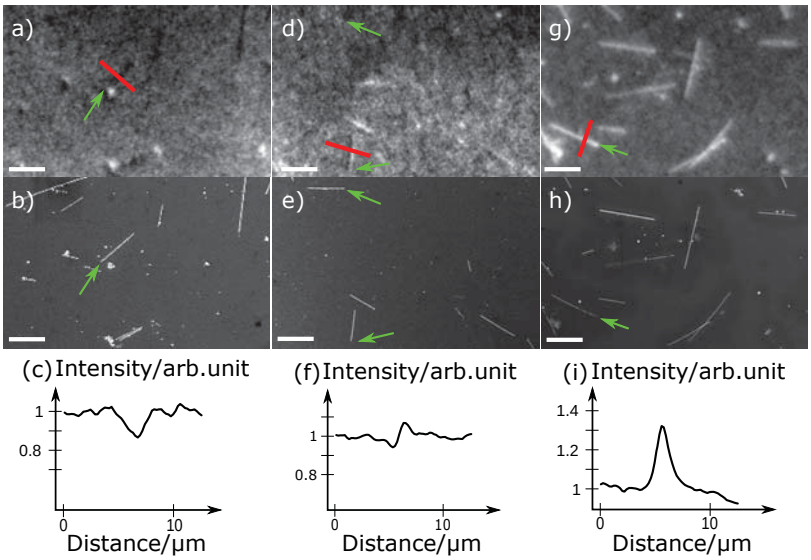

Figure 4.1: XUV PEEM images [a), d) and g)], corresponding SEM images [b), e) and h)] of silver nanowires on indium tin oxide, Cr and Au respectively. All scale bars are 10 µm. c), f) and i) shows the intensity profiles over the regions indicated by red lines in a), d) and g), respectively.

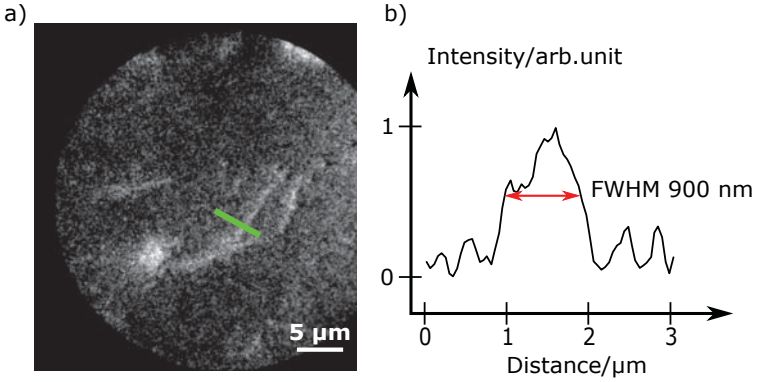

Figure 4.2: a) XUV PEEM image of silver nanowires on gold. b) Intensity profile of the region indicated by green in a). The FWHM of the imaged wire is 900 nm.

from more frequent XUV pulse trains, not more electrons per XUV pulse, could improve the spatial resolution.

(iv) We combined an IR beam with the XUV beam and concluded that, in the hot spots, most of the detected electrons are the result of interactions with the XUV pulse trains (for IR peak intensities of $10^{13} - 10^{14}\mathrm{W/m^{-2}}$). This is important as it must be possible to detect the photoemission signal due to the XUV pulse trains above the constant background.

(v) We measured the PEEM signal values over an area on the substrate without features for different exposure times. The noise level in this area was defined as the ratio between the standard deviation and the mean of the pixel values. A noise level of 0.035 would correspond to a sinusoidal oscillation with 10% peak-to-peak variations compared to the background. This level was obtained with an exposure time of 500 s, when using the kHz system.

This suggested two additional reasons for using a laser system providing a higher photoelectron flux through a higher pulse repetition rate. The first is that the acquisition times should be practical to work with. Secondly, the experiment is less sensitive to fluctuations in the high-power laser system and other instabilities when the measurements are shorter.

To conclude, we found that the secondary electrons excited during PEEM experiment are released on an ultra-short time scale, thus being useful in time-resolved plasmon experiments. Gold was identified as a suitable substrate for silver nanoparticles. The PEEM signal due to the XUV pulse trains was found to be higher than the signal due to the IR in the hot spots and rather long exposure times were estimated to be needed to detect near-field oscillations. Importantly and for three reasons, it is concluded that a higher repetition rate than 1 kHz of the produced XUV pulse trains would be beneficial. 1) The increased number of XUV pulse trains could allow the use of smaller apertures or an energy filter, which could improve the spatial resolution. 2) The exposure times could be shorter and thus more practical to work with. 3) Shorter exposure times would also make the measurement less sensitive to laser fluctuations or other instabilities.

4.2 XUV pulse trains at high repetition rate

From the above, it is clear that PEEM imaging would benefit from a higher photoelectron flux than that possible with the kHz laser system, if the number of photoelectrons per shot is kept small. Achieving HHG at repetition rates higher than 1 kHz is thus of a great interest.

For time-resolved plasmonics in general, user-friendly generation of attosecond pulses could also be interesting, as discussed in Section 4.1. A third point of interest is the generation of a single attosecond pulse per IR pulse instead of a train of pulses, which could be used to scan the full plasmonic field. A single attosecond pulse could potentially be achieved when the number of generating laser cycles is very few, by using various gating techniques [50].

This section describes experiments performed to fulfill these interests. High-order harmonics were generated at a high repetition rate with two laser systems. Both sys-

tems could thus successfully be combined with PEEM. However, the two laser systems differ considerably in most other aspects, making them suitable for very different applications. The first system is a compact and user-friendly turnkey system with rather long (170 fs) laser pulses. The other laser system is an OPCPA system, capable of delivering ultrashort pulses of 8 fs duration. The turnkey system is ideal for researchers interested in the use of attosecond pulses with, for example, PEEM, but who have limited experience in the field of attosecond science. The OPCPA system is interesting for PEEM because of its high repetition rate and short pulse duration, ideally suited for production of single attosecond pulses.

We characterized the harmonic emission from the turnkey laser in terms of the repetition rate, pulse energy and photon flux (Paper II). In the tight focusing scheme employed, the short-trajectory contribution was not optimally phase-matched, and was therefore of comparable strength to the long-trajectory contribution. Thus, both made clear contributions to the harmonics. This provided suitable conditions for a study of the ellipticity dependence of the trajectories (Paper VII). The clear contributions of the trajectory contributions also enabled us to fruitfully study how they depended on the chirp of the driving pulse (Paper VIII). The results of this study together with mathematical modeling allowed the dipole phase parameters for the short (α_s) and long (α_l) trajectories to be determined (see Section 2.4).

When generating harmonics with the OPCPA system, a clear dependence on the CEP could be observed (Paper IV). The pulses being both short and having the same CEP, made the observation possible. CEP-dependent effects have been observed previously (see references in Paper IV), but mainly in specific spectral regions, such as the cut-off or the region between consecutive harmonic peaks.

This section first describes the experimental setup of both laser systems and the HHG setup, and then the results.

4.2.1 The laser systems

The turnkey laser system is a commercially available ("Pharos, Light Conversion") Yb:KGW (ytterbium-doped potassium gadolinium tungstate) laser. It is compact, ($640 \times 360 \times 212$ mm), user-friendly and stable in operation (pulse energy, pointing, and pulse duration). The central wavelength of the pulses is 1030 nm. The repetition rate is tunable between 1 kHz and 600 kHz, and the pulse energy can be varied between 0.5 mJ and 10 μJ. At 200 kHz repetition rate the pulse energy is 30 μJ. The chirp of the pulse can be adjusted with a grating compressor/stretcher.

The OPCPA laser system produces CEP-stable, 10 μJ, 8 fs pulses centered at 890 nm at a 200 kHz repetition rate. The system consists of three main components: a broadband Ti:Sapphire oscillator (Venteon, used in the IR–IR experiments, Chapter 3), a pumping laser based on a Yb-doped fiber amplifier, and a two-stage non-collinear OPA. A small part of the spectrum of the 6 fs pulses delivered by the oscillator serves as the seed for the fiber laser, whereas the main part seeds the OPA. The fiber output pulses are frequency doubled to 515 nm, and are then sent to pump the OPA stages, consisting of two beta barium borate crystals. The signal from the oscillator is first stretched to match the pump pulse duration, then amplified and then compressed by chirped mirrors. A detailed description of the laser system can be found in Paper IV. Only 2–3 cycles are included in the FWHM of the 8 fs long IR pulse, which should lead to the generation of very few attosecond pulses.

4.2.2 The HHG setup

The same HHG setup was used with both laser systems. A tight focusing scheme was employed to achieve sufficiently high intensity for HHG. As XUV radiation is absorbed by air, generation takes place in vacuum. The main components of the HHG setup are a vacuum chamber, a lens to focus the laser light, a gas jet and a spectrometer to characterize the harmonics generated, see Fig. 4.3.

The laser light was sent into the chamber and focused onto the gas by the lens. The focal length was 10 cm when used with the turnkey system and 5 cm when used with the OPCPA system. This tight focusing results in a small interaction volume, which must be compensated for by a high density in the generation gas. Argon was mainly used as generation gas with both laser systems. It entered the vacuum chamber through a small nozzle mounted on a 3D-translation stage. A cone with a small pinhole separated the generation part from the detection part, each pumped by a turbo pump. The pinhole allowed for a high (10^{-2} mbar) pressure in the generation part, while at the same time maintaining only 10^{-7} mbar in the detection part. The gas pressure in the setup was limited by the pumping system. A 200 nm thin aluminum filter blocked the IR. The XUV light was diffracted onto a MCP by an XUV grating. The grating was placed on both a rotary stage and a linear stage, where the latter was used to remove the grating from the beam path. The grating diffracted and focused the harmonics in the dispersive plane and reflected them in the perpendicular direction. This allowed investigation of both the spectral content and the divergence properties of the harmonics. The MCP was imaged with a CCD camera. The spectra were calibrated using observed atomic lines or the well-known transmission edges of different metallic filters.

In the experiment with the turnkey laser, the XUV photon flux was measured. This was done by removing the grating from the beam path, and measuring the flux with an XUV camera. For the ellipticity measurements, a quarter-wave plate was inserted before the beam entered the chamber.

When the OPCPA system was used for HHG, a pair of glass wedges was installed in the beam path before the chamber, allowing the amount of glass in the beam to be tuned. The dispersion and CEP could thus be varied.

Typical argon harmonic spectra using the turnkey laser and the OPCPA system are shown in Fig. 4.4a–b, respectively. The harmonics from the turnkey laser are spectrally well-defined. For some harmonic orders, the (less divergent and spectrally more confined) short-trajectory contribution was clearly separated from the (more divergent and spectrally broader) long-trajectory contribution (Fig. 4.4a). The harmonics generated with the OPCPA system are much broader. This is due to the much shorter pulse, resulting in the generation of fewer interfering attosecond pulses. This spectrum was recorded after optimization of the short trajectories (by moving the gas nozzle). When no such optimization was performed, complicated features surrounding the fringes were observed, most likely overlapping long-trajectory contributions.

4.2.3 Characterization of the XUV emission generated with the turnkey laser

By exploiting the tunable repetition rate of the laser, we investigated the repetition rates at which harmonics could be generated in argon. We found that harmonics could

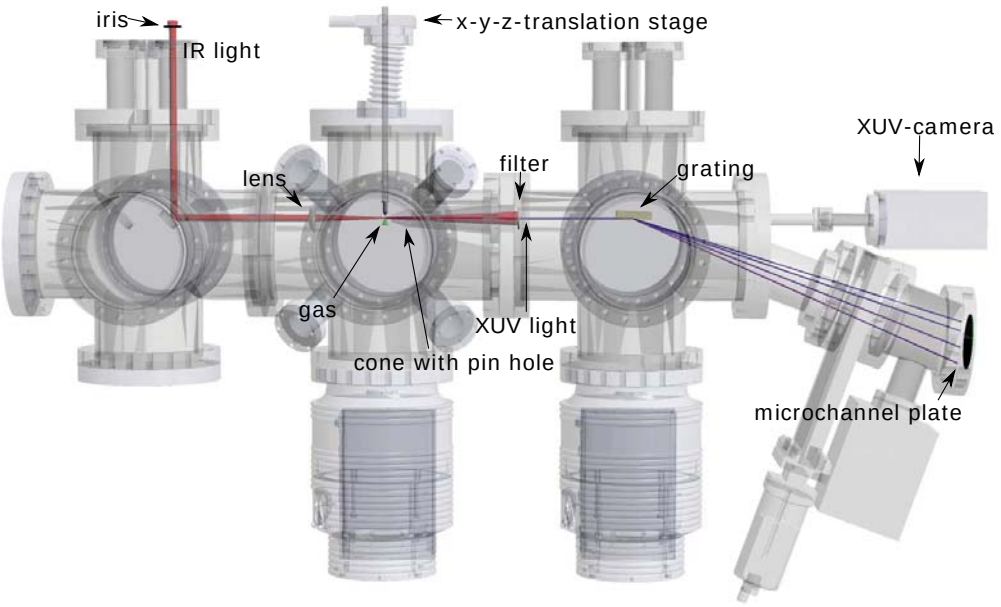

Figure 4.3: The setup used for HHG at 200 kHz repetition rate.

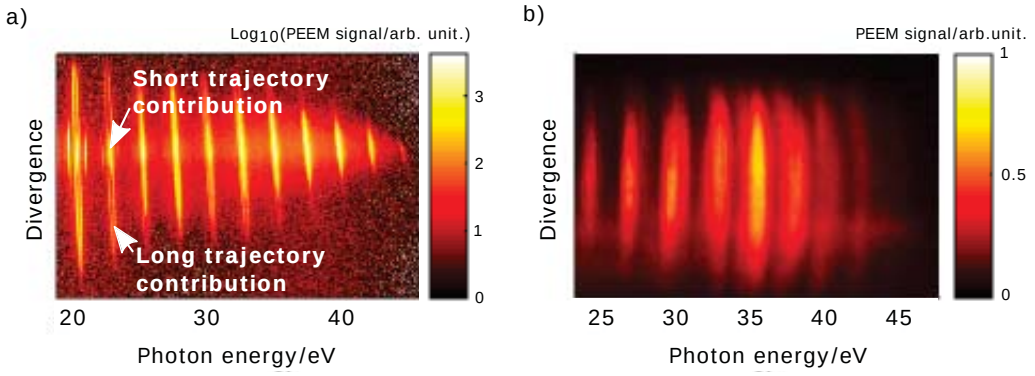

Figure 4.4: HHG spectra. a) Spectrum obtained with the turnkey laser at 20 kHz. b) Spectrum obtained with the OPCPA system at 200 kHz.

Table 4.1: The highest observed harmonic orders and corresponding photon energies generated in argon for different repetition rates and pulse energies using the turnkey laser.

Repetition rate/kHz	Laser pulse energy/μJ	Harmonic order	Photon energy /eV
20	<175	41	49.4
50	<90	35	42.1
100	54	33	39.7
200	30	27	32.5
300	20	21	25.3
400	15	19	22.9

be generated up to 400 kHz, see Table 4.1, which is very interesting for applications with PEEM.

We measured the flux of XUV photons generated in argon at repetition rates of 20 kHz and 100 kHz. At 20 kHz up to $4.2 \cdot 10^{11}$ photons (conversion efficiency $4.9 \cdot 10^{-7}$) were generated per harmonic order, and a total of $21.1 \cdot 10^{11}$ photons (conversion efficiency $27 \cdot 10^{-7}$) for all orders. At 100 kHz up to $4.4 \cdot 10^{10}$ photons (conversion efficiency $3.9 \cdot 10^{-8}$) were obtained per harmonic order, and a total of $29.0 \cdot 10^{10}$ photons (conversion efficiency $24.3 \cdot 10^{-8}$).

In the calculation of these values, the aluminum oxide layer on the filter, the diffraction efficiency of the grating and the quantum efficiency of the XUV camera were considered. We later discovered that the wrong quantum efficiency had been provided by the camera manufacturer, which means that the actual photon flux was lower than reported in Paper II. (The reduction depends on the photon energy.) The fluxes were recalculated, and for photon energies around 20 eV, a factor of a maximum 6 less photons were found than reported in the paper. For photon energies around 50 eV the flux was a factor of 20 less.

The highest possible photon energy was then investigated. We investigated generation of higher harmonic orders for noble gases with a higher ionization potential, specifically neon (see Section 2.4). The highest observed harmonic order was 77, corresponding to 92.7 eV or 13.4 nm. This photon energy was obtained using an IR pulse energy of 170 μJ at 20 kHz.

A high repetition rate, XUV photon flux and photon energy were demonstrated using a turnkey laser. This is relevant for researchers outside the high power laser laboratories interested in for example time-resolved plasmonics.

4.2.4 Ellipticity dependence

By exploiting the clear separation between the long- and short-trajectory contributions to the harmonics obtained with the 170 fs-pulses, we were able to study and compare their ellipticity dependence. Figure 4.5a shows clearly the contributions to each harmonic order, where the innermost spot is associated with mainly the short trajectory and the outer ring with the long trajectory. The area between the inner spot and outer ring is also associated with the long trajectory. In Figure 4.5b, the ellipticity dependence of the contributions to harmonic order 23 is shown. Gaussian

curves were fitted to the respective datasets. The arrows indicate which contribution each curve is associated with. It can be seen that the intensity decreases more rapidly for the long-trajectory contribution than for the short-trajectory contribution as the ellipticity increases. This is due to the fact that electrons following long trajectories spend more time in the continuum, and are thus more affected by the ellipticity of the driving field.

The threshold ellipticity, ϵ_{th} is defined as the ellipticity at which the intensity has fallen by a factor 2 (see Fig. 4.5b). Fig. 4.5c shows the threshold ellipticity for the long and short trajectories as a function of harmonic order. The red curve represents the average of the threshold ellipticities associated with the two long-trajectory contributions, that is, the area between the inner spot and outer ring, and the outer ring. The previously observed behavior, of greater sensitivity to ellipticity for the long-trajectory contribution than the short, for harmonic 23, is now observed for all harmonic orders. The threshold ellipticity of the short-trajectory contribution decreases slowly with increasing harmonic order. This is in agreement with previous studies (see references in Paper VII). It can also be understood within the three-step model. As the short-trajectory electrons spend more time in the continuum for higher harmonic orders, they become more transversally displaced from the ion core than those resulting in lower orders. Thus, the overlap between ion and electron decreases with harmonic order. For the long trajectories, this argument would lead to the opposite result, as the higher harmonics result from electrons spending *less* time in the continuum. However, in Fig. 4.5c a slight decrease in threshold ellipticity can be seen for the long trajectories, similar to the case of the short trajectories.

To help understand the ellipticity dependence of the long-trajectory contribution to the harmonic signal, a model was applied that accounts for the fact that the electrons are tunnel-ionized with different initial velocities dependent on the sub-cycle time of ionization. The model qualitatively reproduces the experimental data in the plateau region. For harmonic orders 17, 21 and 23 there are, however, differences between the data and the results obtained from the model; the long-trajectory contributions exhibiting a higher sensitivity to ellipticity than predicted by the model. See Paper VII for the interpretation.

4.2.5 Chirp dependence

Harmonic spectra were measured as a function of chirp, affecting also the duration and intensity of the driving pulse, using the turnkey laser. The pulse duration was varied between down-chirped pulses (where the frequency decreases with time) of 500 fs to Fourier-limited pulses of 170 fs, to up-chirped pulses (where the frequency increases with time) of 500 fs. We studied the intensity profile of the central part of each harmonic in both the spatial and spectral direction as a function of pulse duration, see Paper VIII. Figure 4.6 shows an example, where the central part, in the spatial direction, of harmonic order 17 is shown as a function of pulse duration.

By applying a mathematical model for HHG based on classical physics, which includes the parameters $\alpha_{s,l}$ (introduced in Equation 2.4), we could simulate the experimental spectra. By optimizing the fit it was possible to determine the values of $\alpha_{s/l}$. The diagrams obtained and the values of $\alpha_{s/l}$ are presented in Paper VIII. If ϕ_l^0-ϕ_s^0 additionally would be measured and a RABBITT measurement performed, a full reconstruction of the harmonic emission, including the phases of the short and

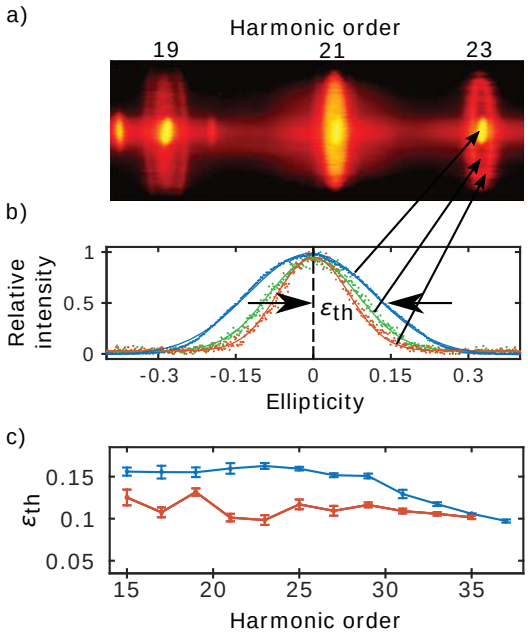

Figure 4.5: a) Three harmonic orders, where the different contributions to each can be seen clearly. b) Intensity dependence of the short- (blue) and long- (red and brown) trajectory contributions of harmonic order 23. c) Threshold ellipticity, ϵ_{th}, defined in b) as a function of harmonic order for the short (blue) and long (red) trajectories.

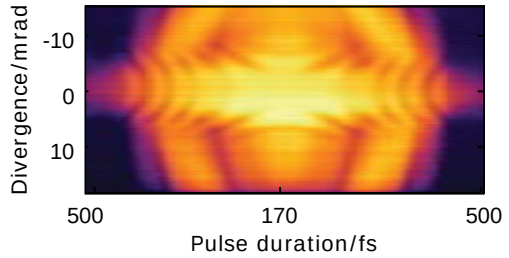

Figure 4.6: The central part, in the spatial direction, of harmonic order 17 as a function of pulse duration.

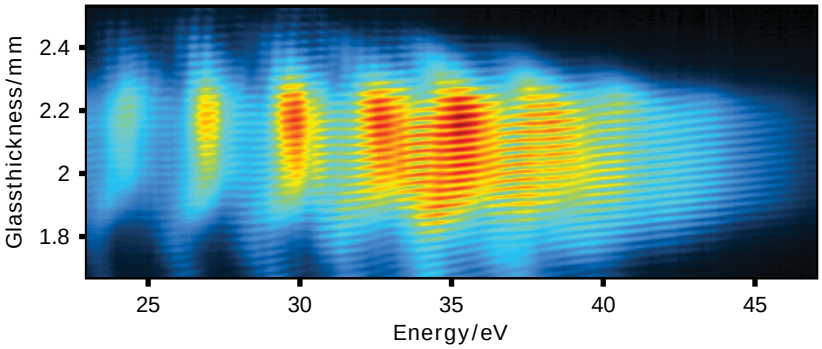

Figure 4.7: An harmonic spectrum as a function of glass thickness in the beam.

long trajectory contribution for each harmonic order, would be possible (see Section 2.4).

4.2.6 CEP dependence

Harmonic spectra, covering 25–45 eV and optimized for the short trajectory contribution, were recorded using the OPCPA system to drive the harmonic generation while varying the thickness of glass inserted (see Fig. 4.7). When the thickness of the inserted glass was too much or too little (top and bottom of the figure), the harmonic signal almost disappeared. This is explained by the pulse becoming too long (and chirped), and not sufficiently intense for harmonic generation. The fringe pattern in the horizontal direction is an effect of the CEP of the IR field: each structure reappears when the CEP has been shifted by 2π. Intense harmonic generation was observed with glass thicknesses between 2.1 and 2.2 mm. In this region, the change of glass thickness is very small so we can neglect the effect of chirp and instead focus on the CEP effect.

We developed a model to interpret the CEP-dependent harmonic spectra. The model was based on interference of three attosecond pulses, since this is the estimated number of pulses in our experiment. The spectral phase of the generated attosecond pulses is affected by a CEP change, through their intensity dependent dipole phase. When summing their spectra, including the phase, we get a result in good agreement with our experimental data, see Paper IV. This indicates that the physics of the observed pattern is contained in the variation of the spectral phase of consecutive pulses, and not only in the number of interfering pulses, for example. As this measurement provides information of the spectral phase of the XUV pulses, it can be a useful part in a reconstruction of the harmonic emission.

4.3 XUV pulse trains on nanostructures at high repetition rate

In Section 4.1 it was shown that HHG at a high repetition rate is needed to obtain high-quality PEEM images of plasmonic fields. High-order harmonics were successfully generated at repetition rates of 20-400 kHz with the turnkey laser, and at 200 kHz with the OPCPA laser system (Sec. 4.2). The next step was to obtain PEEM images using

XUV pulse trains produced at these repetition rates and to confirm the improvement in the image. We used the OPCPA system as this system provides shorter laser pulses. The short pulses result in only three XUV pulses per IR pulse, *i.e.* XUV pulse trains consisting of three pulses. Experiments with this system can thus pave the way for future PEEM experiments using a single XUV pulse per IR pulse.

This section describes the work presented in the book chapter, Paper III. The PEEM image resolution using XUV pulse trains generated at 200 kHz repetition rate as a light source was first investigated. In Section 4 it was shown that the secondary electrons should be emitted very rapidly, and could thus be used in PEEM experiments. However, it is also interesting to be able to observe only the primary electrons. This was thus also investigated.

The increase in the average intensity of XUV photons at 200 kHz repetition rate, compared to that at 1 kHz repetition rate, provided several new possibilities. These are all based on the expected increase in the number of photoelectrons emitted, which would allow some to be discarded by filtering or collimation. One new option was the use of smaller contrast apertures, which would reduce spherical and chromatic aberration. Another option is the use of an energy filter. A high-pass, retardation grid imaging energy filter was installed, allowing only electrons above a chosen energy to pass. With this energy filter in place it was possible, for example, to image both the secondary and primary electrons or only the (higher energy) primary electrons.

Let us compare PEEM measurements using HHG at 1 kHz and 200 kHz. The same Ag silver nanowires, 200 nm in diameter, were imaged in both cases. Figure 4.8 shows PEEM images with various repetition rates and exposure times. The difference in exposure time is an order of magnitude; the much shorter exposure time being needed for the 200 kHz image. In addition to the improvement in exposure time, the spatial resolution is clearly improved. Measuring the PEEM signal across a nanowire in the two cases gives a FWHM of 900 nm with the kHz system and 350 nm with the OPCPA system. Comparing the two FWHM values shows an improvement with a factor 2.6. The reason for the improvement is the higher number of photoelectrons. This makes it possible to use smaller apertures which reduces spherical and chromatic aberrations.

Using XUV pulse trains at a high repetition rate it was possible to obtain sharply focused images of only the primary electrons, as shown in Fig. 4.9. Figure 4.9a shows a PEEM image of a gold/silicon surface obtained using all the electrons, while Fig. 4.9b shows the PEEM image obtained using only the high-energy (primary) electrons. It was possible to image only the primary electrons due to the increased photoelectron intensity, which made alignment of the microscope using the primary electrons possible.

Both the spatial resolution and the exposure time required were improved when using XUV pulse trains at a repetition rate of 200 kHz, compared to 1 kHz. The exposure time was considerably reduced to more realistic values ($\sim$30 s), which also is important in IR–XUV experiments. The energy filter was installed and can be used to decrease chromatic aberration or for successful imaging of only primary photoelectrons.

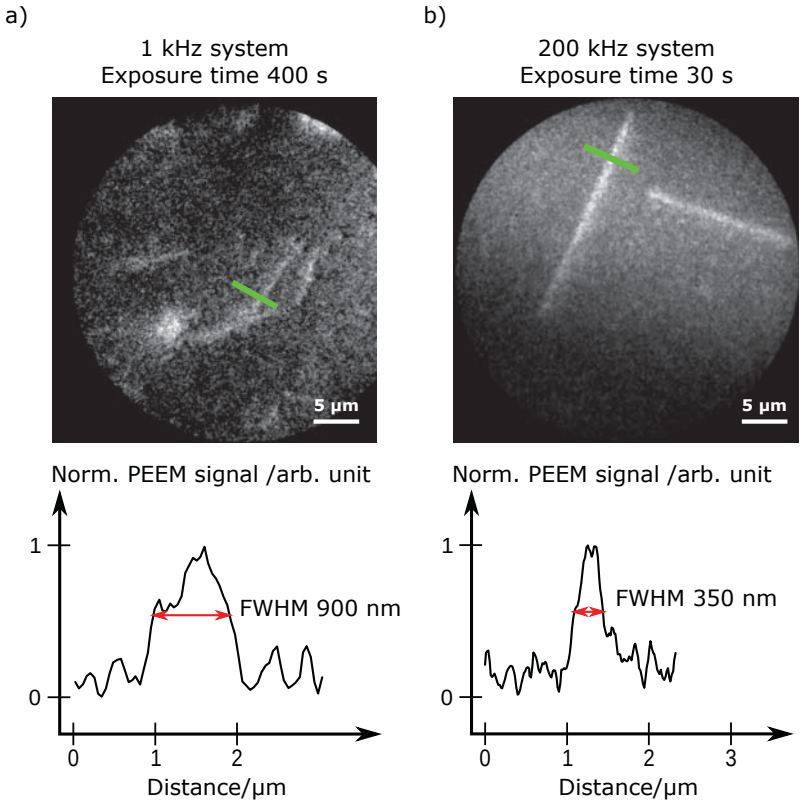

Figure 4.8: The same type of nanowires imaged with PEEM using a) XUV pulses obtained with the kHz laser system and 400 s exposure time, and b) XUV pulses obtained with the OPCPA laser system with a 200 kHz repetition rate and 30 s exposure time.

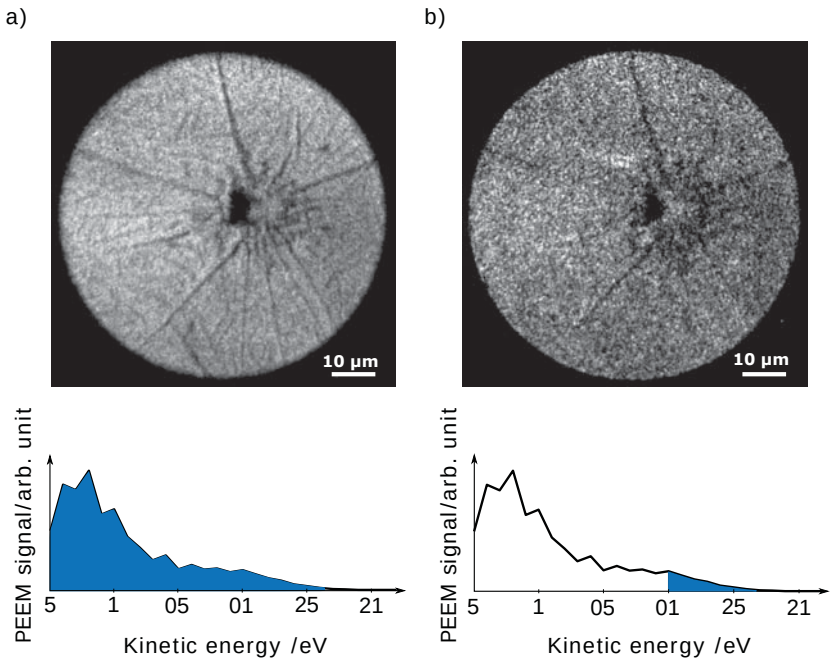

Figure 4.9: PEEM images using: a) only high-energy photoelectrons (primary electrons) and b) electrons of all energies, as shown in the diagrams below.

Chapter 5

Summary and outlook

This thesis describes experiments in which the time-resolved dynamics of plasmons are targeted. We were particularly interested in two topics. The first concerned the effect of the exact shape of the commonly used bowtie antennas on the ultrafast induced plasmon near field. The other topic of interest was the simultaneous study of the near-field dynamics of different parts of a single nanostructure.

These two topics were investigated by performing autocorrelation studies of the near field using PEEM with few-cycle IR pulses. The bowtie experiment involved manufacturing tailored nanostructures. The autocorrelation measurements provided answers to the questions raised. It was found that the exact shape of the nanostructures was critical for the evolution of the few-fs near field. It is of fundamental interest that the variation in peak position, which indicates a variation in the near-field dynamics, for slightly different antennas is comparable to the peak position variation between completely differently sized antennas. This is also important in the fabrication of antennas for applications. The nanorice experiment exploited the high spatial resolution of PEEM. In this particular study, we were able to observe the effects of retardation and the superposition of modes with different parity. This study demonstrated the nanometer- and few-femtosecond-resolved characterization of plasmon-enhanced near fields.

It is also of considerable interest to be able to map the induced field in nanoparticles more directly, either the complete evolution of the field, or a cycle of it. PEEM experiments using attosecond pulses were therefore targeted. Before the start of the work described in this thesis, it had been observed that the attosecond pulse trains generated with the kHz laser system in Lund, provided enough photon flux to be combined with PEEM [17]. This previous study also indicated the benefit of higher repetition rates of the attosecond pulse trains. We performed a further prestudy with the same laser system but with an improved PEEM setup, revealing a number of interesting facts. The secondary electrons excited during PEEM experiments were predicted to be usable in ultrafast experiments. A suitable substrate for experiments using silver nanoparticles was found, and the image resolution using XUV pulse trains was improved due to the PEEM upgrade, but was still limited. Furthermore, the PEEM signal resulting from XUV induced photoemission was found to be higher than the signal resulting from the IR induced photoemission in the hot spots. Moreover,

rather long exposure times were found to be needed to detect the ultrafast plasmon dynamics. It was also concluded that XUV pulses with a higher repetition rate would be advantageous as this would allow the use of an energy filter to reduce chromatic aberration, and would reduce exposure times.

Efforts were then made to implement the generation of XUV pulse trains at high repetition rates. In that process, several interesting aspects of the HHG itself were also studied. One is how the emission from the long trajectory involved in HHG depends on the ellipticity of the driving field. Another is that obtained CEP- and chirp dependences of HHG spectra could pave the way towards full characterization of the harmonic emission. A third aspect is that HHG using a turnkey laser could be of interest for researchers outside the attoscience community, such as those in plasmonics. (During the work described in this thesis, HHG using a turnkey laser was first reported by another group [71]. However, a more detailed investigation on the properties of the XUV light generated was desired.)

High-repetition-rate (∼200 kHz) HHG was implemented with two different laser systems. One of the systems was a turnkey laser. The harmonic emission generated with the help of this system was characterized. The ellipticity dependence of the long-trajectory emission and the chirp dependence of the spectra were also studied. The other laser system was an advanced OPCPA system. (During the course of the work described in this thesis, high-order harmonics were also generated by another group using an OPCPA system [69]). Our OPCPA system allowed for fruitful measurements of the CEP dependence of the HHG spectra.

Having succeeded in the generation of XUV pulses at 200 kHz, possible improvements in PEEM image quality were investigated. It was found that the spatial resolution indeed improved, partly due to the higher electron flux, enabling a narrower energy range of the electrons to be selected, thus reducing chromatic aberration. The exposure times were also considerably reduced which is important both for practical reasons and to ensure that the system is less sensitive to laser fluctuations and other instabilities. The imaging of only the primary electrons was demonstrated, which is of relevance for the originally proposed IR–XUV scheme [16].

Since work started on this thesis, two new time-resolved measurement techniques have been introduced by other groups: 1) near-field scanning optical microscopy combined with spectral interferometry [88] and 2) second-harmonic-generation microscopy [89]. The main advantage of PEEM compared to second-harmonic-generation microscopy is that its resolution is not limited by optical diffraction. Since PEEM is an imaging and not a scanning method as near-field scanning optical microscopy combined with spectral interferometry, it can probe several structures or several parts of one structure simultaneously, which can be advantageous if the response of different structures or different parts of the same structures are to be compared. (Studies employing PEEM and few-cycle (7 fs) laser pulses have also been presented by other groups since work started on this thesis. Sun *et al.* studied the dynamics of two gold squares of different sizes [82], while Jiang *et al.* [90] studied the dynamics at different locations within a *single* bowtie nanoantenna.)

Future work will involve the implementation of an interferometer in which the IR beam is sufficiently intense to be split into two arms, such that high-order harmonics can be generated in one of them. To realize this, the OPCPA laser system had to be improved even further. It currently provides pulses of 10μJ in energy, 7 fs in time duration at a repetition rate of 200 kHz. Two improvements were also made to the

HHG setup. The gas system in the vacuum chamber was improved to enable a higher pressure in the gas jet used for HHG. This is expected to increase the intensity of the XUV pulses generated. The vacuum chamber was also rebuilt to give space for the interferometer and to allow for the generated XUV to be directed into the PEEM chamber properly. The next step is to generate harmonics with this upgraded system.

Considering the ultra-short duration of the OPCPA laser pulses, the generation of only one isolated attosecond per IR pulse could be possible. This, together with the improved spatial resolution and reasonable exposure times found when combining PEEM with the attosecond pulses generated at high repetition rate, could open up for experiments probing the full plasmonic field in nanoparticles. These nanostructures could be of random nature, or designed, for example, using FIB. Hopefully, we could thereby gain more knowledge about plasmons. It is also possible that, somewhere along the way, we will gain new perspectives on the fundamental building blocks of our world, namely atoms.

Comments on the papers

I **Secondary electron imaging of nanostructures using extreme ultraviolet attosecond pulse trains and infrared femtosecond pulses**
In this paper some important factors for a successful IR–XUV experiment were investigated. Among other things it is reported that secondary electrons generated when light interacts with silver nanoparticles could potentially be used to reveal information on the attosecond timescale. Silver nanowires were also found to have a good contrast against the gold substrate when imaging with XUV light in PEEM experiments. I participated in the performance of the experiments and provided feedback on the manuscript.

II **High-order harmonic generation using a high-repetition-rate turnkey laser**
We demonstrated high-order harmonic generation using a high repetition rate turnkey laser. I planned, designed and acquired the high-order harmonic generation setup, with focus on vacuum parts, gauges, translation stages and ion pumps. I reviewed the used setup and planned for acquiring new parts. I participated in the experiments, made the data analysis and wrote the paper.

III **Imaging localized surface plasmons by femtosecond to attosecond time-resolved photoelectron emission microscopy- "ATTO-PEEM"**
Improvements in image quality and acquisition times were demonstrated, when combining XUV pulses at high repetition rate with PEEM. I participated in the experiment with PEEM combined with HHG at 200 kHz repetition rate and provided feedback on the manuscript.

IV **Carrier-envelope phase-dependent high-order harmonic generation with a high-repetition-rate OPCPA system**
The carrier-envelope phase dependence of HHG was studied. I planned, designed and acquired the experimental HHG setup. I participated in the experiment and contributed to the manuscript with figures and feedback.

V **Nanoscale imaging of local few-femtosecond near-field dynamics within a single plasmonic nanoantenna**
The few-cycle dynamics of a single nanoantennas was studied. I participated in discussions concerning the experiment and provided feedback on the manuscript.

VI **Size- and shape-dependent few-cycle near-field dynamics of bowtie nanoantennas**
The size and shape dependent few-cycle dynamics of bowtie nanoantennas was studied. I manufactured the nanoantennas, participated in the experiment, performed the data analysis and wrote the majority of the paper.

VII **Trajectory-resolved high-order harmonic generation in elliptically polarized fields in the presence of resonances**
The ellipticity dependence of the HHG process was studied. I planned, designed and acquired the high-order harmonic generation setup, with focus on vacuum parts, gauges, translation stages and ion pumps. I reviewed the used setup and planned for obtaining new parts. I participated in the experiments and contributed with feedback on the manuscript.

VIII **Spatially and spectrally resolved quantum path interference with chirped driving pulses**
By measuring the harmonic spectra as a function of chirp of the driving pulse and compare with mathematical modeling, we were able to extract information useful for reconstruction of the harmonic emission. I planned, designed and acquired the high-order harmonic generation setup, with focus on vacuum parts, gauges, translation stages and ion pumps. I reviewed the used setup and planned for obtaining new parts. I participated in the experiments.

Acknowledgements

In many ways, these years have been a very special and distinct part of my life: not least regarding everything I have learned, and all the people I have met and worked with.

I would like to thank my supervisor, Johan Mauritsson for this great opportunity. I value the confidence you had in me and all the things you have done for me. From you I have learned about positive thinking, about what is important and less important, and about completing things. Thanks are also due to Anders Mikkelsen, my co-supervisor, for the guidance in nanostructure fabrication and for boosting my self-confidence. I am also grateful to Anne L'Huillier, my other co-supervisor, for her humility and professionalism. It is largely thanks to you that there is such a pleasant working atmosphere among the Attosecond Group.

It is difficult for me to express my gratitude to everyone in the Attosecond Group in words. I simply hope that I have shown you in daily life how important and wonderful you all are. It was a pleasure to work with you and be around you. With you I ate my first (and most likely last) surströmming and strapped on my first pair skis. We have shared Jacuzzis, Småland, hot springs, lunches and barbecues. In our Atto-family there is a sense of togetherness and a feeling that everyone belongs.

I would like to thank Anne Harth for joining the group. Thanks to Arthur Losquin for being the best mini-supervisor anyone could have, and for being so kind. Thanks to Bastian Manschwetus for representing something familiar and German, Byunghoon Kim for something Gangnam-style, Chen Guo for being so pleasant to work with, Cord Arnold for being himself, Christoph Heyl for that ever glint in his eyes, David Kroon for being so comfortable to be around, Diego Guénot for his lightheartedness and for loving dogs, Erik Mansten for his aura of security, Esben Witting-Larsen for always (almost!) making me laugh and for his kind heart, Fernando Brizuela for his relaxed attitude, Filippo Campi for being Filippo Campi, Hampus Nilsson for being so respectful, Hélène Coudert-Alteirac for being so strong, Jan Lahl for being so clear in his mind, Jana Preclíková for being so happy and friendly, Jörg Schwenke for gently introducing me to the world of research, Kathrin Klünder for being there, Linnea Rading for our shared understanding and nail polishing sessions, Marcus Isinger for being so reliable, Mathieu Gisselbrecht for our rewarding teaching collaboration and all the human connections, Maïté Louisy for being in contact with something true, Marija Kotur for being so easy-going, Marko Swoboda for his wide perspectives, Marcus Dahlström for his jokes, which seem to be connected to some Atto-heart, Miguel Miranda for his calmness, Neven Ibrakovič for offering me hot food, Per Johnsson for his jokes and many other things, Piotr Rudawski for being so warm, Rafal Rakowski for his friend-

liness, Stefanos Carlström for his helpfulness to others and his brilliance in imitating skånska, Samuel Bengtsson for the occasional pushing and punching, Sylvain Maclot for making me smile and his awesome parties, Thomas Fordell for being kind, and Yu-Chen Cheng for being as kind!

During this work, I had the chance to perform experiments together with Erik Mårsell – thank you for your expertise and for being so kind. I was fortunate to learn about FIB from Richard Sundberg, Filip Lenrick and Dmitry Suyatin. Mariusz Graczyk and Ivan Maximov provided additional support in the clean room. During our experiments at Kemicentrum in Lund we were given wonderful help by Donatas Zigmantas and David Paleček. Annika Olsson was a great mentor who helped me to focus on what was important to me.

I am very happy to have been a part of the Division of Atomic Physics. The friendliness combined with professionalism amazes me still today. Thank you Claes-Göran Wahlström for heading this workplace and for your care. I appreciate all the lunch discussions at the Division. I would also like to thank the Division for giving me the possibility to teach, which I believe was very beneficial in my scientific development. I want to express my gratitude for all the help I received during these years from Anne Petersson Jungbeck, Bertil Hermansson, Camilla Nilsson, Harriet Lindahl, Jakob Testad, Minna Ramkull and Åke Johansson. And Nina Reistad: thank you for your eyes.

I want to thank all my friends and relatives for being there for me. You know who you are. Mikaela Claesson and Linnéa Stolle: tack för att jag har er. On a daily basis during these five years, Matilda Lindberg brought joy and fun, tack, k. I also want to thank Christian Svensson for going to NanoLund retreats.

Jag vill också passa på att rikta de djupaste tacken till min familj.

References

1. G. Galilei. *The Assayer*. Rome: Giacomo Mascardi (1623).

2. I. Newton. *Optics, 3:rd edition*. Addison-Wesley (1721).

3. S.E. Palmer. *Vision science: Photons to phenomenology*. MIT press (1999).

4. J.W. Kalat. *Biological Psychology*. Wadsworth Thomson Learning (2004).

5. D.D. Hoffman. *Conscious Realism and the Mind-Body Problem*. Mind & Matter **6**, 87–121 (2008).

6. J.A. McGilvray. *Constant colors in the head*. Synthese **100**, 197–239 (1994).

7. E. Hecht and A. Zajac. *Optics*. Addison-Wesley (1974).

8. M.A. Garcia. *Surface plasmons in metallic nanoparticles: fundamentals and applications*. J. Phys. D: Appl. Phys. **44**, 283001 (2011).

9. D.J. Griffiths. *Introduction to Electrodynamics*. Pearson (2008).

10. S.A. Maier. *Plasmonics: Fundamentals and Applications*. Springer (2007).

11. A.V. Durrant. *Some basic properties of stimulated and spontaneous emission: A semiclassical approach*. American Journal of Physics **44**, 630–635 (1976).

12. P. Bharadwaj, B. Deutsch and L. Novotny. *Optical Antennas*. Adv. Opt. Photon. **1**, 438–483 (2009).

13. M. Ferray, A. L'Huillier, X.F. Li, L.A. Lompre, G. Mainfray and C. Manus. *Multiple-harmonic conversion of 1064 nm radiation in rare gases*. J. Phys. B **21**, L31 (1988).

14. P.M. Paul, E.S. Toma, P. Breger, G. Mullot, F. Augé, Ph. Balcou, H.G. Muller and P. Agostini. *Observation of a train of attosecond pulses from high harmonic generation*. Science **292**, 1689 (2001).

15. A. Einstein. *Über einen die Erzeugung und Verwandlung des Lichtes betreffenden heuristischen Gesichtspunkt*. Ann. Physik **322**, 132 (1905).

16. M. I. Stockman, M. F. Kling, U. Kleineberg and F. Krausz. *Attosecond nanoplasmonic-field microscope*. Nat. Photon. **1**, 539–544 (2007).

17. A. Mikkelsen, J. Schwenke, T. Fordell, G. Luo, K. Klünder, E. Hilner, N. Anttu, A.A. Zakharov, E. Lundgren, J. Mauritsson, J.N. Andersen, H.Q. Xu and A. L'Huillier. *Photoemission electron microscopy using extreme ultraviolet attosecond pulse trains.* Review Of Scientific Instruments **80**, 123703 (2009).

18. P. Drude. *Zur Elektronentheorie der Metalle.* Ann. Phys. page 566613 (1900).

19. C. Kittel. *Introduction to solid state physics.* John Wiley and Sons, New York, NY (1996). Seventh edition.

20. J.M. Pitarke, V.M. Silkin, E.V. Chulkov and P.M. Echenique. *Theory of surface plasmons and surface-plasmon polaritons.* Reports on Progress in Physics **70**, 1 (2007).

21. L. Novotny and N. van Hulst. *Antennas for light.* Nat. Photon. **5**, 83–90 (2011).

22. G. Mie. *Beiträge zur Optik trüber Medien, speaiell kolloidaler Metallösungen.* Ann. Phys. page 25:377 (1908).

23. J. Aizpurua, G.W. Bryant, L.J. Richter, F.J. García de Abajo, B.K. Kelley and T. Mallouk. *Optical properties of coupled metallic nanorods for field-enhanced spectroscopy.* Phys. Rev. B **71**, 235420 (2005).

24. A. Kubo, K. Onda, H. Petek, Z. Sun, Y.S. Jung and H. K. Kim. *Femtosecond Imaging of Surface Plasmon Dynamics in a Nanostructured Silver Film.* Nano Letters **5**, 1123–1127 (2005).

25. H. Fischer and O.J.F. Martin. *Engineering the optical response of plasmonic nanoantennas.* Opt. Express **16**, 9144–9154 (2008).

26. J. Gersten and A. Nitzan. *Electromagnetic theory of enhanced Raman scattering by molecules adsorbed on rough surfaces.* J. Chem. Phys. **73**, 3023–3037 (1980).

27. J.I. Gersten. *The effect of surface roughness on surface enhanced Raman scattering.* J. Chem. Phys. **72**, 5779–5780 (1980).

28. P.F. Liao and A. Wokaun. *Lightning rod effect in surface enhanced Raman scattering.* J. Chem. Phys. **76**, 751–752 (1982).

29. E. Hao and G.C. Schatz. *Electromagnetic fields around silver nanoparticles and dimers.* J. Chem. Phys. **120**, 357–366 (2004).

30. P.J. Schuck, D.P. Fromm, A. Sundaramurthy, G. S. Kino and W.E. Moerner. *Improving the Mismatch between Light and Nanoscale Objects with Gold Bowtie Nanoantennas.* Phys. Rev. Lett. **94**, 017402 (2005).

31. S. A. Maier, M. L. Brongersma, P. G. Kik and H. A. Atwater. *Observation of near-field coupling in metal nanoparticle chains using far-field polarization spectroscopy.* Phys. Rev. B **65**, 193408 (2002).

32. A. Sundaramurthy, K.B. Crozier, G.S. Kino, D. P. Fromm, P.J. Schuck and W.E. Moerner. *Field enhancement and gap-dependent resonance in a system of two opposing tip-to-tip Au nanotriangles.* Phys. Rev. B **72**, 165409 (2005).

33. A. Merlen and F. Lagugné-Labarthet. *Imaging the Optical Near Field in Plasmonic Nanostructures*. Appl. Spectrosc. **68**, 1307–1326 (2014).

34. M. Aeschlimann, M. Bauer, D. Bayer, T. Brixner, S. Cunovic, F. Dimler, A. Fischer, W. Pfeiffer, M. Rohmer, C. Schneider, F. Steeb, C. Strüber and D.V. Voronine. *Spatiotemporal control of nanooptical excitations*. PNAS **107**, 5329–5333 (2010).

35. S. Kim, J. Jin, Y.-J. Kim, I.-Y. Park, Y. Kim and S.-W. Kim. *High-harmonic generation by resonant plasmon field enhancement*. Nature **453**, 757–760 (2008).

36. P. Dombi, A. Hörl, P. Rácz, I. Márton, A. Trügler, J.R. Krenn and U. Hohenester. *Ultrafast Strong-Field Photoemission from Plasmonic Nanoparticles*. Nano Letters **13**, 674–678 (2013).

37. B. Piglosiewicz, S. Schmidt, D.J. Park, J. Vogelsang, P. Grosz, C. Manzoni, P. Farinello, G. Cerullo and C. Lienau. *Carrier-envelope phase effects on the strong-field photoemission of electrons from metallic nanostructures*. Nat. Photon. **8**, 37–42 (2014).

38. A. Anderson, K.S. Deryckx, X.G. Xu, G. Steinmeyer and M.B. Raschke. *Few-Femtosecond Plasmon Dephasing of a Single Metallic Nanostructure from Optical Response Function Reconstruction by Interferometric Frequency Resolved Optical Gating*. Nano Letters **10**, 2519–2524 (2010).

39. J. Matyschok, T. Lang, T. Binhammer, O. Prochnow, S. Rausch, M. Schultze, A. Harth, P. Rudawski, C.L. Arnold, A. L'Huillier and U. Morgner. *Temporal and spatial effects inside a compact and CEP stabilized, few-cycle OPCPA system at high repetition rates*. Opt. Express **21**, 29656–29665 (2013).

40. M. Cinchetti, A. Gloskovskii, S.A. Nepjiko, G. Schönhense, H. Rochholz and M. Kreiter. *Photoemission Electron Microscopy as a Tool for the Investigation of Optical Near Fields*. Phys. Rev. Lett. **95**, 047601 (2005).

41. A. Grubisic, V. Schweikhard, T.A. Baker and D. J. Nesbitt. *Coherent Multiphoton Photoelectron Emission from Single Au Nanorods: The Critical Role of Plasmonic Electric Near-Field Enhancement*. ACS Nano **7**, 87–99 (2013).

42. G. Farkas. *Multiphoton Processes*. Wiley, New York (1978).

43. G. Farkas, Z.G. Horváth, C. Tóth, C. Fotakis and E. Hontzopoulos. *Linear surface photoelectric effect of gold in intense laser field as a possible high-current electron source*. Journal of Applied Physics **62**, 4545–4547 (1987).

44. O. Schmidt, G.H. Fecher, Y. Hwu and G. Schönhense. *The spatial distribution of non-linear effects in multi-photon photoemission from metallic adsorbates on Si(1 1 1)*. Surface Science **482485, Part 1**, 687–692 (2001).

45. W.M.H. Sachtler, G.J.H. Dorgelo and A.A. Holscher. *The work function of gold*. Surf. Sci. **5**, 221–229 (1966).

46. E. Mårsell. *Photoemission Electron Microscopy with an Attosecond Light Source* (2014). Licentiate thesis, Lund University.

47. M. Lewenstein, Ph. Balcou, M.Yu. Ivanov, A. L'Huillier and P.B. Corkum. *Theory of high-order harmonic generation by low-frequency laser fields.* Phys. Rev. A **49**, 2117 (1994).

48. P.B. Corkum. *Plasma perspective on strong-field multiphoton ionization.* Phys. Rev. Lett. **71**, 1994 (1993).

49. T. Popmintchev, M.-C. Chen, D. Popmintchev, P. Arpin, S. Brown, S. Alisauskas, G. Andriukaitis, T. Balciunas, O.D. Mücke, A. Pugzlys, A. Baltuska, B. Shim, S.E. Schrauth, A. Gaeta, C. Hernández-Garcia, L. Plaja, A. Becker, Agnieszka J.-B., M.M. Murnane and H.C. Kapteyn. *Bright Coherent Ultrahigh Harmonics in the keV X-ray Regime from Mid-Infrared Femtosecond Lasers.* Science **336**, 1287–1291 (2012).

50. G. Sansone, L. Poletto and M. Nisoli. *High-energy attosecond light sources.* Nat Photon **5**, 655–663 (2011).

51. J. Mauritsson, P. Johnsson, E. Gustafsson, A. L'Huillier, K.J. Schafer and M.B. Gaarde. *Attosecond Pulse Trains Generated Using Two Color Laser Fields.* Phys. Rev. Lett. **97**, 013001 (2006).

52. E. Mansten J. Mauritsson, M. Dahlström and T. Fordell. *Sub-cycle control of strong field processes using two color laser fields.* J. Phys. B (2009).

53. H.G. Muller. *Reconstruction of attosecond harmonic beating by interference of two-photon transitions.* Appl. Phys. B **74**, 17 (2002).

54. A. Zaïr, M. Holler, F. Schapper, J. Biegert, L. Gallmann, U. Keller, A.S. Wyatt, A. Monmayrant, I.A. Walmsley, E. Cormier, T. Auguste, J.P. Caumes and P. Salières. *Quantum Path Interferences in High-Order Harmonic Generation.* Physical Review Letters **100**, 143902–1–4 (2008).

55. K.S. Budil, P. Salières, A. L'Huillier, T. Ditmire and M.D. Perry. *Influence of ellipticity on harmonic generation.* Phys. Rev. A **48**, R3437 (1993).

56. I.J. Sola, E. Mével, L. Elouga, E. Constant, V. Strelkov, L. Poletto, P. Villoresi, E. Benedetti, J.-P. Caumes, S. Stagira, C. Vozzi, G. Sansone and M. Nisoli. *Controlling attosecond electron dynamics by phase-stabilized polarization gating.* Nature Phys. **2**, 319 (2006).

57. M. Möller, Y. Cheng, S.D. Khan, B. Zhao, K. Zhao, M. Chini, G.G. Paulus and Z. Chang. *Dependence of high-order-harmonic-generation yield on driving-laser ellipticity.* Phys. Rev. A **86**, 011401 (2012).

58. F. Lindner, W. Stremme, M.G. Schätzel, F. Grasbon, G.G. Paulus, H. Walther, R. Hartmann and L. Strüder. *High-order harmonic generation at a repetition rate of 100 kHz.* Phys. Rev. A **68**, 013814 (2003).

59. C. Gohle, T. Udem, M. Herrmann, J. Rauschenberger, R. Holzwarth, H. A. Schuessler, F. Krausz and T. W. Hansch. *A frequency comb in the extreme ultraviolet.* Nature **436**, 234–237 (2005).

60. R.J. Jones, K.D. Moll, M.J. Thorpe and J. Ye. *Phase-Coherent Frequency Combs in the Vacuum Ultraviolet via High-Harmonic Generation inside a Femtosecond Enhancement Cavity.* Phys. Rev. Lett. **94**, 193201 (2005).

61. M.C. Chen, M.R. Gerrity, S. Backus, T. Popmintchev, X. Zhou, P. Arpin, X. Zhang, H.C. Kapteyn and M.M. Murnane. *Spatially coherent, phase matched, high-order harmonic EUV beams at 50 kHz.* Opt. Exp. **17**, 17376–17383 (2009).

62. D.C. Yost, T.R. Schibli and J. Ye. *Efficient output coupling of intracavity high-harmonic generation.* Optics Letters **33**, 1099–1101 (2008).

63. J. Boullet, Y. Zaouter, J. Limpert, S. Petit, Y. Mairesse, B. Fabre, J. Higuet, E. Mevel, E. Constant and E. Cormier. *High-order harmonic generation at a megahertz-level repetition rate directly driven by an ytterbium-doped-fiber chirped-pulse amplification system.* Opt. Lett. **34**, 1489–1491 (2009).

64. S. Hädrich, M. Krebs, J. Rothhardt, H. Carstens, S. Demmler, J. Limpert and A. Tünnermann. *Generation of μW level plateau harmonics at high repetition rate.* Opt. Express **19**, 19374–19383 (2011).

65. A. Vernaleken, J. Weitenberg, T. Sartorius, P. Russbueldt, W. Schneider, S.L. Stebbings, M.F. Kling, P. Hommelhoff, H.-D. Hoffmann, R. Poprawe, F. Krausz, T.W. Hänsch and T. Udem. *Single-pass high-harmonic generation at 20.8 MHz repetition rate.* Opt. Lett. **36**, 3428–3430 (2011).

66. C.-T. Chiang, A. Blättermann, M. Huth, J. Kirschner and W. Widdra. *High-order harmonic generation at 4 MHz as a light source for time-of-flight photoemission spectroscopy.* Appl. Phys. Lett. **101**, 071116–071116–4 (2012).

67. C.M. Heyl, J. Güdde, A. L'Huillier and U. Höfer. *High-order harmonic generation with μJ laser pulses at high repetition rates.* Journal of Physics B: Atomic, Molecular and Optical Physics **45**, 074020 (2012).

68. J. Rothhardt, S. Demmler, S. Hädrich, J. Limpert and A. Tünnermann. *Octave-spanning OPCPA system delivering CEP-stable few-cycle pulses and 22 W of average power at 1 MHz repetition rate.* Opt. Express **20**, 10870–10878 (2012).

69. M. Krebs, S. Hädrich, S. Demmler, J. Rothhardt, A. Zaïr, L. Chipperfield, J. Limpert and A. Tünnermann. *Towards isolated attosecond pulses at megahertz repetition rates.* Nature Photonics **7**, 555–559 (2013).

70. S. Fuchs, C. Rödel, M. Krebs, S. Hädrich, J. Bierbach, A.E. Paz, S. Kuschel, M. Wünsche, V. Hilbert, U. Zastrau, E. Förster, J. Limpert and G.G. Paulus. *Sensitivity calibration of an imaging extreme ultraviolet spectrometer-detector system for determining the efficiency of broadband extreme ultraviolet sources.* Review of Scientific Instruments **84**, 023101 (2013).

71. M. Huth, C.-T. Chiang, A. Trützschler, F.O. Schumann, J. Kirschner and W. Widdra. *Electron pair emission detected by time-of-flight spectrometers: Recent progress.* Appl. Phys. Lett. **104**, 061602 (2014).

72. C.A. Volkert and A.M. Minor. *Focused Ion Beam Microscopy and Micromachining.* MRS Bulletin **32**, 389–399 (2007).

73. L.A. Giannuzzi and F.A. Stevie, editors. *Introduction to Focused Ion Beams: Instrumentation, Theory, Techniques and Practice.* Springer, New York (2005).

74. S. Reyntjens and R. Puers. *A review of focused ion beam applications in microsystem technology.* Journal of Micromechanics and Microengineering **11**, 287 (2001).

75. J. Karlsson, L. Rippe and S. Kröll. *A confocal optical microscope for detection of single impurities in a bulk crystal at cryogenic temperatures* (). Manuscript in preparation.

76. H. Kollmann, X. Piao, M. Esmann, S.F. Becker, D. Hou, C. Huynh, L.-O. Kautschor, G. Bösker, H. Vieker, A. Beyer, A. Gölzhäuser, N. Park, R. Vogelgesang, M. Silies and C. Lienau. *Toward Plasmonics with Nanometer Precision: Nonlinear Optics of Helium-Ion Milled Gold Nanoantennas.* Nano Letters **14**, 4778–4784 (2014).

77. V. Callegari. *Fabrication of photonic elements by focused ion beam (FIB).* PhD thesis ETH (2009).

78. H. Wei, A. Reyes-Coronado, P. Nordlander, J. Aizpurua and H. Xu. *Multipolar Plasmon Resonances in Individual Ag Nanorice.* ACS Nano **4**, 2649–2654 (2010).

79. H. Liang, H. Yang, W. Wang, J. Li and H. Xu. *High-Yield Uniform Synthesis and Microstructure-Determination of Rice-Shaped Silver Nanocrystals.* Journal of the American Chemical Society **131**, 6068–6069 (2009).

80. H. Liang, H. Zhao, D. Rossouw, W. Wang, H. Xu, G. A. Botton and D. Ma. *Silver Nanorice Structures: Oriented Attachment-Dominated Growth, High Environmental Sensitivity, and Real-Space Visualization of Multipolar Resonances.* Chemistry of Materials **24**, 2339–2346 (2012).

81. M. Miranda, T. Fordell, C. Arnold, A. L'Huillier and H. Crespo. *Simultaneous compression and characterization of ultrashort laser pulses using chirped mirrors and glass wedges.* Opt. Express **20**, 688–697 (2012).

82. Q. Sun, K. Ueno, H. Yu, A. Kubo, Y. Matsuo and H. Misawa. *Direct imaging of the near field and dynamics of surface plasmon resonance on gold nanostructures using photoemission electron microscopy.* Light: Sci. Appl. **2**, e118 (2013).

83. D. Bauer. *Emergence of Classical Orbits in Few-Cycle Above-Threshold Ionization of Atomic Hydrogen.* Phys. Rev. Lett. **94**, 113001 (2005).

84. C. Wiemann, D. Bayer, M. Rohmer, M. Aeschlimann and M. Bauer. *Local 2PPE-yield enhancement in a defined periodic silver nanodisk array.* Surf. Sci. **601**, 4714–4721 (2007). Proceedings of the Fifth International Conference on LEEM/PEEM.

85. M. Bauer, C. Wiemann, J. Lange, D. Bayer, M. Rohmer and M. Aeschlimann. *Phase propagation of localized surface plasmons probed by time-resolved photoemission electron microscopy.* Appl. Phys. A **88**, 473–480 (2007).

86. M. Chelvayohan and C.H.B. Mee. *Work function measurements on (110), (100) and (111) surfaces of silver.* Journal of Physics C: Solid State Physics **15**, 2305 (1982).

87. A.W. Dweydari and C.H.B. Mee. *Work function measurements on (100) and (110) surfaces of silver.* physica status solidi (a) **27**, 223–230 (1975).

88. S. Onishi, K. Matsuishi, J. Oi, T. Harada, M. Kusaba, K. Hirosawa and F. Kannari. *Spatiotemporal control of femtosecond plasmon using plasmon response functions measured by near-field scanning optical microscopy (NSOM).* Opt. Express **21**, 26631–26641 (2013).

89. N. Accanto, L. Piatkowski, J. Renger and N.F. van Hulst. *Capturing the Optical Phase Response of Nanoantennas by Coherent Second-Harmonic Microscopy.* Nano Letters **14**, 4078–4082 (2014).

90. Q. Jiang, J. Bo-Yu, H. Zuo-Qiang and L. Jing-Quan. *Probing of Ultrafast Plasmon Dynamics on Gold Bowtie Nanostructure Using Photoemission Electron Microscopy.* Chin. Phys. Lett. **32**, 064202 (2015).